

UNIVERSITÄT LEIPZIG

Faculty of Physics and Earth Sciences
Institute of Experimental Physics II
Semiconductor Physics Group

Master Thesis

**Growth and Properties of Na_2IrO_3
Thin Films**

submitted by

Marcus Jenderka

in partial fulfillment of the requirements for the degree of
Master of Science (M. Sc.)
in Physics (IPSP)

Supervisors:

Prof. Dr. Michael Lorenz
Prof. Dr. Marius Grundmann

Referees:

Prof. Dr. Marius Grundmann
Prof. Dr. Michael Lorenz

Leipzig, November 19, 2012

Contents

1	Introduction and Motivation	5
2	Theory	7
2.1	Introduction to Topological Insulators	7
2.2	Spin Liquids and the Kitaev Model for Hexagonal Honeycomb Lattices	10
2.3	Na ₂ IrO ₃ as a Mott Insulator	11
2.3.1	Level Schemes	11
2.3.2	The Hubbard Model	15
2.4	Intrinsic Conductivity in Ideal Semiconductors	18
2.5	Conductivity in Disordered Solids	21
2.6	Variable Range Hopping	24
3	Review and Properties of Single and Polycrystalline Na₂IrO₃	31
4	Experimental Methods	35
4.1	X-ray Diffraction	35
4.2	Atomic Force Microscopy (AFM)	37
4.3	SEM and EDX	38
4.4	Optical Transmission	39
4.5	Hall Effect and Resistivity Measurements	40
5	Thin Film Deposition	43
5.1	Pulsed Laser Deposition (PLD)	43
5.2	Sputter Deposition of Gold Contacts	45
5.3	PECVD of SiN _x as Passivation and Protective Layer	47
6	Results and Discussion	49
6.1	Growth of Na ₂ IrO ₃	49
6.1.1	Structural Analysis - XRD	49
6.1.2	Surface Morphology - AFM	58
6.1.3	Chemical Film Composition and Surface Corrosion	61
6.2	Temperature Dependent Electrical Resistivity	64
6.3	Magnetic Properties	71
6.4	Optical Properties	76
7	Summary and Outlook	79

Bibliography	83
A Appendix	95
A.1 AFM Images	95
A.2 JCPDS Diffraction Database Patterns	100
Acknowledgments	103
Statement of Authorship (Selbständigkeitserklärung)	105
Permission for Thesis Deposit (Erklärung für die Bibliothek)	107

1 Introduction and Motivation

Electronic correlations in layered transition metal oxides (TMOs) provide for interesting new physics. In recent years, many TMOs have been discovered to show correlated behaviour such as odd-parity superconductivity in Sr_2RuO_4 [1], the metal-insulator transition in $\text{Cd}_2\text{Os}_2\text{O}_7$ [2] or superconductivity in water intercalated Na_xCoO_2 [3].

In the transition metal series, electron correlations are expected to be strongest for 3d transition metals and decrease for 4d and 5d metals due to the increasing spatial extent of the d orbital. It is expected [4], that the larger spatial extent alone causes the more weakly correlated 5d TMOs to be metallic, since in this case Coulomb interactions are reduced which is beneficial for electrical conduction. However, recent experiments have shown that some 5d TMOs are actually insulators [5–7]. The insulating properties were in parts related to an interplay between electron correlations and strong spin orbit coupling [8] that in turn increases with atomic number from 3d to 5d. Also, due to the increased spatial extent of the d orbitals, crystal field splittings and 2p hybridization between transition metal and oxygen octahedron are enhanced. This in turn leads to strong electron-lattice couplings that can alter and distort metal-oxygen bond lengths and angles lifting degeneracies of bands and gaps. Thus in 5d systems spin orbit coupling (SOC) and electron correlations are of comparable size and act cooperatively, which can lead to intriguing new physics.

There are several proposals for intriguing emerging quantum phases in these materials like spin liquid behaviour, topological insulators and related phases [9–13]. Some recent experimental findings like a spin liquid state in the $S=1/2$ hyperkagome antiferromagnet $\text{Na}_4\text{Ir}_3\text{O}_8$ [10, 14] and metallic spin liquid behavior in $\text{Pr}_2\text{Ir}_2\text{O}_7$ [15] prove these predictions right. Furthermore, the novel $J_{\text{eff}}=1/2$ Mott insulating ground state in Sr_2IrO_4 can be ascribed to strong SOC in the presence of electron correlations leading to J_{eff} being a good quantum number instead of only the spin S [8].

Another example of above 5d transition metal oxides is the Mott insulating [16] layered iridate Na_2IrO_3 . In Na_2IrO_3 , Ir^{4+} ions form a honeycomb lattice and both strong SOC and electron correlations are present. Based on tight binding calculations, Na_2IrO_3 among other TMOs was recently proposed as a topological insulator at room temperature with antiferromagnetic ordering [12, 17]. Several further theoretical studies using a Heisenberg-Kitaev model suggest a rich phase diagram with emergent magnetically ordered, spin liquid and topological phases [13, 18, 19]. Especially the topological

and spin liquid phases promise a potential for application of Na_2IrO_3 in fault tolerant quantum computation.

To the best of the author's knowledge, experimental effort on Na_2IrO_3 was so far limited to powder and single-crystalline samples. Partly for this reason, this thesis is concerned with the deposition of Na_2IrO_3 thin films. Studying the feasibility of thin film deposition of Na_2IrO_3 is hence yet another step towards the future application of this novel material. Deposition is done by means of pulsed laser deposition (PLD). An array of experimental probes is employed to extensively study the structural, electrical, optical and magnetic properties of Na_2IrO_3 thin films. The purpose of this thesis is furthermore to experimentally verify proposals of the quantum phases mentioned above, for instance to find signatures of a topological phase in Na_2IrO_3 thin films.

2 Theory

On account of theoretical proposals for Na_2IrO_3 , this chapter begins with a brief introduction to the concept of topological insulators followed by a short definition of spin liquids and the Kitaev model. Afterwards the origin of the experimentally found Mott insulating properties [4] together with the observed hopping conductivity will be discussed.

2.1 Introduction to Topological Insulators

Three-dimensional topological insulators (TIs) represent a new kind of quantum structure of matter that have been predicted theoretically in 2005 [20, 21] prior to their experimental discovery in zinc-blende based HgTe quantum wells in 2007 [22]. Among the first three-dimensional TIs investigated theoretically and experimentally are the binary tetradymite semiconductors Bi_2Se_3 (cf. Fig. 2.2), Bi_2Te_3 and the $\text{Bi}_{1-x}\text{Sb}_x$ alloy [23–26].

Topological insulators are usual band insulators where a bulk energy gap prevents electrical conduction. However, as opposed to a trivial band insulator, the material's band structure exhibits surface states (SSs) that allow electrons to conduct at the surface. Those surface states are gapless and spin-split, i.e. they cross the bulk band gap and individual branches can be assigned to one of two spin directions (Fig. 2.1a). The surface state structure is similar to the Dirac cone as known from graphene (Fig. 2.1b). Along

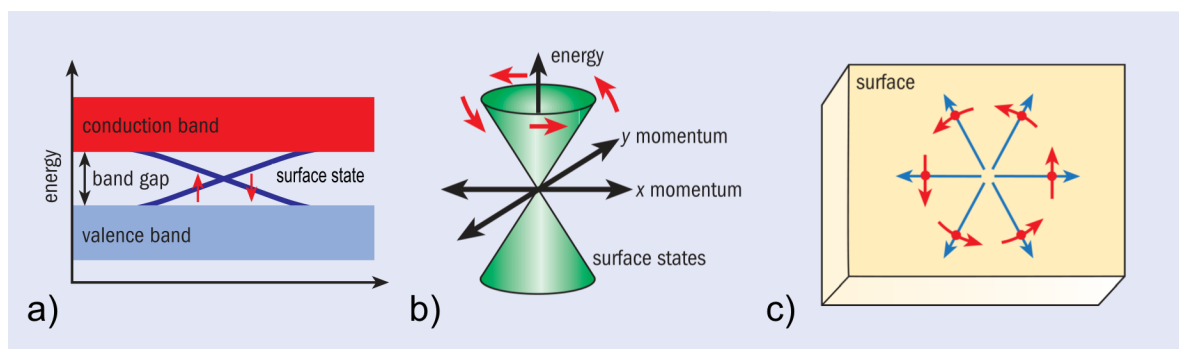


Figure 2.1 3D topological insulator. **a)** Schematic of a typical band structure. Gapless, spin-split surface states (SS) cross the bulk energy gap of an ordinary band insulator. **b)** In the k_x - k_y -momentum plane, the SSs have a Dirac cone structure similar to graphene. **c)** The surface is like a "planar metal", since electron motion in any direction is possible. The spins are locked perpendicularly to the direction of propagation. (from [27])

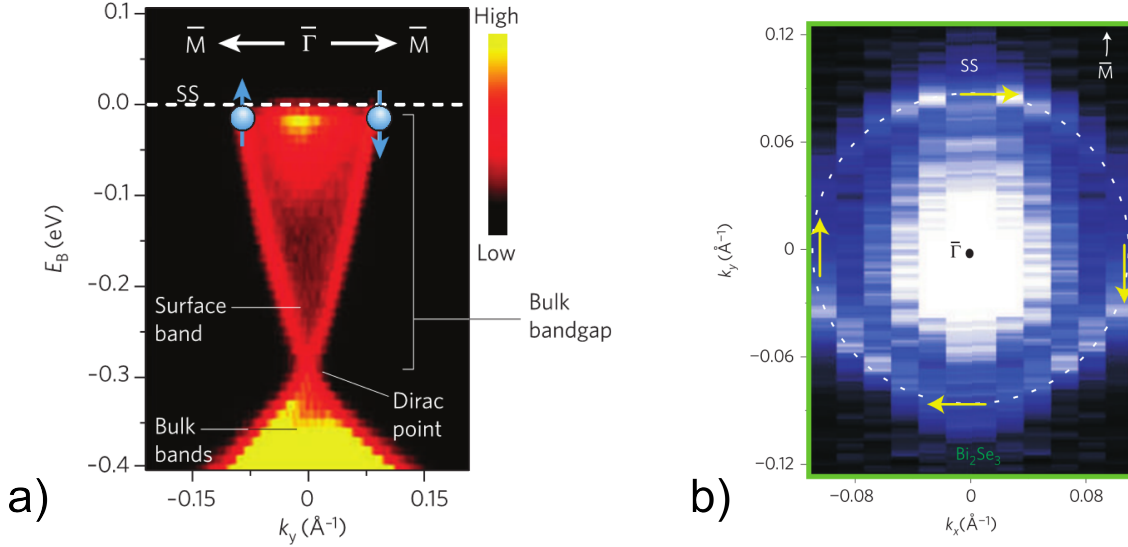


Figure 2.2 Bi_2Se_3 is a 3D topological insulator with Dirac cone structure. (a) Surface electronic band dispersion of $\text{Bi}_2\text{Se}_3(111)$ measured by angle-resolved photoemission spectroscopy (ARPES) with incident photon energy of 22 eV. The measurement was performed along the Γ - K direction. (b) High-momentum-resolution data around the Γ -point obtained by ARPES reveal a single ring formed by the surface state V-shaped Dirac band. The intensity in the middle of the ring is due to the presence of the bulk conduction band. (from [23])

the two-dimensional conducting surface of the topological insulator electron motion is possible in any direction. The surface can hence be considered a "planar metal". The electron spin is locked in-plane and perpendicular to the direction of propagation. It varies continuously with the direction of propagation along the surface (Fig. 2.1c). A differentiation can be made between a weak and a strong topological insulator in terms of the topological protection of their surface states. In the presence of disorder, the former becomes a trivial band insulator, while in the strong TI the topological surface states remain protected. The 3D quantum spin Hall state or the strong topological insulator considered here requires material with large spin orbit coupling (SOC) like mercury or bismuth. But also 5d transition metal ions like Ir^{4+} have significant SOC. Figure 2.2 shows experimental results on Bi_2Se_3 , one of the first 3D topological insulators discovered. In strong TIs, the beforementioned surface states are insensitive to impurities and imperfections of the crystal. Electron motion is thus not inhibited by backscattering and the transport is nearly dissipationless. Surface states are further protected by time-reversal invariant (TRI) perturbations. An example for a TRI perturbation is a photon ejecting a photoelectron by way of the photoelectric effect. On the other hand, introducing magnetic order into the crystal represents a perturbation that will destroy surface states, essentially creating gaps inside the surface states. The topological insulator then becomes insulating also on the surface [28].

The search for novel topological insulator materials to overcome the limitations of current materials continues and further proposals are constantly being made. Materials design flexibility is required to enhance topological properties and to allow for the observation of interesting topological phenomena such as the observation of Majorana fermions (see section below). Moreover, new materials would allow for the simultaneous tunability of electronic, magnetic and superconducting properties and thus opening up new vistas in the envisioned application in spintronics, magnetoelectric devices or quantum computation.

Among the continuously growing number of proposed materials are ternary tetradymite-like compounds (such as $\text{Bi}_2\text{Se}_2\text{S}$, $\text{Sb}_2\text{Te}_2\text{Se}$ and $\text{Sb}_2\text{Te}_2\text{S}$) [29] or ternary famatinitite and quaternary chalcogenides (such as Cu_3SbSe_4 and $\text{Cu}_2\text{CdSbSe}_4$, respectively) [30]. Furthermore there have been proposals [31, 32] and experimental proof [33, 34] for topological insulator phases in thallium-based ternary chalcogenides TlBiTe_2 and TlBiSe_2 . Also a wide range of ternary Heusler compounds (LnAuPb , LnPdBi , LnPtSb and LnPtBi) [35–37] are among the proposed new materials. Proposals among the oxide materials, and as such closer to the scope of this thesis, have been made for Os- and Ir-based pyrochlore oxides A_2IrO_7 and $\text{A}_2\text{Os}_2\text{O}_7$, respectively [38–40], in perovskite oxides [41] and on the kagome lattice [42]. It is hence obvious that Na_2IrO_3 is just one of many promising candidates for new topological insulator materials.

It was already mentioned that surface states allow nearly perfect transport, as the electron motion on the surface is protected from backscattering. Combining this feature with the possibility of creating Majorana particles could lead to a new architecture for quantum bits, which would be a step towards fault tolerant topological quantum computers [43]. Majorana fermions are fundamental particles that have been devised in particle and condensed matter physics. Their existence has yet to be proven. Majorana fermions have half-integer spin and quantum numbers that differ from those of the electron. They are electrically neutral and their own antiparticle.

In particle physics, neutrinos are a proposed candidate for elementary Majorana fermions, in which case the sought-after neutrinoless double-beta decay is possible [44]. However, in condensed matter physics, more promising proposals were made that Majorana fermions can appear in the form of quasiparticles at the interface between topological insulators and superconductors [45, 46]. For the creation of Majorana fermions via a superconductor, a topological superconductor is required. One way to realize such a superconductor is to place a topological insulator in contact with an ordinary

superconductor. By way of the proximity effect¹ the surface states will then become superconducting and a Majorana fermion is created [47]. Another way of achieving such a topological superconductor is to induce superconductivity of the system by applying isostatic pressure. The bulk of the sample becomes superconducting and on its part makes the surface state superconducting via the proximity effect [48]. Another proposal has been that of the solid state manifestation of Majorana fermions in semiconducting wires that are in contact with a superconductor at one end [49,50]. In 2012, an experiment from Delft marked a possible verification of the latter proposal [51].

2.2 Spin Liquids and the Kitaev Model for Hexagonal Honeycomb Lattices

A topologically insulating state has been just one of two proposals on Na_2IrO_3 . Another emergent quantum phase proposed for Na_2IrO_3 is spin liquid behaviour [13]. The proposal is a consequence of the hexagonal arrangement of Ir^{4+} ions forming a honeycomb lattice of effective spin 1/2 moments which in turn could be a realization of the Kitaev model [52]. In the Kitaev model spins $S = 1/2$ sit on the vertices of a honeycomb lattice. The lattice consist of two equivalent sublattices and the unit cell contains one vortex of each sublattice (see Fig. 2.3a). Depending on the direction, there are three bonds $\gamma = \{x, y, z\}$. The nearest-neighbour exchange interactions J_γ of spins one-half on these bonds are anisotropic, ferromagnetic and may differ in strength. The respective hamiltonian reads

$$H_{ij}^{(\gamma)} = -J_\gamma S_i^\gamma S_j^\gamma. \quad (2.1)$$

The model has an exact analytical solution. As a ground state we find among others a gapless spin liquid that has a potential use in quantum computation [53]. Spin liquids occur in frustrated magnets among other exotic quantum phases of Mott insulators. In a (quantum) spin liquid enhanced fluctuations of correlated spins prevent an ordering of magnetic moments even down to a temperature of 0 K (for a review on spin liquids see [54]).

In the hexagonal unit cell of a A_2BO_3 -type layered compound the magnetic ions, in our case spin one-half Ir^{4+} , form a honeycomb lattice. In this case, the edge-shared IrO_6 octahedra form 90° Ir-O-Ir bonds. Consequently, exchange interactions via these

¹also called Holm-Meissner effect

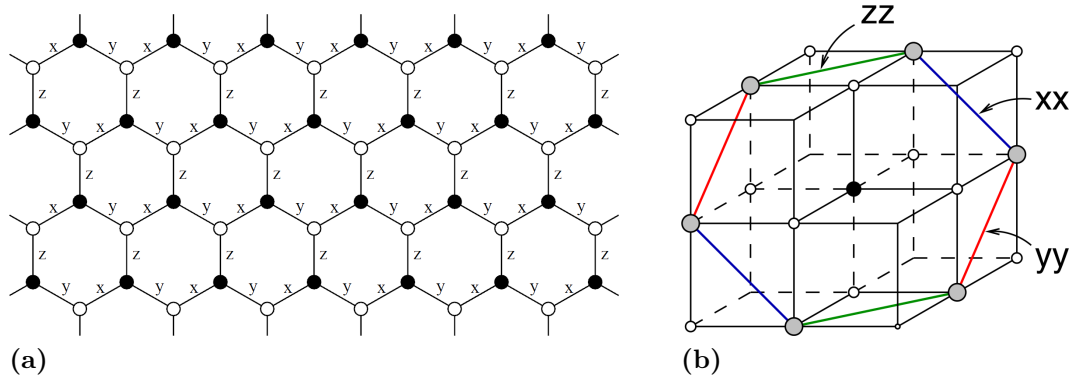


Figure 2.3 The Kitaev Model. **a)** Spin 1/2 moments on a honeycomb lattice with two equivalent sublattices (full and empty circles). **b)** Hexagonal of a A_2BO_3 -type layered compound forming a honeycomb lattice with three non-equivalent links XX, YY and ZZ. (from [52] and [13])

bonds are anisotropic and depend on the bond direction [13]. There are then three nonequivalent bonds XX, YY, ZZ each perpendicular to the cubic axes x , y , z (see Fig. 2.3b). On those three nonequivalent bonds only the corresponding components of spins are coupled, e.g., $S_i^x S_j^x$ on XX-links. Precisely for this reason the model is highly frustrated [18]. In fact, geometrical magnetic frustration has been found in experiments on Na_2IrO_3 [4]

2.3 Na_2IrO_3 as a Mott Insulator

In 2010, experiments [4] showed insulating behaviour in Na_2IrO_3 accompanied by anti-ferromagnetic long range order. With a half-filled t_{2g} band, Na_2IrO_3 should be metallic according to classic band theory. Strong Coulomb repulsions in this and other TMOs lead to the observed insulating behaviour of the so-called Mott insulator. In the following sections, the level scheme of 5d transition metal oxides in general and Na_2IrO_3 in particular will be discussed. It then follows an illustration of the formation of a Mott gap inside a half-filled d-band rendering the system insulating. A lot of the following information that is valid for transition metal oxides in general is taken from [55–57].

2.3.1 Level Schemes

In transition metal oxides with half-filled d orbitals and hence an odd number of electrons per unit cell, simple band theory would predict that the systems were metallic.

Instead, for some of those systems experiments show that they are so-called Mott insulators. The experimentally observed insulating behavior is attributed to electron correlations, specifically strong Coulomb repulsions U between the charge carriers, that are larger than the carrier's kinetic energy. While in a conventional band insulator conduction electrons occupy a completely filled band and a band gap prohibits conduction, in a Mott insulator electrons instead need to overcome a Mott gap U to create doubly occupied sites and to delocalize. Furthermore, a possible display of antiferromagnetic order below an ordering temperature T_N is a consequence of super-exchange interactions mediated by virtual tunneling.

In 5d transition metal oxides, transition metal ions are surrounded by six oxygen atoms. The six oxygen atoms form an octahedral crystal field with cubic symmetry or, if the octahedron is elongated along one direction, a field with tetragonal symmetry. In both cases, the five-fold degenerate 5d orbitals split into two highest orbitals $d(x^2-y^2)$ and $d(3z^2-r^2)$, referred to as e_g orbitals, and three low energy orbitals t_{2g} comprised of $d(xy)$, $d(yz)$ and $d(zx)$ (Fig. 2.4). In a cubic field e_g and t_{2g} are doubly and triply degenerate, respectively, and split by $10Dq \approx 3$ eV [58]. On the other hand, in a tetragonal field further degeneracies are lifted. A consequence of the crystal field is the quenching of angular momentum such that the magnetic moment of a transition metal compound is equal to the spin. This is usually the case for 3d transition metal ions. In 5d transition metal ions, spin orbit coupling is one order of magnitude larger and angular momentum is not as effectively quenched. There are other consequences of much stronger strong spin orbit interactions in 5d transition metal oxides as discussed below.

For the explanation of Mott insulating behaviour in Na_2IrO_3 two level schemes are currently considered in literature that consider the large spin orbit coupling in 5d transition metals. The first has been successfully applied to explain the novel $J_{eff} = 1/2$ Mott insulator in Sr_2IrO_4 [8, 59]. Another scheme includes trigonal distortions leading to a tetragonal crystal field [60, 61].

For 5d transition metal oxides the cubic crystal field splitting $10Dq$ is in general large enough to yield a t_{2g}^5 low spin state for the Ir^{4+} ions in Na_2IrO_3 with the highest t_{2g} orbital half filled (Fig. 2.5a); the system would now be metallic. For a typical Mott insulator an unrealistically high U is now required to open a Mott gap in the highest t_{2g} band (Fig. 2.5b). It must be noted here, that in 5d transition metals Coulomb repulsions are weaker than in 3d transition metals. Instead, high spin orbit coupling prevents the usual angular momentum quenching. As a consequence, the t_{2g} states

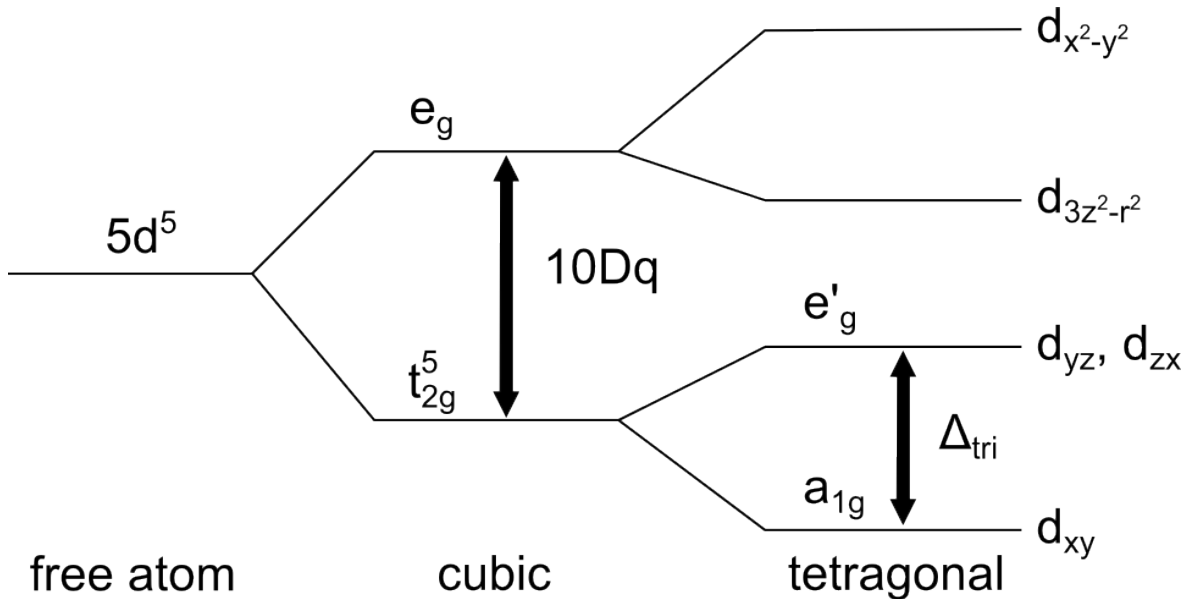


Figure 2.4 Crystal-field splittings of 5d orbitals under crystal fields with cubic and tetragonal symmetries.

effectively correspond to angular momentum $L = 1$. In the presence of strong spin orbit coupling the t_{2g} bands split into an effective $J_{eff} = 1/2$ doublet and a $J_{eff} = 3/2$ quartet band (Fig. 2.5c). The resultant narrow $J_{eff} = 1/2$ band is half-filled and now even a small U opens a Mott gap (Fig. 2.5d) splitting the narrow band into a so-called upper Hubbard band (UHB) and lower Hubbard band (LHB). The terminology of Hubbard bands will be explained in section 2.3.2.

Aforementioned level scheme did not include trigonal distortions of the crystal field due to compression or expansion along one of the four axes of IrO₆ octahedra. We discuss this level scheme according to local-density approximation (LDA) calculations by Jin [61] (see figure 2.6). A trigonal crystal field Δ_{tri} lifts the degeneracy of the t_{2g} splitting them into a e'_g quartet band and a a_{1g} doublet (Fig. 2.4). Strong hybridization between neighbouring Ir 5d orbitals gives rise to the bonding and anti-bonding of the e'_g states, that is a narrow e_{AB} at E_F and e_B below E_F , respectively (Fig. 2.6a). Indeed, spin orbit coupling already splits the half-filled e_{AB} doublet over the entire Brillouin zone (Fig. 2.6b). In spite of the splitting, a small electron pocket at the A point is still left rendering the system insulating. Only the combination with on-site Coulomb repulsion U results in the opening of a Mott gap in the spin orbit-split e_{AB} doublet (Fig. 2.6c). However, the LDA calculations show that even without U an increase in spin orbit interactions can open a sufficiently large gap. This is in contrast to Sr₂IrO₄ for instance where the Mott gap can be attained only when the on-site U is introduced.

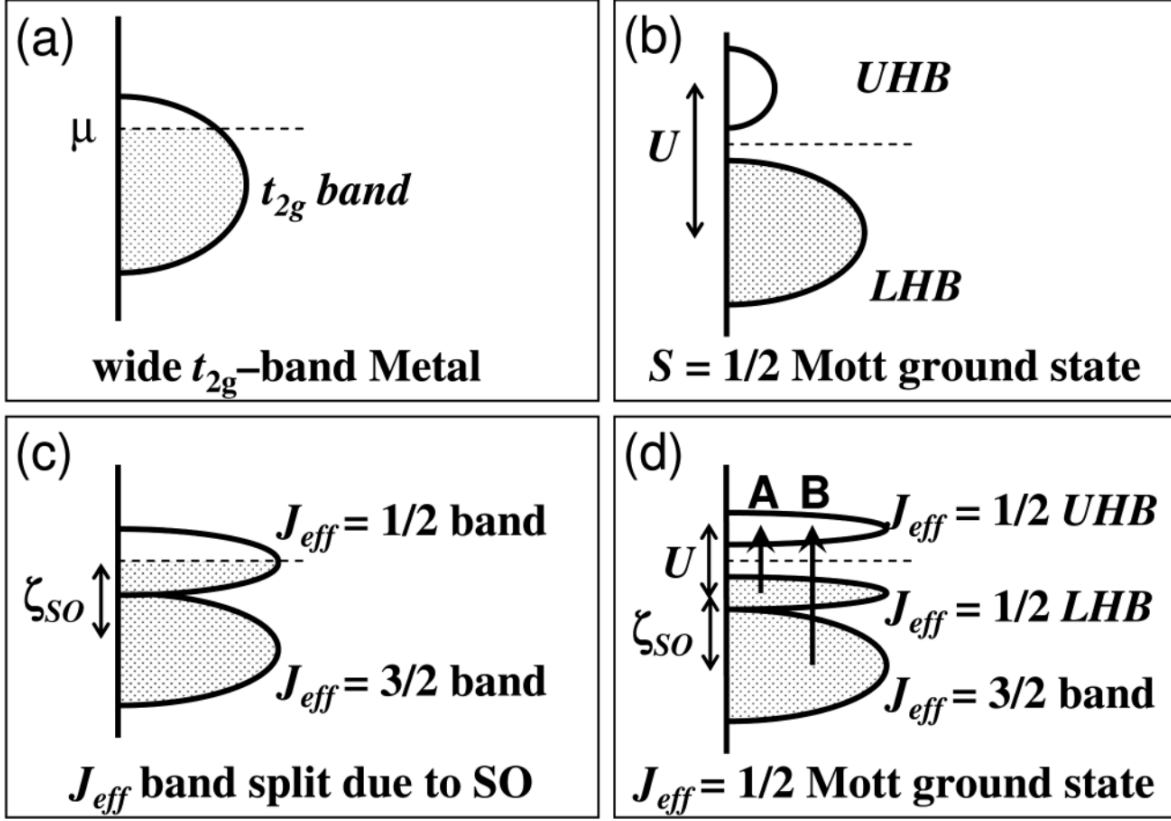


Figure 2.5 Schematic energy diagrams for the $5d^5$ (t_{2g}^5) low-spin configuration (a) without SOC and U , (b) with an unrealistically large U and no SOC, (c) with SOC (ζ_{SO}) but no U , and (d) with SOC and U . Possible optical transitions A and B are indicated by arrows. μ denotes the Fermi level; UHB and LHB denote the upper and lower Hubbard bands, see text. (from [59])

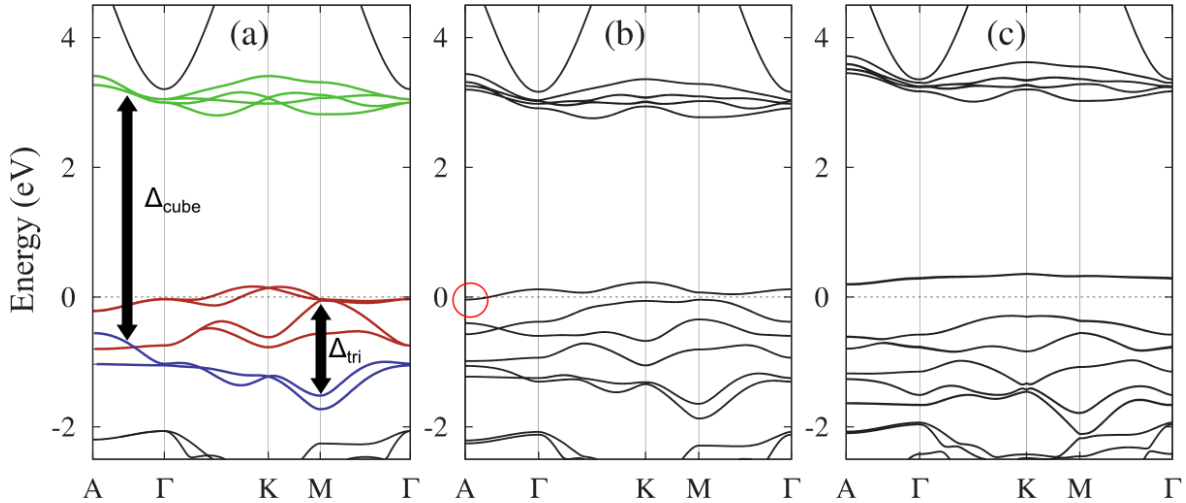


Figure 2.6 Electronic band structure calculations of Na_2IrO_3 within (a) LDA, (b) LDA+SO, and (c) LDA+ U +SO schemes. Green, red, and blue colored energy dispersions in (a) are indicating e_g , e'_g , and a_{1g} bands respectively, induced by cubic and trigonal crystal fields Δ_{cube} and Δ_{tri} , respectively. The red circle in (b) is a guide to the eye for the small electron pocket at the A point. (adapted from [61])

2.3.2 The Hubbard Model

It was found [4] that Na₂IrO₃ is an antiferromagnetic Mott insulator. A very simple model that in its parameter space contains an antiferromagnetic Mott insulating ground state is the Hubbard model [62,63]. The model combines both localization and delocalization of electrons via strong Coulomb repulsion and via a tight-binding Hamiltonian accounting for hopping processes, respectively. The following discussion about the model is mainly based on [56,57]. In the model, one considers a d -dimensional cubic lattice of hydrogen atoms. The protons provide L lattice sites for $N = L$ electrons - the system is at half filling. Furthermore, the electrons sit on the atoms with only local electron-electron interactions. The Hubbard U is then ionization energy minus electron affinity

$$U = E(H \rightarrow H^+) - |E(H \rightarrow H^-)| \quad (2.2)$$

It is further assumed that electrons hop only between neighbouring lattice sites. This tunneling is the tight-binding part of the model. The Hamiltonian in second quantization reads

$$H = -t \sum_{\langle ij \rangle} (c_{i\sigma}^\dagger c_{j\sigma} + H.c.) + U \sum_i n_{i\uparrow} n_{i\downarrow} \quad (2.3)$$

where $c_{i\sigma}^\dagger$ ($c_{i\sigma}$) is the creation (annihilation) operator with $n_{i\sigma} = c_{i\sigma}^\dagger c_{i\sigma}$. In this model t is the hopping integral between neighbouring sites $\langle ij \rangle$ and expresses the probability for this process to happen. It is this kinetic energy causing the tendency to delocalize. The Hubbard U describes the on-site repulsion of two electrons at the same site. For a Mott insulator U is much larger than t . If after a hopping process an electron has moved to a neighbouring site now doubly occupied the energy is increased by U . Due to this large energy cost the electrons are instead localized on their ion and cannot move and the system is insulating.

The creation of a Mott gap can be illustrated as follows. Nearest neighbour hopping t with resultant bands of small bandwidth $W = 2Zt$ and Z number of nearest neighbours is strongly repressed by the Coulomb repulsion. Adding another electron to the ground state $E_0(N)$ of the half-filled electron system (Fig. 2.7), where N is equal to the number of electrons, requires an energy $\mu^+(N) = E_0(N+1) - E_0(N)$ with $\mu^+(N) = U - W_1/2$. The spectrum of these charge excitation form the upper Hubbard band (UHB) of width W_1 . Similarly for the removal of an electron an energy $\mu^-(N) = E_0(N) - E_0(N-1) = W_2/2$ is needed where the excitation spectrum makes up the lower Hubbard band (LHB) of width W_2 . As a consequence, a gap for charge excitations $\Delta\mu = U - (W_1 - W_2)/2$

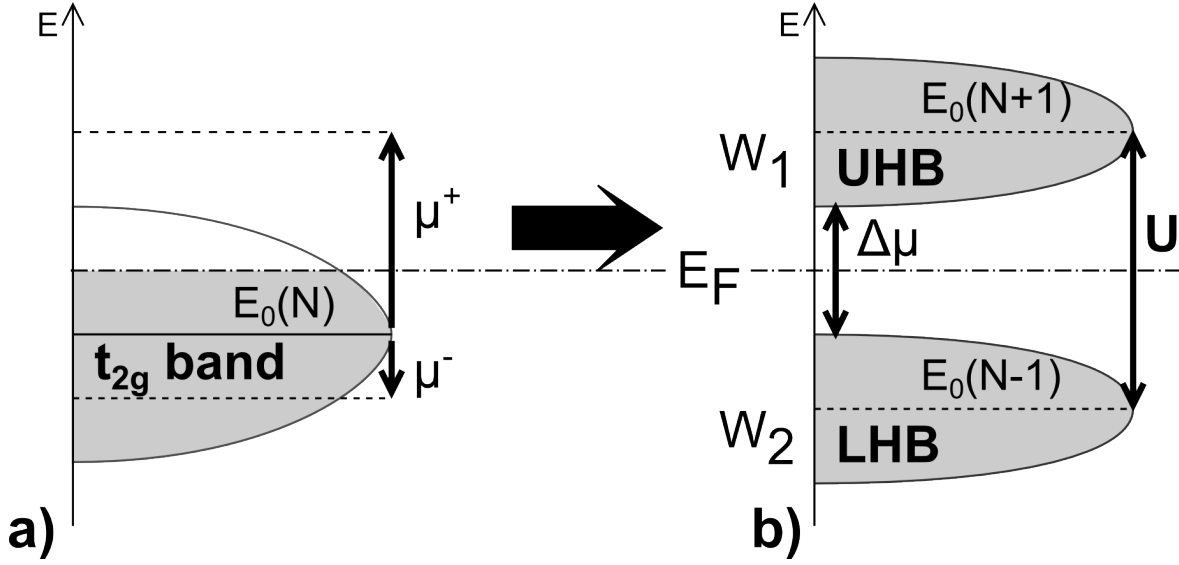


Figure 2.7 The Hubbard Model. (a) Half-filled electron system illustrated by a t_{2g} band of a 5d transition metal. (b) Formation of upper and lower Hubbard bands (*UHB* and *LHB*, respectively) as a consequence of strong Coulomb repulsions U in the half-filled electron system. (adapted from [57])

occurs and the system is an insulator if $W \ll U$ or equivalently $t \ll U$ (cf. Fig. 2.7). If the distance between the hydrogen atoms is reduced, their wave functions overlap more and the corresponding bandwidths increase. Eventually, the Hubbard bands overlap and the gap closes at around $U \approx W$. A metal-insulator transition occurs. The Hubbard model can at present only be solved analytically in one dimension. However, there are the following other limits of the model with exact solutions.

For $U = 0$ the model represents a simple metallic Fermi gas. In the atomic limit, $t = 0$, the system is an insulator since the lattice sites do not communicate with each other. As mentioned above, there is the limit of strong correlations $U \gg W$ and finite coupling t between lattice sites at half band filling $N = L$. Tunneling of carriers is taken as a second-order perturbation. In this case the Hubbard model is equivalent to the insulating antiferromagnetic Heisenberg model

$$H^{(2)} = \sum_{\langle ij \rangle} \frac{4t^2}{U} (\vec{S}_i \cdot \vec{S}_j - \frac{1}{4} n_i n_j) \quad (2.4)$$

with nearest neighbour exchange coupling $J = 4t^2/U$. Since at half filling $n_i = n_j = 1$, for parallel spin configurations ($\vec{S}_i \cdot \vec{S}_j = 1/4$) the energy goes to zero. Hopping of electrons with parallel spins is prohibited and as a result the system is antiferromagnetically ordered.

Above model is a one band model and in this sense only valid for an atom with a

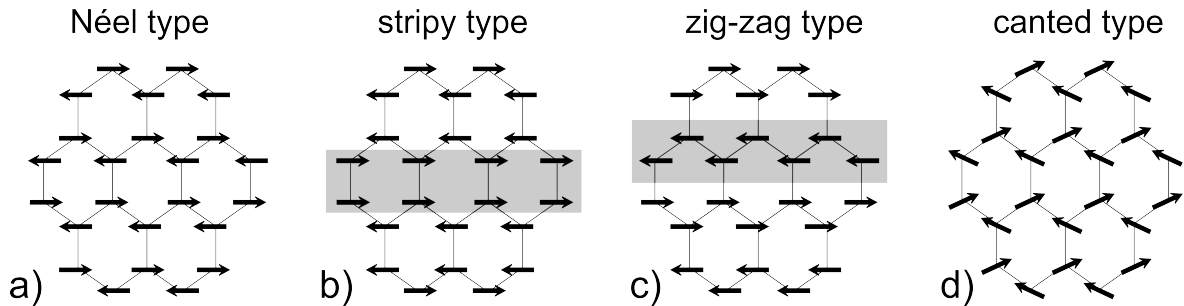


Figure 2.8 Possible antiferromagnetic-ordering patterns of the Ir-sublattice. The magnetic structures (a-d) shown are of Néel, stripy, zig-zag and canted type. The shaded boxes highlight the stripy and zig-zag chain elements. (adapted from [66])

single s orbital. Upon application of the model to d electron systems it is implicitly assumed that strong crystal fields lift the orbital degeneracy to such a degree that low-energy excitations can be described by a single band near the Fermi level. It is also assumed that the ligand p band is either far away from the relevant d band or so strongly hybridized with it as to effectively form a single band. For the description of more realistic situations the Hubbard model is hence often modified. Some of these modifications include non-zero hopping beyond nearest neighbour distance or additional nearest-neighbour interactions such as intersite Coulomb forces inside the screening radius that are otherwise neglected. Also for some transition metal compounds the oxygen p orbitals must be taken into account explicitly leading to the concept of charge transfer insulators [64].

Experiments on Na_2IrO_3 [65–67] showed zigzag-type magnetic order (Fig. 2.8c). However, in the strong coupling limit, the simple Hubbard model shows antiferromagnetic Néel-type order (Fig. 2.8a) in $d \geq 3$ dimensions. Zigzag-type order is also inconsistent with the $J_{eff} = 1/2$ hamiltonians derived where the effect of Coulomb repulsion within a Hubbard model description in the strong coupling limit was combined with a Kitaev hamiltonian of spin $1/2$ moments on a honeycomb lattice [13,18]. This so-called Heisenberg-Kitaev model shows apart from a desired spin liquid phase either Néel or stripy (Fig. 2.8b) order. For the Heisenberg-Kitaev model, that in its original form considers only nearest-neighbour Heisenberg exchange interactions, a zigzag-type order can manifest itself only upon inclusion of further neighbour exchanges [16,68,69]. However, it can be argued [70] that these further exchanges are hard to justify without lattice distortion rendering a $J_{eff} = 1/2$ unlikely. Furthermore, the proposed model for a topological insulator in the weak interaction limit [12] results in a canted antiferromagnet (Fig. 2.8d). In conclusion, the correct microscopic mechanism explaining the magnetic properties of Na_2IrO_3 has at present not been found.

2.4 Intrinsic Conductivity in Ideal Semiconductors

Motivated by experimental findings [4] in single crystals of Na_2IrO_3 associated with variable range hopping conductivity, this and the following sections intend to give an introduction to hopping conductivity in insulator and semiconductor materials. This section starts with a discussion of basic facts about semiconductors, especially intrinsic conduction in semiconductors. Subsequently, the focus will be set on conductivity in disordered solids, for which theories on hopping conductivity have originally been set up. Finally, the special case of variable range hopping conductivity will be reviewed. The discussion of hopping conductivity is mainly based on the extensive book by Shklovskii and Efros [71] "Electronic Properties of Doped Semiconductors".

An insulator is defined as having zero conductivity at zero temperature (and weak external fields), whereas a metal has a finite conductivity. Electrons in completely filled bands cannot conduct an electrical current and in an insulator all bands are either filled or empty. There exists an energy gap E_g separating the highest filled from the lowest empty band. Electrons can be thermally excited from the valence band across the band gap E_g into the conduction band leaving behind holes in the valence band. The conductivity is then a sum of electron and hole conduction

$$\sigma = -en_c\mu_e + ep_v\mu_h \quad (2.5)$$

The two types of charge carriers have a mobility μ . Mobility and the density of thermally excited electrons and holes n_c and p_v , respectively, are temperature dependent. Generally, the electrical conductivity is strongly increasing with temperature. Insulators are considered semiconductors if their magnitude of E_g is such that a thermal activation of charge carriers leads to a significant conductivity for instance at room temperature [56]. At high temperatures usual semiconductors possess an intrinsic electrical conductivity. It is due to thermal activation of charge carriers across the bandgap. In the following the intrinsic generation of charge carriers, that is the thermal generation and not generation due to defects, will be derived at thermal equilibrium.

One can define a carrier concentration at an energy E by the product of the density of states $g(E)$ and the Fermi-Dirac distribution function $f(E)$ as [73]

$$n(E) = g(E) \cdot f(E), \quad (2.6)$$

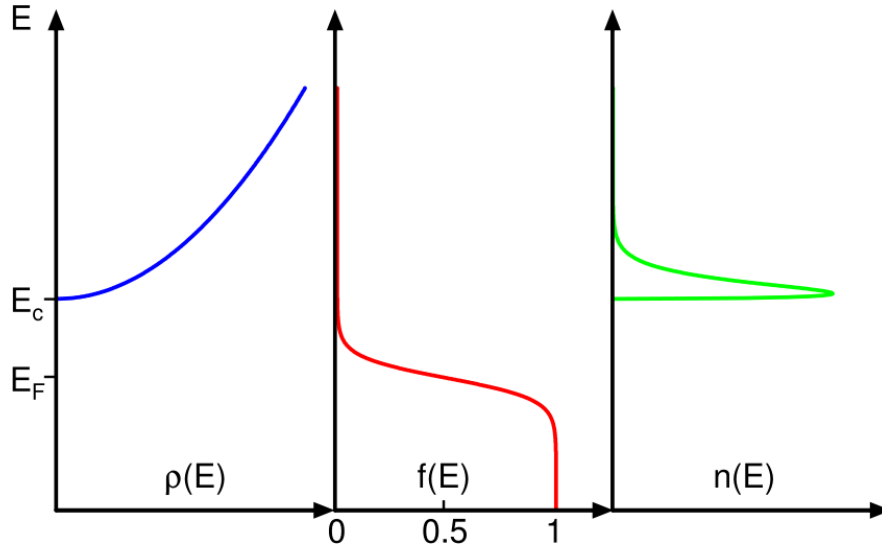


Figure 2.9 Density of states, Fermi-Dirac distribution function and free electron concentration of a non-degenerate semiconductor at energies above the valence band and in arbitrary units. (from [72])

where the distribution function is given as

$$f(E) = \frac{1}{\exp\left(\frac{E-\mu}{k_B T}\right) + 1} \quad (2.7)$$

and the density of states in three dimension as

$$g(E)_c = \frac{1}{2\pi^2} \left(\frac{2m_e^*}{\hbar^2}\right)^{3/2} \sqrt{E - E_C} \quad (2.8)$$

$$g(E)_v = \frac{1}{2\pi^2} \left(\frac{2m_h^*}{\hbar^2}\right)^{3/2} \sqrt{E_V - E}. \quad (2.9)$$

Figure 2.9 illustrates that for an ideal semiconductor the density of states is zero within the bandgap and also that most of the carriers are located within $3k_B T$ above and below the conduction and valence band edges, respectively [74]. Hence, an integration from the band edges to plus and minus infinity, respectively, yields the full concentration of charge carriers:

$$n_c = \frac{1}{2\pi^2} \left(\frac{2m_e^*}{\hbar^2}\right)^{3/2} \int_{E_C}^{\infty} dE \sqrt{E - E_C} \frac{1}{\exp\left(\frac{E-\mu}{k_B T}\right) + 1}, \quad (2.10)$$

$$p_v = \frac{1}{2\pi^2} \left(\frac{2m_h^*}{\hbar^2}\right)^{3/2} \int_{-\infty}^{E_V} dE \sqrt{E_V - E} \frac{1}{\exp\left(\frac{\mu-E}{k_B T}\right) + 1}. \quad (2.11)$$

$$(2.12)$$

Substituting $x = (E - E_C)/k_B T$ and $\zeta = (\mu - E_C)/k_B T$ for electrons and similarly $x = (E_V - E)/k_B T$ and $\zeta = (E_V - \mu)/k_B T$ for holes, one gets

$$n(E)_c = \frac{1}{2\pi^2} \left(\frac{2m_e^*}{\hbar^2} \right)^{3/2} (k_B T)^{3/2} \int_0^\infty dx \frac{x^{1/2}}{\exp(x - \zeta) + 1}, \quad (2.13)$$

$$p(E)_v = \frac{1}{2\pi^2} \left(\frac{2m_h^*}{\hbar^2} \right)^{3/2} (k_B T)^{3/2} \int_0^\infty dx \frac{x^{1/2}}{\exp(x - \zeta) + 1}. \quad (2.14)$$

There is no analytical solution to this integral but one can define the effective density of states at the band edges

$$N_c = 2 \left(\frac{2\pi m_e^* k_B T}{(2\pi\hbar)^2} \right)^{3/2}, \quad (2.15)$$

$$P_v = 2 \left(\frac{2\pi m_h^* k_B T}{(2\pi\hbar)^2} \right)^{3/2}. \quad (2.16)$$

An intrinsic semiconductor has a negligible amount of impurities, such that charge carriers in the conduction band can only originate from states in the valence band where they leave holes behind upon thermal activation. Consequently, the number of electrons and holes is equal:

$$n_c = p_v = n_i. \quad (2.17)$$

Equivalently, one can write the intrinsic carrier concentration n_i as $(n_c p_v)^{1/2}$. Then it follows

$$\begin{aligned} n_i(T) &= [N_c P_v]^{1/2} \exp\left(-\frac{E_C - E_V}{k_B T}\right) \\ &= 2 \left(\frac{2\pi k_B T}{(2\pi\hbar)^2} \right)^{3/2} (m_c m_v)^{3/4} \cdot \exp\left(\frac{-E_g}{2k_B T}\right). \end{aligned} \quad (2.18)$$

The intrinsic carrier concentration increases exponentially with increasing temperature. For a pure n -type semiconductor and mobility dominated by lattice scattering $\mu_{lattice} \propto T^{-3/2}$ the conductivity is $\sigma = -en_c\mu$, such that

$$\rho = \frac{1}{\sigma} \propto \rho_0 \exp\left(\frac{E_g}{2k_B T}\right). \quad (2.19)$$

In a measurement of temperature dependent resistivity, plotting $\ln\rho$ vs. $1/T$ yields a straight line from which the bandgap E_g can be estimated. This type of temperature dependence is often termed activated or Arrhenius behaviour. Arrhenius behaviour generally indicates an ideal, homogeneous and clean sample where thermal activation of carriers is the dominant transport mechanism. Due to the large activation energy $E_g/2$,

the intrinsic carrier concentration (2.18) decreases very rapidly with temperature. At lower temperatures free charge carriers gradually freeze out and the extrinsic properties of a semiconductor begin to dominate conduction processes. Eventually, conductivity is solely due to electrons hopping between localized sites close to the Fermi level.

2.5 Conductivity in Disordered Solids

Perfect crystalline material shows structural short- and long-range order. In band structure models this translational periodicity leads to a well-defined forbidden energy gap and sharp edges at the valence and conduction band. However, in disordered solids, such as amorphous or highly doped semiconductors, structural long-range order breaks down. In disordered systems, the translational and possible compositional disorder has to be taken into account in the proper variation of classical band structure models. One of these band structure models is the *Davis-Mott* model [75] leading to the conduction mechanism of variable range hopping (VRH) with a temperature dependence of $\ln\rho \propto 1/T^{1/4}$ [76]. A variable range hopping type conductivity has been reported for NaIr_2O_3 single crystals in a temperature regime between 100 K and 300 K [4] but also in the thin film samples investigated in this thesis (cf. Sec. 6.2). The variable range hopping mechanism is observed in many disordered or highly doped semiconductor materials. Among them are for instance single-crystalline Sr_2IrO_4 [77], single-crystalline $\text{InGaO}_3\text{ZnO}_5$ with intrinsic structural randomness [78], polycrystalline silicon films [79], boron doped silicon [80] and molecular beam epitaxial GaAs [81–83]. In the following the *Davis-Mott* model will be discussed. The subsequent section then deals with the mechanism of variable range hopping conductivity.

Davis-Mott Model The electronic structure of a crystal displaying perfect short- and long-range order is defined by a sharp energy gap between abruptly terminating valence and conduction bands. Within these bands, electronic states are extended, i.e. their wavefunctions occupy the entire volume. In variance to perfect crystals, amorphous and highly disordered material shows no long-range order. Also, the short-range order, that is interatomic distances and bond angles, can be slightly changed. Those spatial fluctuations in the otherwise periodic potential lead to localized states that form band tails reaching into the energy gap. These states are localized in the sense, that at zero temperature an electron will not diffuse to other regions in the crystal with similar potential fluctuations [84]; in other words, the mobility in localized

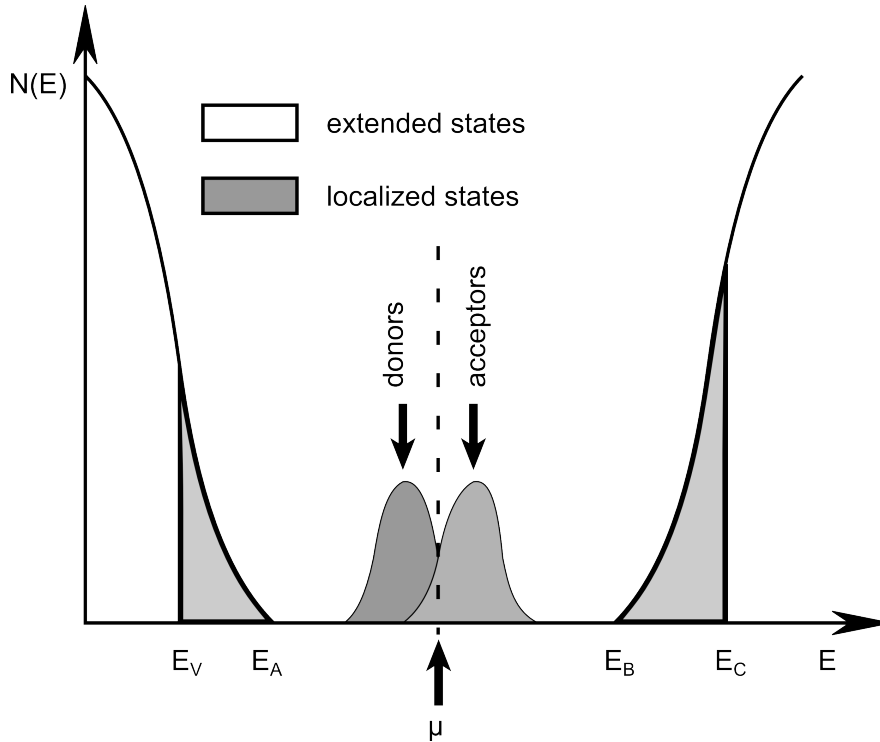


Figure 2.10 Schematic density of states diagram for amorphous semiconductors according to the *Davis-Mott* model. In grey are the localized states in the band tails and in the middle of the mobility gap. (adapted from [85])

states is zero at $T = 0$.

In the *Davis-Mott* model [75], the band tails are rather narrow and only extend to a couple of meV into the gap. Furthermore, there exists a band of compensated levels near the middle of the band gap caused by defects (cf. Fig. 2.10). Moreover, this center band is split into an acceptor and donor band pinning the Fermi level μ to the middle of the gap. There is a sharp transition from extended to localized states at E_V and E_C , respectively, where the mobility drops by several orders of magnitude. This in turn creates a so-called mobility edge. The pseudogap between E_V and E_C is hence defined as a mobility gap in the model. On the basis of the *Davis-Mott* model, three conduction processes can be devised that will each dominate at different temperature regimes.

At very low temperatures, carriers will tunnel between localized states at the Fermi level via thermal activation. For higher temperatures excitation of carriers into the localized states of the band tails occurs. There, carriers can conduct charge only via hopping processes. Finally at even higher temperatures, carriers are excited across the mobility edge into extended states with much higher mobility. Transport inside the extended states is equivalent to band conduction as discussed in section 2.4 and

results in an activated behaviour, although the preexponential factors σ_0 or ρ_0 , respectively, differ. In the following, transport inside the extended states will be discussed in greater detail to illustrate the differences to intrinsic conduction in ideal and ordered semiconductors.

Conduction in Extended States The general expression of conductivity in any semiconductor is [85]

$$\sigma = -e \int g(E)\mu(E)kT \frac{\partial f(E)}{\partial E} dE. \quad (2.20)$$

Above expression can be rewritten using

$$\frac{\partial f(E)}{\partial E} = -f(E)[1 - f(E)]/kT, \quad (2.21)$$

and σ can be written as

$$\sigma = e \int g(E)\mu(E)f(E)[1 - f(E)]dE. \quad (2.22)$$

In the *Davis-Mott* model, one makes the assumption, that the Fermi level is situated in the middle of the gap sufficiently far away from the band edges - i.e. $E_C - \mu \gg k_B T$. Consequently, one can use Boltzmann statistics to express $f(E)$. Furthermore, inside the extended states a constant density of states $g(E_C)$ and mobility μ_C is assumed. Hence, the conductivity due to electrons excited into extended states reads as

$$\sigma = eg(E_C)kT\mu_C \exp[-(E_C - \mu)/kT], \quad (2.23)$$

where μ_C is the average mobility in the extended states above E_C and μ is the Fermi level. It can be shown that in this model the average mobility $\mu_C \propto 1/T$ [85] and the expression (2.23) for the conductivity transforms into

$$\sigma = \text{const} \cdot \exp[-(E_C - \mu)/kT] \quad (2.24)$$

The band gap is assumed to be linearly decreasing with temperature, i.e.

$$E_C - \mu = \frac{E(0)}{2} - \gamma T \quad (2.25)$$

such that in the end the conductivity in the extended states can be written as

$$\sigma = \sigma_0 \exp[-E(0)/2kT], \quad (2.26)$$

where $\sigma_0 = eg(E_C)kT\mu_C\exp(\gamma/k)$. The preexponential factor σ_0 is temperature independent, however, its exact form depends on the approach chosen to calculate the mobility μ_C in the extended states [85]. In conclusion, also for highly disordered systems an Arrhenius type activated behaviour of conductivity (cf. Sec. 2.4) can be expected in a sufficiently high range of temperatures, but with a different prefactor σ_0 .

2.6 Variable Range Hopping

The *Davis-Mott* model discussed in the preceding section predicts the Fermi level μ_F to lie in a narrow band of localized states where conduction can occur via thermally activated and phonon-assisted hopping. The main ingredients of hopping theory are localized states on donor and/or acceptor sites. Their wavefunction overlap and the interaction with phonons leads to infrequent jumps. Miller and Abrahams [86] proposed a model of a random resistance network to approach electron hopping. Some main ideas of this idea will be presented in order to arrive at a quantitative derivation of variable range hopping via percolation theory [71].

The Random Resistance Network In the following approach electrons are localized on individual donors. There exists a probability of an electron hopping from site i to j assisted by a phonon with energy ϵ_{ij} . The sites are separated by a distance r_{ij} and the electrons localization radius on these sites is denoted by a . In the absence of an electric field, the number of transitions from i to j and that of the reverse process is equal. Application of a weak external field breaks this balance giving rise to a net current that is proportional to the applied field. From this current, the resistance R_{ij} of the transition can be extracted. Miller's and Abrahams model is eventually reduced to calculating the conductivity of a network of random resistors completely determined by the resistances R_{ij} between the network's vertices [71]. The resistance R_{ij} between two sites is given by

$$R_{ij} = \frac{kT}{e^2\Gamma_{ij}}, \quad (2.27)$$

where Γ_{ij} is the number of transitions per unit time at equilibrium, i.e. without externally applied field. At sufficiently low temperatures the transition frequency is proportional to

$$\Gamma_{ij} \propto \exp\left(-\frac{2r_{ij}}{a}\right) \exp\left(-\frac{\epsilon_{ij}}{kT}\right). \quad (2.28)$$

In the above definition of the transition frequency, the first exponential term represents the probability of electron transfer from one state to another. It is dependent on the overlap of wave functions. The probability of finding a phonon with excitation energy equal to ϵ_{ij} is contained in the second exponential term. In turn, this excitation energy is given by

$$\epsilon_{ij} = \frac{1}{2} [|\epsilon_i - \epsilon_j| + |\epsilon_i - \mu| + |\epsilon_j - \mu|], \quad (2.29)$$

and μ is the Fermi level. Some of the above notions will now be used to give a qualitative derivation of variable range hopping. However, the same notions are important also for a quantitative approach on variable range hopping by means of a percolation method.

A qualitative Approach According to the *Davis-Mott* model, at sufficiently low temperatures conduction is due to hopping between states inside a narrow band near the Fermi level. Mott showed [76] that for a non-vanishing density of states at the Fermi level the temperature dependent resistivity is given by Mott's law of variable range hopping (VRH):

$$\rho(T) = \rho_0 \exp[(T_0/T)^{1/4}], \quad \text{where} \quad (2.30)$$

$$T_0 = \frac{\beta}{kg(\mu)a^3}, \quad (2.31)$$

with β a numerical coefficient. For the qualitative derivation, one considers a system with states localized in the vicinity of the Fermi level (cf. Figs. 2.10 and 2.11). Since the definition of the resistance R_{ij} contains the factor $\exp(\epsilon_{ij}/kT)$ (cf. eqs. (2.27) & (2.28)), it is argued that at very low temperatures only the resistances with very small ϵ_{ij} contribute to conductivity. Otherwise, for larger ϵ_{ij} the resistances are considered too large to allow for a significant contribution to conduction. This restraint on ϵ_{ij} requires that the relevant states ϵ_i lie in a *narrow* band which is symmetric around the Fermi level (Fig. 2.11), i.e.

$$|\epsilon_i - \mu| \leq \epsilon_0, \quad (2.32)$$

as can be illustrated by eq. (2.29): the first term inside the brackets corresponds to the width of the band, the second and third terms express the distance to the Fermi level. Having established this narrow band, its density of states is furthermore set constant and non-zero, i.e. $g(\epsilon) = g(\mu)$ at low temperatures. Then, the concentration of states inside the band is given by

$$N(\epsilon_0) = 2g(\mu)\epsilon_0. \quad (2.33)$$

Now, to formulate an estimate of the system's resistivity, equations (2.27) and (2.28)

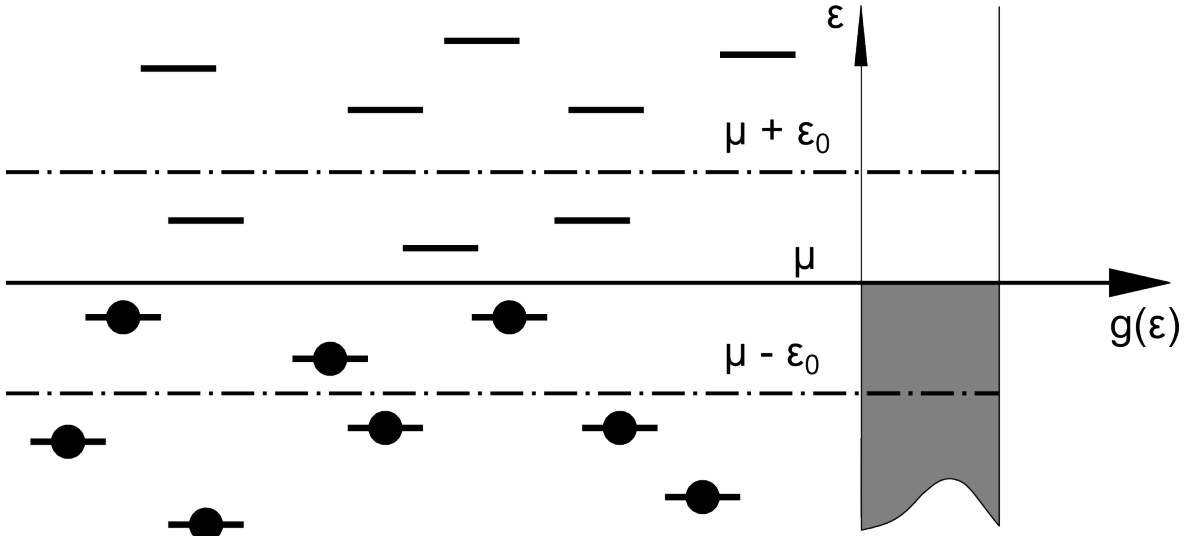


Figure 2.11 Construction of a symmetric band containing localized states that are separated from the Fermi level μ by less than ϵ_0 . The density of states shown on the right is constant with occupied states shaded in grey. (adapted from [71])

are combined. Also the distance between sites r_{ij} and ϵ_{ij} are replaced by $[N(\epsilon_0)]^{1/3}$ and ϵ_0 , respectively. Ignoring numerical coefficients, one finally obtains for the resistivity corresponding to the narrow band:

$$\rho = \rho_0 \exp \left[\frac{1}{N^{1/3}(\epsilon_0)a} + \frac{\epsilon_0}{kT} \right] = \rho_0 \exp \left[\frac{1}{[g(\mu)\epsilon_0]^{1/3}a} + \frac{\epsilon_0}{kT} \right]. \quad (2.34)$$

If we analyze the dependence $\rho(\epsilon_0)$ (cf. Fig. 2.12), we see that for very low T there is a minimum in the resistivity, that corresponds to an optimal bandwidth

$$\epsilon_0 = \epsilon_0(T) \equiv \frac{(kT)^{3/4}}{[g(\mu)a^3]^{1/4}}. \quad (2.35)$$

It is assumed that the conductivity in its entirety is determined in order of magnitude by the optimal band. Then, substituting (2.35) into (2.34) one obtains Mott's law of variable range hopping (2.30) and the expression for (2.31) T_0 , where the numerical coefficient β remains indeterminable by above arguments. The derivative $d(\ln\rho)/d(kT)^{-1}$ is called the activation energy at a given temperature. It can be shown to be equal to ϵ_0 in order of magnitude and hence decreases monotonically with $T^{3/4}$. Moreover, from (2.33) and (2.35) one discovers how the average hopping distance \bar{r} , that is the average distance r_{ij} between states in the optimal band, varies with temperature:

$$\bar{r} \approx [g(\mu)\epsilon_0(T)]^{1/3} \approx (T_0/T)^{1/4}, \quad (2.36)$$

hence the name *variable* range hopping.

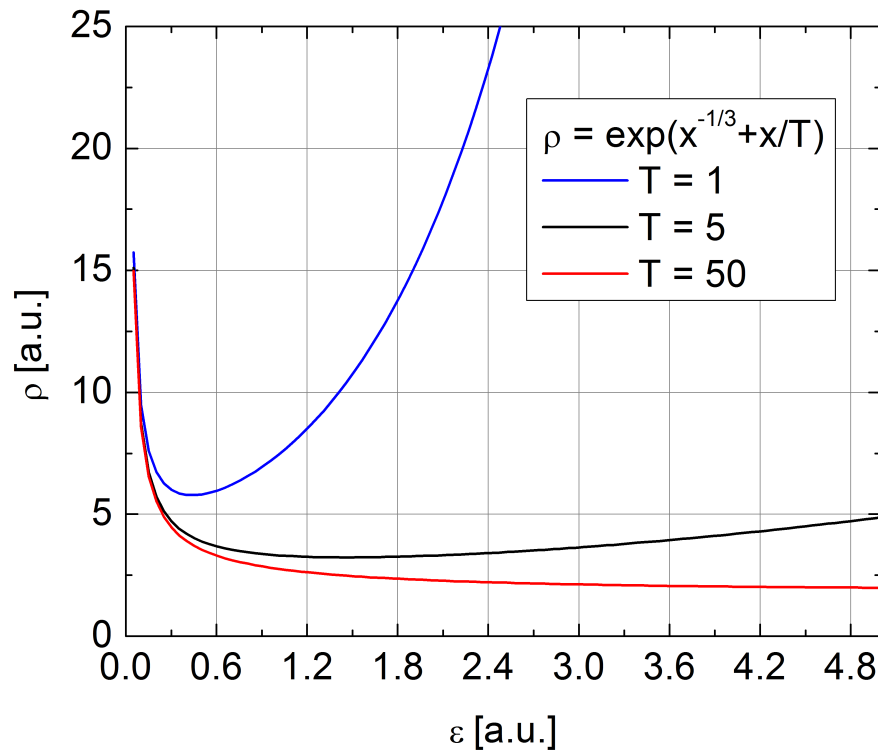


Figure 2.12 Schematic illustration of resistivity of a system with localized states inside a narrow band in the vicinity of the Fermi level as given by eq. (2.34).

A more rigorous approach Applying percolation theory to variable range hopping [71,87] not only yields the same expression as (2.30) but can also quantitatively derive a value for the numerical coefficient β in eq. (2.31).

Coming back to the random resistance network, we apply a random site problem to our network. We can define a bonding criterion, that if fulfilled allows for clusters of connected resistances spanning the entire system. In other words, there exist conducting channels in our sample. For the random resistance network we relate the exponential temperature dependence of resistivity (2.27) to the bonding criterion as

$$\frac{2r_{ij}}{a} + \frac{\epsilon_{ij}}{kT} \leq \xi \quad (2.37)$$

with percolation threshold ξ_c . The percolation threshold describes the point, at which the systems still contains one complete conducting channel. As a consequence of the bonding criterion, there exist a maximal hopping distance and energy, respectively:

$$\epsilon_{\max} = kT\xi \quad \text{and} \quad r_{\max} = \frac{a\xi}{2}. \quad (2.38)$$

It can furthermore be shown [71] that the percolation threshold ξ_c behaves as

$$\xi_c = \left[\frac{4n_c}{g(\mu_F)kT a^3} \right]^{1/4}, \quad (2.39)$$

where n_c is the critical concentration of sites at which percolation first occurs. With the hopping conductivity expressed as $\rho = \rho_0 \exp(\xi_c)$ within the percolation approach (cf. eq. (2.34)), one obtains the expression of the form of Mott's law (2.30). Moreover, one has [71]

$$\beta = 4n_c = 21.2 \quad (2.40)$$

Furthermore, the percolation method enables one to determine a critical temperature T_C above which Mott's law of variable range hopping may not hold. Still, the density of localized states inside the narrow band of width $2\Delta\epsilon$ is a constant $g(\epsilon) = N/2\Delta\epsilon$, where N is the number of states per unit volume. Outside a distance $\Delta\epsilon$ from the Fermi level it abruptly vanishes. However, within the percolation approach one can state that Mott's law (2.30) will hold provided $\epsilon_{\max} < \Delta\epsilon$. Hence, one can define the critical temperature as

$$kT\xi_c(T_c) = \Delta\epsilon. \quad (2.41)$$

Now, using (2.39), (2.40), and (2.41) one finds

$$T_c = 0.29 \Delta\epsilon (N^{1/3} a) k^{-1} \quad (2.42)$$

Above this temperature T_c there is a gradual transition from variable range hopping to nearest neighbour (NN) hopping of the form

$$\rho = \rho_0 \exp(E_a/kT) \quad (2.43)$$

with activation energy E_a being independent on temperature. For NN-hopping temperatures are such that in equation (2.34)

$$\frac{\epsilon_{ij}}{kT} \ll \frac{2r_{ij}}{a} \quad (2.44)$$

and resistivity is minimal for nearest neighbours.

Up to now, the density of states has been considered constant within a finite interval around the Fermi level. However, upon inclusion of significant Coulomb interactions, the density of localized states vanishes in the vicinity of the Fermi level forming a Coulomb gap U . Obviously, this is expected for a Mott insulator and in particular in

Na_2IrO_3 . In this situation the variable range hopping conductivity has the form [71]

$$\sigma \propto \exp \left[- \left(\frac{T_1}{T} \right)^{1/2} \right]. \quad (2.45)$$

The variable range hopping conductivity above can generally be expressed as

$$\rho(T) = \rho_0 \exp[(T_0/T)^p], \quad \text{where } 0 < p < 1. \quad (2.46)$$

In the course of this discussion, we have already encountered $p = 1/4$ and $p = 1/2$. For an analysis of experimental data, it is convenient to introduce the dimensionless activation energy $W \equiv T d \ln(\rho) / dT$. When above law (2.46) holds, one must have

$$\ln W = -p \ln T + \text{const} \quad (2.47)$$

so that in a log-log plot a detailed discussion of p or potentially $p(T)$ is possible.

3 Review and Properties of Single and Polycrystalline Na_2IrO_3

The first synthesis of NaIr_2O_3 powder was reported in 1974 [88] in a study of equilibrium phase relations for the $\text{Na}_2\text{O}-\text{IrO}_2$ system in air using the quenching technique. It was found there, that NaIr_2O_3 dissociates at 1235°C . An X-ray powder pattern was indexed on the basis of the monoclinic $C2/c$ space group. The JCPDS database diffraction pattern (Sec. A.6) as used in this work is based upon the 1974 data.

In the past two years, again experimental effort has been made to synthesize and study Na_2IrO_3 single crystals and polycrystalline samples. First experimental efforts on single crystalline Na_2IrO_3 have been published in 2010 and have since continued. Early powder X-ray diffraction experiments [4] on single crystals and polycrystalline samples suggested a monoclinic $C2/c$ unit cell with asymmetrically-distorted IrO_6 octahedra. The layered perovskite structure is made up of layers containing only Na atoms alternating with NaIr_2O_6 layers stacked along the c axis. Within the NaIr_2O_3 layers the edge sharing IrO_6 octahedra form a honeycomb lattice, while the Na atoms occupy the voids between the IrO_6 octahedra (Fig. 3.1(a,b)).

However, two more recent single-crystal x-ray diffraction experiments see a better match for the X-ray diffraction data with the space group $C2/m$ [66,67]. Also, in the $C2/m$ structure the IrO_6 octahedra are much more symmetric without three distinct $\text{Ir}-\text{O}$ bond lengths as previously reported. Structural disorder was also investigated in all three reports and established as a common feature. For instance, the probability of faults in the stacking sequence along the c -axis was indeed found to be $1/10$, i.e. one stacking fault every ten NaIr_2O_6 layers [66]. Moreover, a substantial site mixing between Na and Ir within the NaIr_2O_6 layers is deemed likely [4]. The structural distortions found, i.e. the slight flattening of the IrO_6 octahedra perpendicular to layer stacking, indicate the presence of the trigonal crystal field in addition to the cubic crystal field (Fig. 3.1(c)). This in turn has consequences for the proper determination of the electronic band structure (cf. section 2.3). The structural parameters of the monoclinic $C2/m$ unit cell vary slightly between the two reports at 300 K [66] and 125 K [67], probably due to the different temperatures. Table 3.1 shows the range of measured structural parameters.

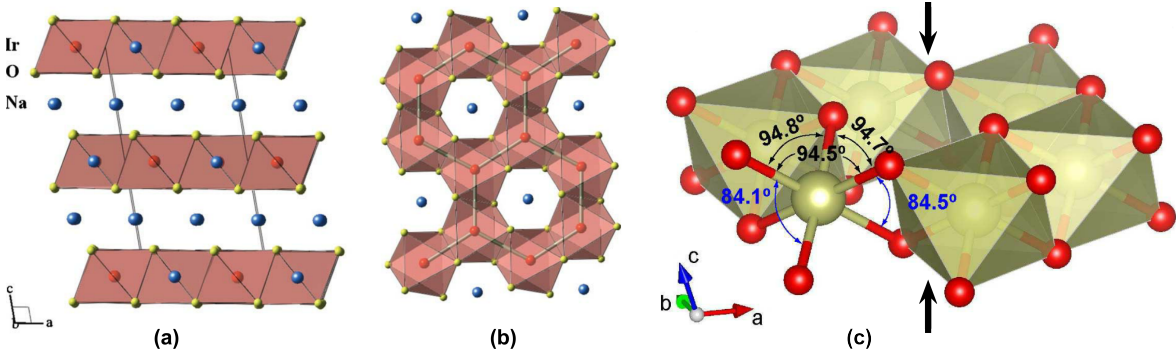


Figure 3.1 Crystal structure of NaIr_2O_6 . (a) View perpendicular to the c axis showing the layered perovskite structure where Na-only layers alternate with slabs of NaIr_2O_6 . (b) View onto the basal plane within a NaIr_2O_6 layer highlighting the honeycomb lattice formed by Ir atoms. The Na, Ir and O atoms in (a) and (b) are shown as blue, red and yellow spheres respectively. (c) Local structure within the basal plane. Black arrows indicate the compression of IrO_6 octahedra due to trigonal distortions causing the decrease of O-Ir-O bond angles across the shared edges. ((a) and (b) from [4], (c) from [67])

Table 3.1 Structural parameters of $C2/m$ monoclinic unit cell in Na_2IrO_3 extracted from X-ray diffraction data obtained from the studies as indicated.

lattice parameters:	$a[\text{\AA}]$	$b[\text{\AA}]$	$c[\text{\AA}]$	β [$^\circ$]
ref. [88]($C2/c$)	5.418	9.394	10.765	99.58
ref. [4]($C2/c$)	5.426	9.386	10.769	99.58
ref. [66]($C2/m$)	5.427	9.395	5.614	109.04
ref. [67]($C2/m$)	5.319	9.215	5.536	108.67

Temperature dependent measurements of resistivity in the range between $T=80$ K and 350 K were performed [4]. The data could not be fit with an activated behaviour $\rho(T) \propto \exp(-\Delta/T)$. Instead, the data follows a $\rho(T) \propto \exp[(\Delta/T)^{1/4}]$ behaviour between 100 K and 300 K (Fig. 3.2(a)). This kind of behaviour was associated with three dimensional variable range hopping (VRH) of carriers localized by disorder (cf. Sec. 2.6).

The onset of antiferromagnetic ordering below temperatures of about 15 K was determined experimentally with resonant X-ray scattering at $T_N = 13.3$ K [65] and with neutron scattering at $T_N = 15.3$ K [66] and $T_N = 18.1$ K [67]. Moreover, the Curie-Weiss temperature is about $\Theta \approx -116$ K (cf. Fig. 3.2(b)). In turn, the ratio $\Theta/T_N \approx 8$ indicates the presence of substantial geometrical magnetic frustration. The high-temperature magnetic susceptibility is anisotropic; the out-of-plane susceptibility being slightly larger than the in-plane one. This anisotropy could originate from trigonal distortions of the IrO_6 octahedrons [4]. The magnetic specific heat is suppressed at low temperatures and shows a lambda-like anomaly at $T_N=15$ K indicating bulk

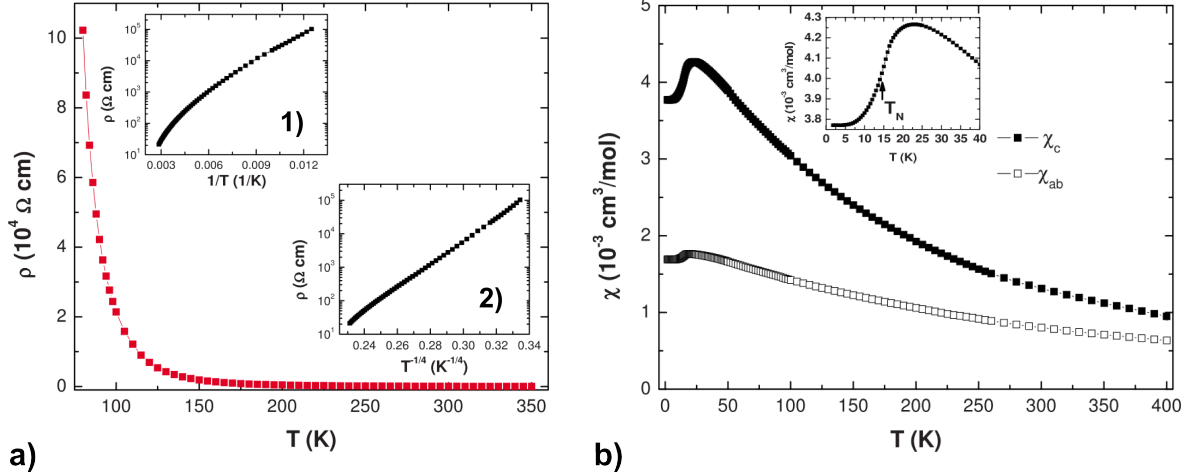


Figure 3.2 (a) In-plane electrical resistivity ρ versus temperature T from 80 K to 300 K for a single crystal Na_2IrO_3 . The insets 1) and 2) show the ρ versus $1/T$ and ρ versus $T^{-1/4}$ dependencies, respectively. (b) Anisotropic out-of-plane and in-plane magnetic susceptibility data χ_c and χ_{ab} versus T . The inset shows the $\chi_c(T)$ data at low T highlighting a broad maximum at about 23 K. The arrow indicates the Néel temperature at T_N at 15 K, i.e. the onset of long-ranged antiferromagnetic ordering. (from [4])

magnetic ordering [4]. A recent resonant X-ray scattering experiment [65] suggests that the magnetic order is collinear with a large projection along the a direction [65]. In the same report, a combination of these experimental findings and density functional theory (DFT) calculations strongly suggest a zig-zag antiferromagnetic-ordering pattern (cf. Fig. 2.8) for the magnetic moments [65]. The zig-zag pattern has since been confirmed independently using neutron scattering [66, 67].

Another recent study [89] on Na_2IrO_3 combined angle-resolved photoelectron spectroscopy (ARPES), optical conductivity and band structure calculations. It was found that the Ir $5d-t_{2g}$ bands are narrow (~ 100 meV) due to structural and atomic disorder. An estimation of the band gap of at least 330 meV was possible with angle-integrated photoemission spectroscopy (PES) and the observation of chemical potential shift with carrier doping. Here, carrier doping introduces electrons across the gap and induces an occupation of the conduction band. Complementary measurements of optical conductivity revealed the starting of an absorption edge at 300-400 meV at 300 K (Fig. 3.3(b)). The gap has a negligible temperature dependence down to 8 K. In conclusion, the converging analysis of ARPES and optical conductivity indicate an insulating band gap of about 350 meV. Further LDA band structure calculations reproduced the experimental findings. Here, with the inclusion of SOC (485 meV) and U (3 eV) a gap of 365 meV was introduced. In conclusion, it was also shown that for Na_2IrO_3 the Mott criterion $U > W$ is fulfilled due to the narrow bandwidth of the Ir $5d-t_{2g}$ states. The study establishes Na_2IrO_3 as the proposed novel type of correlated Mott insulator

where SOC and Coulomb repulsion play equal roles.

As was shown reported experimental efforts on Na_2IrO_3 are up to now limited to powder and single-crystalline samples. Studying the feasibility and properties of Na_2IrO_3 thin films is thus a next step closer to a possible application of this novel material.

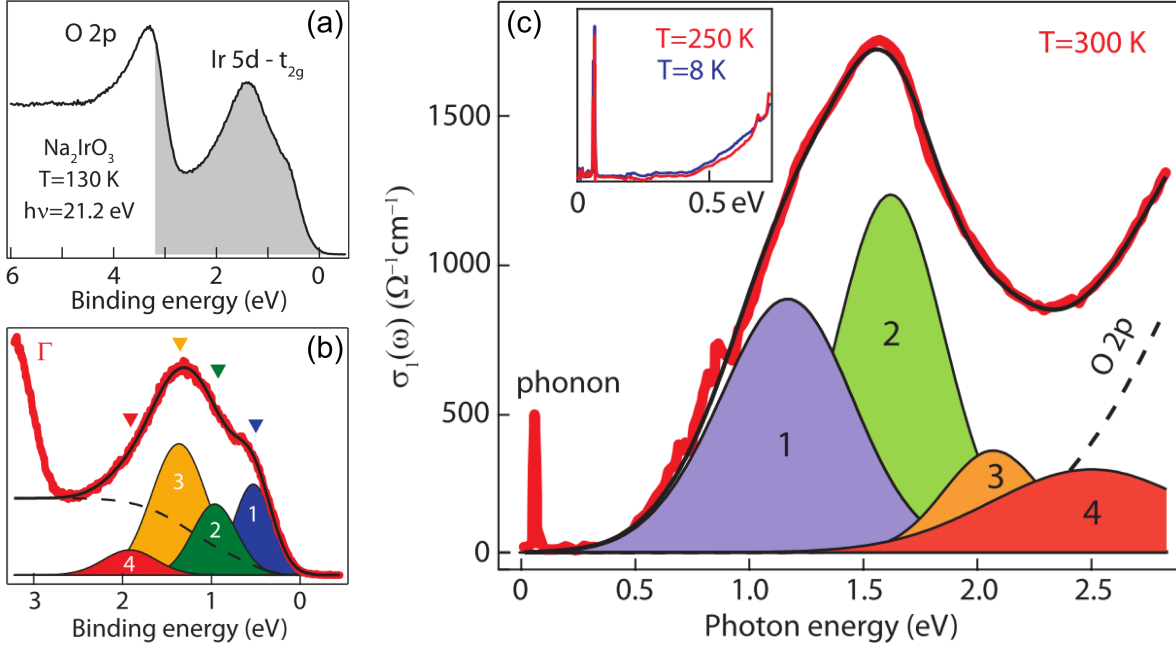


Figure 3.3 (a) Angle-integrated O and Ir valence-band photoemission spectrum of Na_2IrO_3 . The grey area represents the energy range shown in (b). (b) Energy distribution curve (EDC) along the Γ -point. The curve was modeled with four Gaussian peaks as components of the Ir $5d-t_{2g}$ valence band manifold (black line). (c) Optical conductivity data at 300 K (red line) reveals the starting of an absorption edge at 300-400 meV. Also shown is the simulated Ir $5d-t_{2g}$ joint particle-hole DOS (black line) together with its four individual components as obtained from the simultaneous fits of ARPES (b) and optical conductivity data. The inset shows the temperature dependence of the gap edge. (from [89])

4 Experimental Methods

For a thorough study of structural, optical and electrical properties of Na_2IrO_3 thin films, several experimental methods were employed. Among these methods are X-ray diffraction, atomic force microscopy, scanning electron microscopy and energy dispersive X-ray spectroscopy for the study of film growth and structural parameters. Optical properties were determined by transmission spectroscopy, Fourier transform infrared spectroscopy and optical conductivity. Furthermore, temperature dependent electrical properties were investigated by measurements of resistivity and resistance. In the following, select methods are discussed in some more detail.

4.1 X-ray Diffraction

X-ray diffraction (XRD) on crystals for the purpose of structural and epitaxial studies is based on the Bragg condition [90]

$$\Delta s = 2d_{hkl}\sin\theta = n\lambda \quad (4.1)$$

Electromagnetic radiation with wavelength λ comparable to interatomic distances in a crystalline solid scatters from lattice planes with spacing d_{hkl} and interferes constructively upon fulfillment of the Bragg condition. This is the case when the path difference Δs between the scattered waves is an integer multiple of $n\lambda$ (Fig. 4.1). In a X-ray diffraction pattern, high intensity Bragg peaks mark the satisfaction of the Bragg condition.

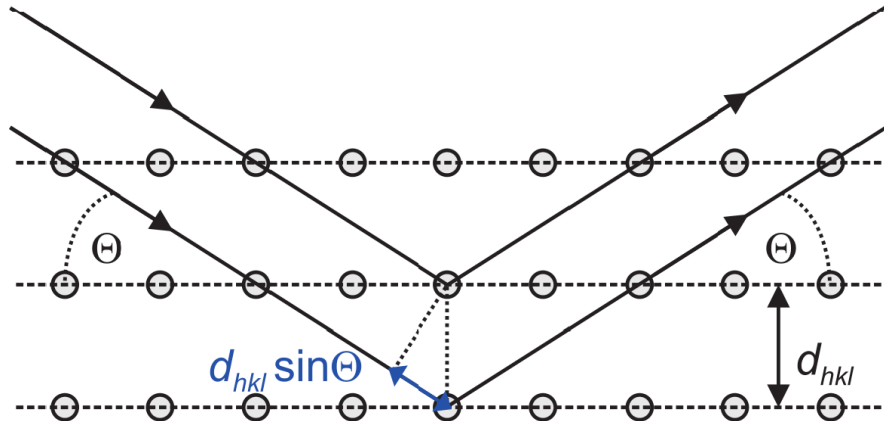


Figure 4.1 Reflection of X-ray radiation from lattice planes with spacing d_{hkl} . (from [91])

In the experiments, a Phillips X'Pert diffractometer was employed. The system consists of two separate goniometers (Fig. 4.2(a): a wide-angle goniometer in Bragg-Brentano geometry [90] (wide-angle XRD) and a high-resolution goniometer (HR-XRD). X-ray radiation is emitted in both cases from a copper anode with $\lambda(\text{Cu-}K_{\alpha 1}) = 1.5406\text{\AA}$. The radiation is not fully monochromatic in the wide-angle XRD and further contains $\text{Cu-}K_{\alpha 2}$ and $\text{Cu-}K_{\beta}$ lines, which are always visible in a XRD pattern. In contrast, the light path in HR-XRD is different and allows for monochromatic radiation by means of a Bartels monochromator [90].

The Bragg-Brentano geometry of the wide-angle XRD allows for the rotation about two Euler angles (ω, ϕ , cf. Fig 4.2(b)). In HR-XRD, the sample holder and detector of the goniometer can in principle be rotated about all three Euler angles (ω, ϕ & ψ), thus offering the flexibility to also measure those skew-symmetric and asymmetric reflections which are not accessible in wide-angle XRD.

With the wide-angle goniometer, 2θ - ω -scans were performed, where the detector is rotated twice as fast as the sample holder around one and the same axis. The axis is in-plane to the samples surface. In this way, all lattice planes oriented normal to the growth direction can be measured (symmetric reflexes). A 2θ - ω -scan yields information about the separation of lattice planes and depending on the type of unit cell information about lattice constants. From the intensity of the peaks one can qualitatively deduce the number of lattice planes oriented normal to the growth direction. The relation between the lattice parameters a , b , c and β of a monoclinic unit cell and a given d spacing d_{hkl} is given as [90]

$$\frac{1}{d_{hkl}^2} = \frac{h^2}{a^2 \sin^2 \beta} + \frac{k^2}{b^2} + \frac{l^2}{c^2 \sin^2 \beta} + \frac{2hl \cos \beta}{ac \sin^2 \beta}. \quad (4.2)$$

All 2θ - ω X-ray diffraction patterns were recorded in a range from 10° to 110° , with a step size of 0.025° , a counting time of 0.5 s per step and with 25 kV and 20 mA X-ray tube setting. Employing the high-resolution goniometer, one can measure a rocking curve, also ω -scan, where the diffractometer is set to a specific angle θ of a symmetric or asymmetric reflex and the detector is rotated about ω . The full width at half maximum (FWHM) of thusly measured symmetric and asymmetric reflexes is a measure for the tilt and twist of crystallites, respectively. The smaller the FWHM is, the better the crystallites are aligned and the larger their size.

For a thin film grown on a substrate, the in-plane epitaxial relationship between film and substrate can be studied by a ϕ -scan. The sample is rotated about ϕ normal to the

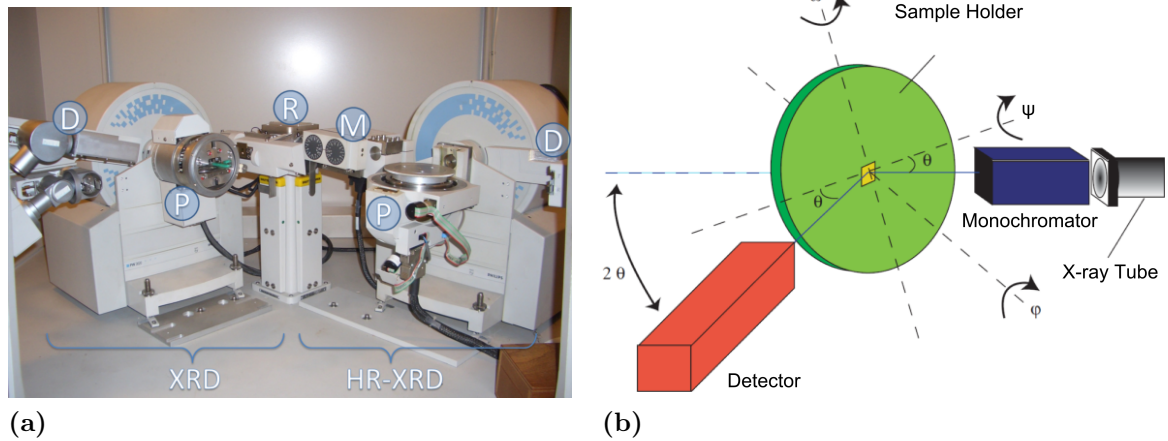


Figure 4.2 (a) Phillips X'Pert diffractometer with X-ray tube (R) and the wide-angle and high-resolution goniometers on the left and the right. (P) and (D) denote sample holders and detectors, resp. (M) denotes the Bartels monochromator of the HR-XRD goniometer. (b) Illustration of a HR-XRD diffractometer setup and the three Euler angles. (from [92])

sample surface. Sample and detector were previously set to the Bragg angle of a specific lattice plane. Then, a ϕ -scan about 360° reveals multiple reflections depending on the symmetry of the underlying lattice. To exemplify, c-plane sapphire has hexagonal in-plane symmetry and a ϕ -scan about the asymmetric (10-14) reflection usually shows six equally spaced reflections. HR-XRD measurements were performed with X-ray tube settings of 40 kV and 30 mA and with open receiving slit.

In conclusion, XRD measurements are a crucial tool to investigate the crystalline quality of the Na_2IrO_3 thin films. For data evaluation, the following software by *PANalytical* was used: *X'Pert HighScore 2.2.1* and *X'Pert Data Viewer 1.2f*.

4.2 Atomic Force Microscopy (AFM)

For the investigation of Na_2IrO_3 thin film properties a single crystalline and very smooth sample is required. Surface roughness has been measured with atomic force microscopy (AFM). A tip attached to a cantilever is traced over the sample surface in non-contact mode. The tip-surface distance is small such that Van-der-Waals (VdW) forces act on the cantilever. A Piezo element oscillates the cantilever slightly above its resonance frequency at a certain amplitude. Acting VdW forces alter resonance frequency and amplitude, subsequently. The original oscillation of the cantilever is maintained via a feedback loop by feeding back the oscillation signal of the cantilever via a piezo element with a phase shift of 90° . With the help of the feedback loop the

amplitude and frequency is kept constant by adjusting the height of the cantilever. From the height of the cantilever the topography of the sample surface in the chosen xy-plane can be extracted. Height and motion of the cantilever are being registered by laser light that is deflected from the cantilever onto a quadrant photodiode. AFM measurements were performed on a Park System XE-150 microscope with a silicon tip and cantilever.

Important parameters for the determination of surface roughness and quality are peak-to-valley height, root mean squared (RMS) roughness and the roughness average (R_a) value. Peak-to-valley height is the difference between highest and lowest point inside the scanned area. RMS and R_a roughness are defined as

$$\begin{aligned} RMS &= \sqrt{\frac{1}{m \cdot n} \sum_{k=1}^m \sum_{l=1}^n [z(x_k, y_l) - \mu]^2} \\ R_a &= \frac{1}{m \cdot n} \sum_{k=1}^m \sum_{l=1}^n |z(x_k, y_l) - \mu| \\ \mu &= \frac{1}{m \cdot n} \sum_{k=1}^m \sum_{l=1}^n z(x_k, y_l) \end{aligned} \quad (4.3)$$

where μ is mean height, $z(x_k, y_l)$ is the pixel height and $m \cdot n$ is the pixel number.

4.3 Scanning Electron Microscopy (SEM) and Energy Dispersive X-ray Spectroscopy (EDX)

Scanning electron microscopy (SEM) and energy dispersive X-ray spectroscopy (EDX) were performed with a CamScan CS44. In SEM a high-energy focused electron beam (5 to 50 keV) is thermally emitted in a vacuum of 1E-4 mbar onto a sample. The beam is scanned over the sample and interacts with the surface. Those interaction are detected to extract topographic and material contrast.

A major product of the interactions of electron beam with the sample are secondary electrons ($E < 50$ eV). Atoms in the sample are being ionized and excited such that secondary electrons can diffuse out of the sample to be detected by a scintillator-photomultiplier system. The yield of secondary electrons is strongly dependent on the angle of incidence onto the surface element. This dependence leads to a light-dark contrast when scanning edges and flat areas. Hence, secondary electrons provide

structural information of the sample surface.

Other electrons ($E > 50$ eV) are being backscattered by elastic collisions with the atoms inside the interaction plume. Their number is proportional to the square root of the atomic number \sqrt{Z} . Hence, backscattered electrons provide a material contrast. Since a slight topographic contrast superimposes the material contrast, a segmented semiconductor diode is used to differentiate both signals.

Another signal is X-ray radiation with both its continuous and characteristic parts. Characteristic radiation is emitted when vacancies, that are created in the atomic shells by ionization and excitation via the incident electron beam, are being filled by electrons in energetically higher shells. These level transitions are specific for each element and the characteristic spectrum measured is used to determine the element composition of the sample. In EDX a Lithium-drifted silicon detector is used. At the end, the measured spectrum is compared with individual element spectra to identify the material in the sample. Elements H, O, N and C can not be detected by the system as a polymer foil is used as a window to prevent detector contamination.

4.4 Optical Transmission

Measurements of optical transmission were performed on a UV/VIS double beam spectrometer. Light in the spectral range from 190 nm to 326 nm and from 326 nm to 1100 nm was provided by a deuterium and halogen lamp, respectively. Coming from the source, the light passes a filter wheel that filters any light outside the desired spectral range. The light enters the monochromator through a slit and hits a turnable concave grating that acts as the dispersive element. A beam splitter separates the beam leaving the monochromator through another slit into a reference path without and a measurement path with sample. Two photodiodes detect the two different light beams. The measured quantity is the transmittance t , i.e. the ratio of light intensity I_t that has been transmitted through the sample to the intensity I_0 detected in the reference path. The transmittance is dependent on the absorption coefficient α , the refractive index n and the thickness of the sample d via

$$t = \frac{(1 - R)^2 e^{-\alpha d}}{1 - R^2 e^{-2\alpha d}} \quad (4.4)$$

where the reflection coefficient R is given by

$$R = \frac{(n - 1)^2}{(n + 1)^2}. \quad (4.5)$$

For $R \ll 1$ the denominator in 4.4 can be replaced by 1 so that we yield the more simple expression

$$t = t_0 e^{-\alpha d}, \quad (4.6)$$

i.e. the Lambert-Beer law where t_0 is equivalent to the transmittance measured in the reference path. With the help of the Lambert-Beer law one can deduce the absorption coefficient as long as the thickness d is known. From transmission data of thin plane-parallel samples the thickness can be determined via oscillations caused by interference. The thickness is then given by

$$d = \frac{m}{2n} \cdot \frac{1}{\nu_1 - \nu_2} \quad (4.7)$$

where m is the number of maxima in the spectral range from wave numbers ν_1 to ν_2 . The knowledge of the wavelength dependence of the absorption coefficient allows for a determination of the bandgap. In a α^2 vs. E plot or in a $\sqrt{\alpha}$ vs. E plot for direct and indirect semiconductors, respectively, an extrapolation of an absorption peak at the low energy side to $\alpha = 0$ gives an estimate of the bandgap.

4.5 Hall Effect and Resistivity Measurements

If a current and a magnetic field, both perpendicular to each other, are applied to a conductor, a voltage perpendicular to both the applied current and field is observed. This Hall voltage U_H can be explained as follows.

A current density, positive for holes and electrons, is caused by an applied electric field. Once a magnetic field is turned on, charge carriers are deflected via the Lorentz force building up an electric field E_H . When equilibrium is reached, we can write

$$eE_H = F_L = ev_x B_z \quad (4.8)$$

Electron and hole velocities have opposite signs, hence the sign of the Hall field determines the type of charge carrier. For this reason, measurements of the Hall effect has become significant in the study of semiconductor materials. Another important

quantity derived from Hall measurements is the Hall coefficient R_H that also changes sign with carrier type:

$$E_H = v_x B_z = \frac{j_x B_z}{qn} = R_H j_x B_z \quad (4.9)$$

As one can see, the charge carrier concentration can be extracted from the Hall coefficients. Furthermore resistivity data and Hall mobilities are obtained via

$$\vec{j} = \frac{\vec{E}}{\hat{\rho}} \quad (4.10)$$

and

$$\mu_H = \frac{|R_H|}{\hat{\rho}} \quad (4.11)$$

The thin films studied in this work are not of ideal isotropic cuboidal shape but vary in thickness and size. We eliminate an influence of sample geometry on measurement results by employing the *van der Pauw* method. For this method, samples are required to be smooth and plan-parallel. Four gold contacts whose contact area is small compared to the sample area are placed on the edges of the sample (cf. Fig. 5.4(a)). In terms of sample geometry the only input parameter is the sample thickness d and the resistivity is determined as follows.

A current I_{AB} is applied between contacts A and B . Opposite, at contacts C and D the voltage drop U_{CD} is measured to obtain the resistance $R_{AB,CD}$ via

$$R_{AB,CD} = \frac{U_{CD}}{I_{AB}} \quad (4.12)$$

Next, we apply current and measure voltage rotated by 90° , i.e. I_{BC} and U_{DA} , such that

$$R_{BC,DA} = \frac{U_{DA}}{I_{BC}} \quad (4.13)$$

The resistivity ρ_1 is then calculated by [93]

$$\rho_1 = \frac{\pi d}{\ln 2} \frac{R_{AB,CD} + R_{BC,DA}}{2} f \quad (4.14)$$

where f is a correction function. Another resistivity ρ_2 is obtained by repeating above two steps by rotating and measuring twice more by 90° , i.e. applying currents I_{CD} and I_{DA} . Resistivities ρ_3 and ρ_4 are measured by applying the respective currents with opposite sign. Finally, the measured resistivity ρ is then the mean of all four individual resistivities.

The Hall coefficient is determined by two measurements with and without applied magnetic field and is given by [93]

$$R_H = \frac{d}{B_z} \cdot \Delta R_{AC,BD} \quad (4.15)$$

with $\Delta R_{AC,BD} = R_{AC,BD}(B_z = 0) - R_{AC,BD}(B_z \neq 0)$. Similarly to the resistivity, four measurements are taken and the average is calculated. From the four measurements of ρ and R_H , four values of charge carrier concentration n and Hall mobility μ_H are calculated; again, of these four values the mean is taken.

For the samples investigated in this work, individual Hall coefficients were inconsistent changing sign. Also, charge carrier concentrations often varied by an order of magnitude. This is possibly due to small mobilities below the instrument's sensitivity. Consequently, only resistivity data has been of use.

5 Thin Film Deposition

5.1 Pulsed Laser Deposition (PLD)

All thin films were deposited by pulsed laser deposition (PLD) on various oxide single crystalline substrates. A detailed description of this deposition method can be found in [94].

For PLD, the material to be deposited was prepared as a pelletized polycrystalline target by means of a solid state synthesis according to [4]. Target preparation was done by Gabriele Ramm of the Semiconductor Physics Group. Oxide powders Na_2CO_3 (5N purity, Alfa Aesar) and IrO_2 (85.45% Ir content, ChemPUR) were homogenized in a zirconia ball mill in a ratio of 1.05:1 - a 5 % excess of sodium carbonate was added to account for Na loss during synthesis. The mixture was then calcined in a closed alumina crucible for 24 h at 750°C in air. Afterwards, it was reground and pressed to obtain a cylindrical one-inch diameter target that in turn was sintered for 48 h at 900°C . Higher sintering temperatures were not possible, since IrO_2 tends to sublime above $1,000^\circ\text{C}$. An XRD $2\Theta - \omega$ -scan of the final target (Fig. 5.1) was compared with the JCPDS diffraction database pattern 00-026-1376 for Na_2IrO_3 . The XRD pattern shows a continuous shift with respect to the database pattern. Most likely, the shift arises from a misalignment of the target surface and the focusing circle. Again, this misalignment is likely to occur, since no proper sample holder is available for samples as thick as the used target. Despite the shift, there is a good agreement between the measured pattern and the database pattern, which confirms the dominating Na_2IrO_3 phase of the target.

In PLD, the deposition takes place in a vacuum chamber (S- and E-chamber). A schematic is shown in figure 5.3(a). The chamber is evacuated and oxygen with partial pressures varying from 0.6 mbar to $1\text{E-}4$ mbar is injected into the chamber. The substrate is heated. Its temperature cannot be directly determined, however, a heater power of 400 W corresponds to approximately 620° (cf. 5.3(b)). An excimer-laser (Coherent Lambda Physik LPX305, KrF, $\lambda_0 = 248\text{ nm}$) enters the chamber through a quartz window and ablates the rotating target with short high-intensity pulses, s.t. the absorption and dissipation of laser energy is confined to the immediate area hit by the laser. Since the laser energy is sufficiently high, the ablated material consists of vaporized elemental, ionized and excited species as well as clustered target constituents.

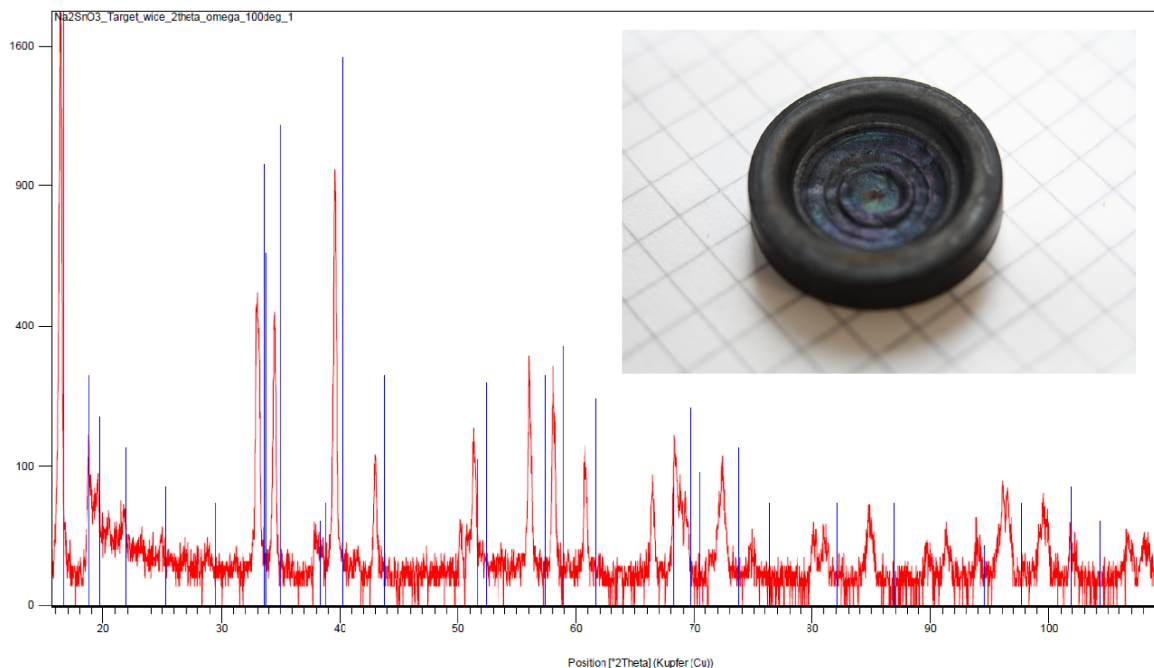


Figure 5.1 XRD $2\theta - \omega$ -scan of the polycrystalline Na_2IrO_3 target (red) and JCPDS diffraction database pattern 00-026-1376 for Na_2IrO_3 (blue). The inset shows a photograph of the Na_2IrO_3 target.

The ejecta constitute a plasma plume that propagates normal to the target surface and towards the substrate holder. Figures 5.2(a) and (b) show an optical emission (OES) spectrum and a photograph of the Na_2IrO_3 plasma plume, respectively. The plume is clearly dominated by the yellow Na emission lines D1 and D2. When the plasma plume hits the substrate, it condenses onto the substrate and a film grows. To ensure a homogeneous film growth and thickness, the substrate is being rotated. Usually in this work, the laser energy per pulse is set to 600 mJ with a pulse duration of about 25 ns.

The used substrate holder allowed for the mounting of 5 x 5 and 10 x 10 mm² substrates. Substrates were held in place by masks with either circular or rectangular opening (cf. Fig. 5.4). Prior to deposition, the chamber and substrate were usually heated up at 400 W for 60 minutes. At first, 300 laser pulses with a frequency of 1 Hz were applied to the target, to create a nucleation layer on the substrate for further film growth. Subsequently, pulse frequency was increased to 15 Hz and in most cases the target was ablated by a further 30,000 pulses. A variation of the number of pulses was done for some samples to investigate the influence of film thickness on measured properties. A first ellipsometry measurement could not quantify the film thickness at 30,000 pulses satisfactorily - partly due to the high surface roughness. However, a rough estimate of film thickness at 30,000 pulses is between 400 nm and 800 nm. After deposition the

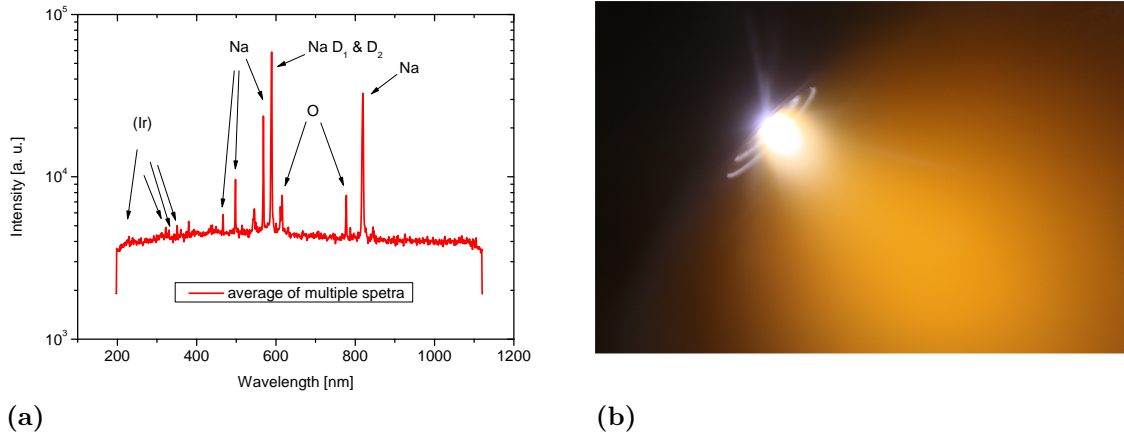


Figure 5.2 (a) Optical emission spectrum of the center of the plasma plume. (b) Photograph of the yellow plasma plume during ablation of the Na_2IrO_3 target

sample was annealed *in-situ* for 5 minutes at an oxygen partial pressure of 800 mbar, while the heater power remained unchanged.

In the course of this work, process parameters such as oxygen partial pressure, growth temperature (heater power) and number of pulses but also the substrate were varied to find the optimal growth conditions of Na_2IrO_3 thin film in terms of crystallinity and surface roughness. The substrates used were: a-plane (11.0) sapphire, YAlO_3 (YAO) (001), c-plane (00.1) sapphire and c-plane ZnO (00.-1). For all substrates used, table 5.1 lists the in-plane (a , b) and out-of-plane (c) unit cell dimensions. Also listed are the lattice parameters of the Na_2IrO_3 C2/ c unit cell, as well as the parameters a and c of the hexagonal Ir-honeycomb lattice in Na_2IrO_3 with respect to the C2/ m unit cell [67]. The lattice mismatch between film and substrate is calculated by a simple comparison of the corresponding lattice constants of film and substrate. The lattice mismatch calculated in this way is generally large for all substrates. It suggests that Na_2IrO_3 thin films will adopt a relaxed rather than a pseudomorphic growth mode. However, proper insight into the in-plane epitaxial relationship between film and substrate is obtained via XRD measurements (cf. Sec. 6.1.1).

5.2 Sputter Deposition of Gold Contacts

In order to enable measurements such as magnetoresistance, Hall resistivity and optical conductivity, DC sputtering of gold contacts was employed for most of the samples. Samples were placed in a vacuum chamber at a process pressure of 0.023 mbar and an

argon gas flow of 100 sccm. The gold layers were deposited for 80 s at a power of 60 W. The position and shape of the contacts was determined by shadow masks to either obtain a van-der-Pauw or Hall-bar geometry of contacts (cf. Fig. 5.4).

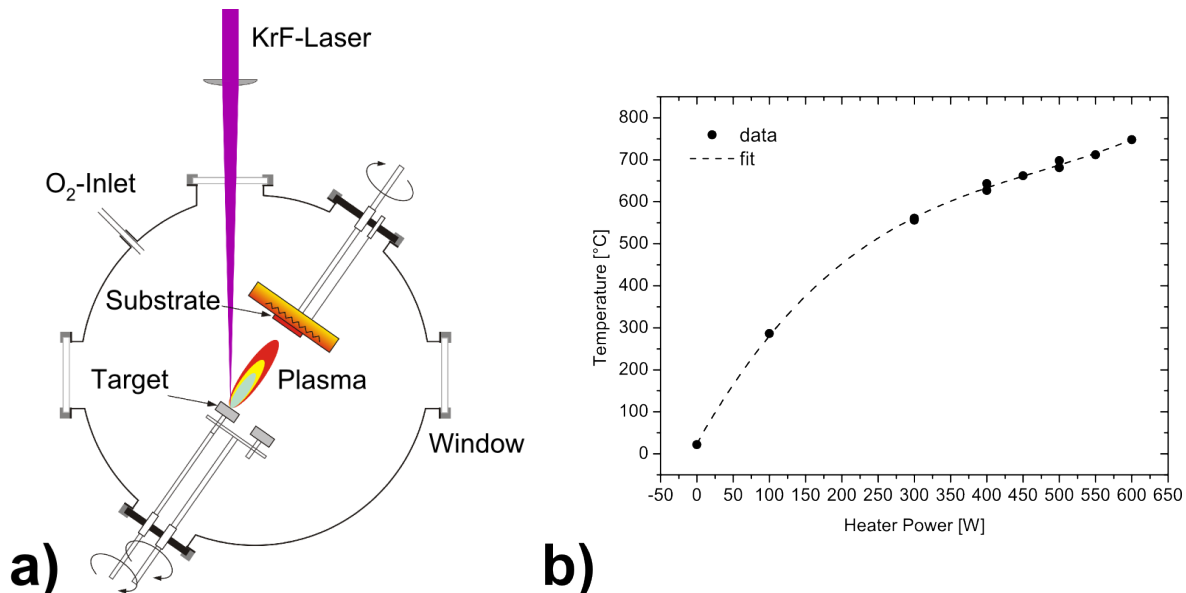


Figure 5.3 Pulsed Laser Deposition. (a) Schematic view of a PLD setup (taken from M. Lange, HLP). (b) Substrate holder temperature versus heater power. The dashed line is a fit as guide to the eye.

Table 5.1 Structural parameters of the substrates used for Na₂IrO₃ thin films. Lattice constants are taken from JCPDS diffraction database patterns contained in the *PCPDFWIN v. 2.00* software. For the hexagonal substrates, the mismatch is calculated with respect to the hexagonal Ir-honeycomb lattice in Na₂IrO₃.

substrate	in-plane unit cell type	in-plane [\AA]		out-of-plane [\AA] c	mismatch [%]	
		a	b		a	b
a-sapphire	rectangular	8.244	12.990	4.755	34.28	27.68
YAO(001)	rectangular	5.319	7.380	5.180	1.86	27.29
c-sapphire	hexagonal	4.755	-	12.991	35.42	-
c-ZnO	hexagonal	3.250	-	5.207	5.51	-
Na ₂ IrO ₃ (C2/c)	rectangular	5.418	9.394	10.765		
Na ₂ IrO ₃ (C2/m) [67]	hex. (Ir-Ir)	3.071	-	5.536		

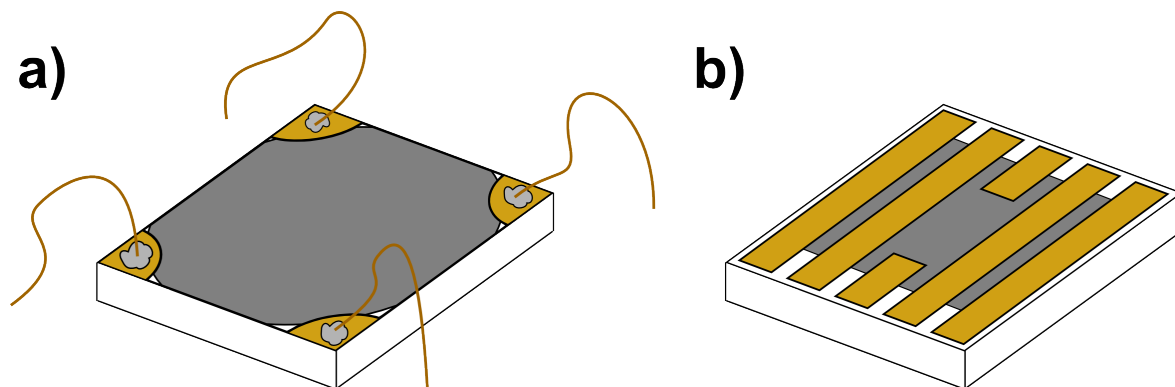


Figure 5.4 Sample layout of Na_2IrO_3 thin films. (a) Van-der-Pauw geometry: after film deposition via PLD, four gold contacts are sputtered onto the sample in a van-der-Pauw geometry; gold wires are affixed with silver paste. (b) Hall-bar geometry: a rectangular shaped film is contacted with six gold strips.

5.3 PECVD of SiN_x as Passivation and Protective Layer

To prevent sample corrosion due to the reactive sodium, some samples were covered with a SiN_x layer by means of plasma enhanced chemical vapour deposition (PECVD). For resistivity measurements the protective layer was applied after application of gold contacts and wires.

PECVD is a chemical deposition method where the chemical layer forming process is controlled by a RF plasma. For deposition, process gases (here silane SiH_4 and ammonia NH_3) are directed into a vacuum chamber. The sample is placed between two electrodes between which a high frequency field is applied. This RF field leads to the formation of a plasma above the sample. In this way, radicals and ions are formed that react on the sample surface to the SiN_x layer. The instrument used was a Oxford Instrument's Plasmalab 80 Plus. The RF frequency was at a fixed 13.56 MHz at a power density of $100\text{mW}/\text{cm}^2$. Mass flow of process gases was set to 28 sccm and 1000 sccm for NH_3 and SiH_4 (2% SiH_4 in N_2), respectively. Total chamber pressure was 1 Torr and substrate temperature 80°C . The resultant SiN_x is about 110 nm thick.

6 Results and Discussion

6.1 Growth of Na_2IrO_3

By means of PLD, the growth of Na_2IrO_3 thin films was done at a total of four different single crystalline substrates: a-plane (11.0) sapphire, YAlO_3 (YAO) (001), c-plane (00.1) sapphire and c-plane ZnO (00.-1). Film growth on a-sapphire and YAO(001) underwent a more extensive study at which PLD deposition parameters such as oxygen partial pressure and heater power were varied systematically (pressure and temperature series). The discussion in the following subsections will always start with films on these two substrate materials. Individual samples were also grown on c-sapphire and c-plane ZnO to compare with the former two substrates in light of substrate-induced effects on film properties. After deposition, the thin films were studied in terms of their surface morphology and crystal structure as well as in respect of their electrical, optical and magnetic properties.

6.1.1 Structural Analysis - XRD

The structural analysis of the PLD-grown thin films begins with wide-angle 2Θ - ω XRD measurements for the purpose of investigating the main growth mode and the occurrence of possible other phases.

a-sapphire Figure 6.1 shows the XRD patterns of the pressure series of Na_2IrO_3 thin films on a-sapphire at a heater power of 400 W and oxygen partial pressures ranging from 0.1 mbar to 3×10^{-4} mbar. Apart from the expected substrate reflections $\text{Al}_2\text{O}_3(110)$ and $\text{Al}_2\text{O}_3(220)$, further reflections can be seen. They were indexed according to the JCPDS diffraction database pattern 00-026-1376 for Na_2IrO_3 (C2/c unit cell, Sec. A.2). For all pressures, around $2\Theta=17^\circ$ a reflection can be observed. At 0.1 mbar, this reflection has its maximum at 16.675° and can be indexed reasonably well to the (002) reflex of Na_2IrO_3 at 16.682° . There is however a second peak with about half the intensity of the first located at 17.250° that cannot be indexed to any reflex in the database pattern of Na_2IrO_3 . Instead, the database pattern 00-026-1377 for $\text{Na}_4\text{Ir}_3\text{O}_8$ (cubic, Sec. A.2) lists the (111) reflex at 17.070° . Hence, at 0.1 mbar it

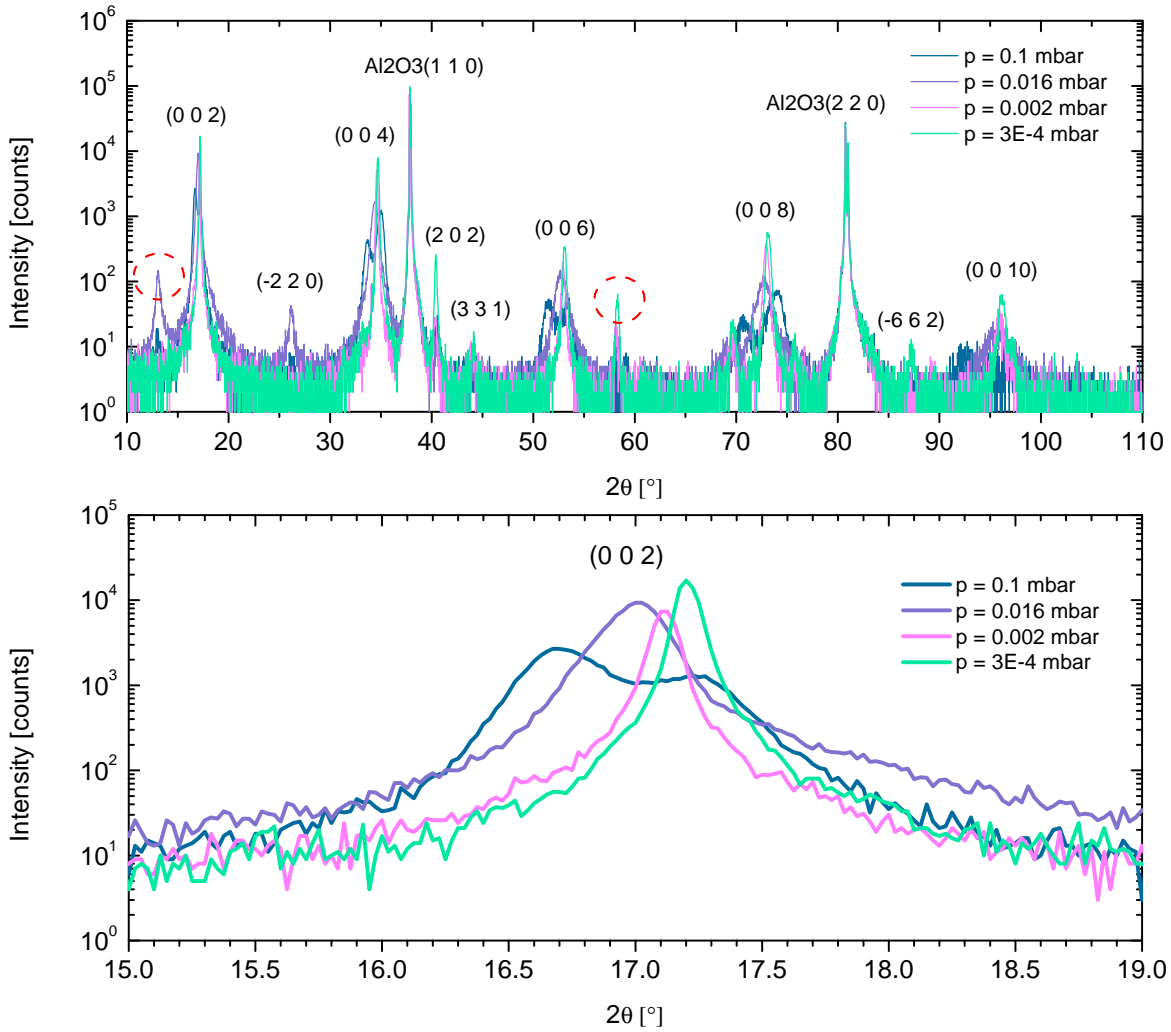


Figure 6.1 XRD 2θ - ω -scans of (001) oriented Na_2IrO_3 thin films on a-sapphire grown at 400 W heater power and oxygen partial pressures as indicated. Red dashed circles denote other crystalline phases, such as $\text{Na}_4\text{Ir}_3\text{O}_8$. Top: Full pattern ($10^\circ < 2\theta < 110^\circ$). Bottom: Zoom-in on (002) reflection of Na_2IrO_3 indicating tunability of lattice constant with oxygen partial pressure.

is very much possible, that there is a coexistence of two phases: a Na_2IrO_3 phase with (001) orientation and a $\text{Na}_4\text{Ir}_3\text{O}_8$ phase with (111) orientation.

From the (002) reflexes onward, further reflections appear at an approximate periodicity of $2\theta \approx 17^\circ$ with decreasing intensity. They in turn can be indexed to higher orders of the (001) orientation of Na_2IrO_3 , that is (004), (006), (008) and (0010). Other reflections in the pattern can be related to other orientations of Na_2IrO_3 (see figure). However, there remain reflections that cannot be identified on the basis of a Na_2IrO_3 -phase (red circles in figure 6.1. For instance, the reflection at 58.325° can be indexed to the (440) orientation of the closely related $\text{Na}_4\text{Ir}_3\text{O}_8$ phase.

In the bottom part of figure 6.1, one can clearly see how the peak position of the

(002) reflection shifts to higher angles with increasing oxygen partial pressure, which is equivalent to a decrease of the c -lattice constant. Table 6.1 illustrates this tunability of the out-of-plane lattice parameter c with pressure. The calculation of c was done according to equation 4.2 and the $C2/c$ and $C2/m$ [66] unit cells. The decrease of c with increasing pressure is 0.338 \AA ($C2/c$). Similarly, also the FWHM of the (002) reflections decreases with pressure suggesting an improvement of film crystallinity with pressure. The peak intensities tend to increase with pressure as well.

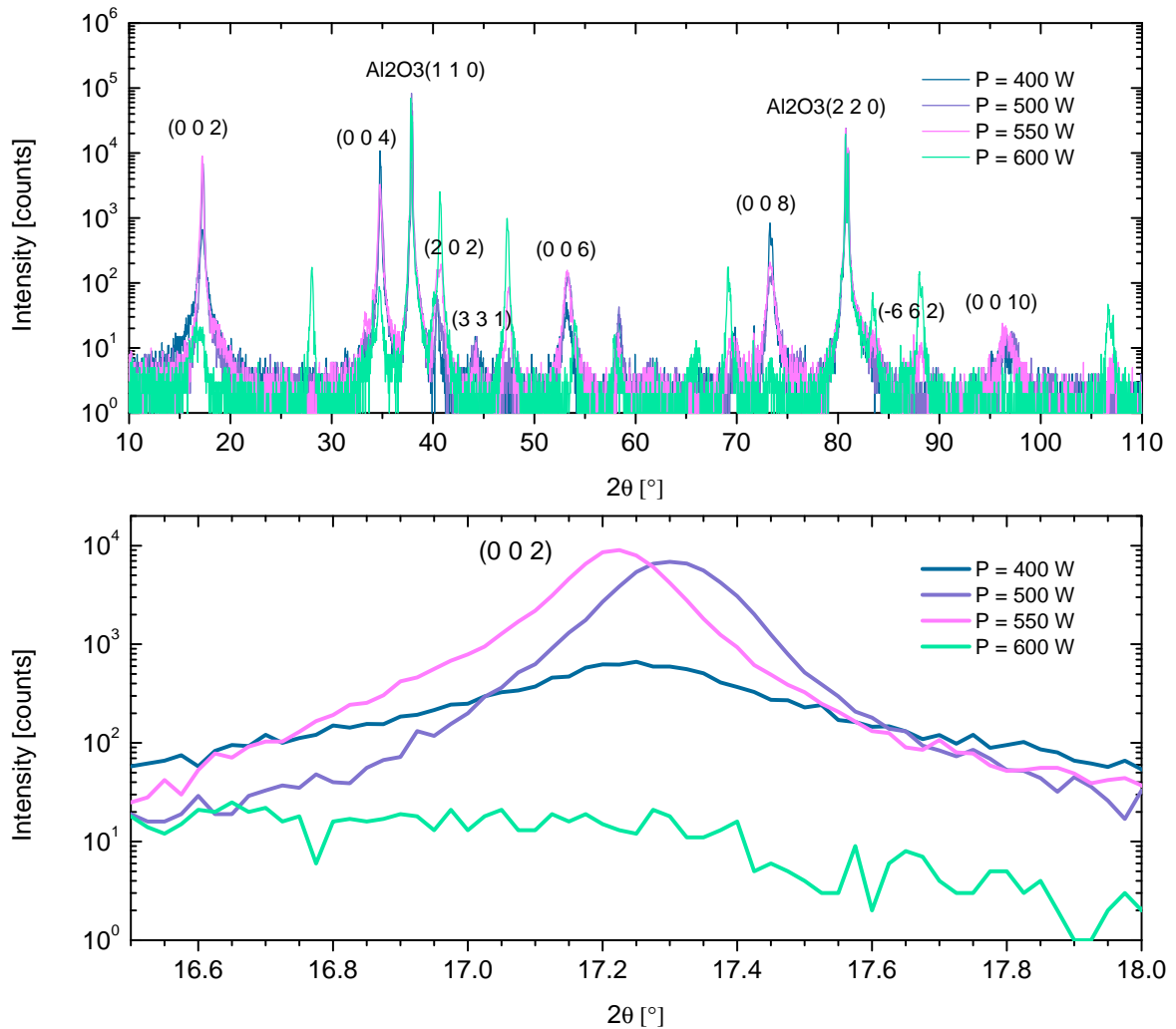


Figure 6.2 XRD 2θ - ω -scans of (001) oriented Na_2IrO_3 thin films on α -sapphire grown at an oxygen partial pressures of 3×10^{-4} mbar and heater powers as indicated. Top: Full pattern ($10^\circ < 2\theta < 110^\circ$). Bottom: Zoom-in on (002) reflection of Na_2IrO_3 .

Motivated by the low surface roughness of the Na_2IrO_3 thin film grown at 3×10^{-4} mbar and 400 W (cf. sec. 6.1.2), a temperature series was done at 3×10^{-4} mbar with applied heater powers ranging from 400 W to 600 W. Figure 6.2 clearly shows, how the (001) orientation of Na_2IrO_3 could be reproduced and was preserved for temperatures

below 700°C (550 W). In fact, at 600 W (700°C–713°C) the (001) phase is hardly discernible. Instead several reflections belonging to other crystalline phases, such as metallic Ir- and IrO-species, dominate. The temperature dependent resistivity at 600 W is indeed metallic (cf. Sec. 6.2) confirming the presence of such metallic species in the thin film. Considering the boiling point of sodium of 883°C, it is feasible that at the very low pressure of 3×10^{-4} mbar and at 700°C considerable amounts of sodium evaporated from the film leaving behind metallic clusters of Ir-containing species. An EDX analysis of the respective sample confirmed this (Fig. 6.3). However, noticeable loss of sodium likely occurs also at 500 W and 550 W since similar crystalline phases, albeit with lower intensity, can be observed. While the c-lattice constant does not vary uniformly (cf. Tab. 6.1), the peak height increases with temperature inside the regime investigated.

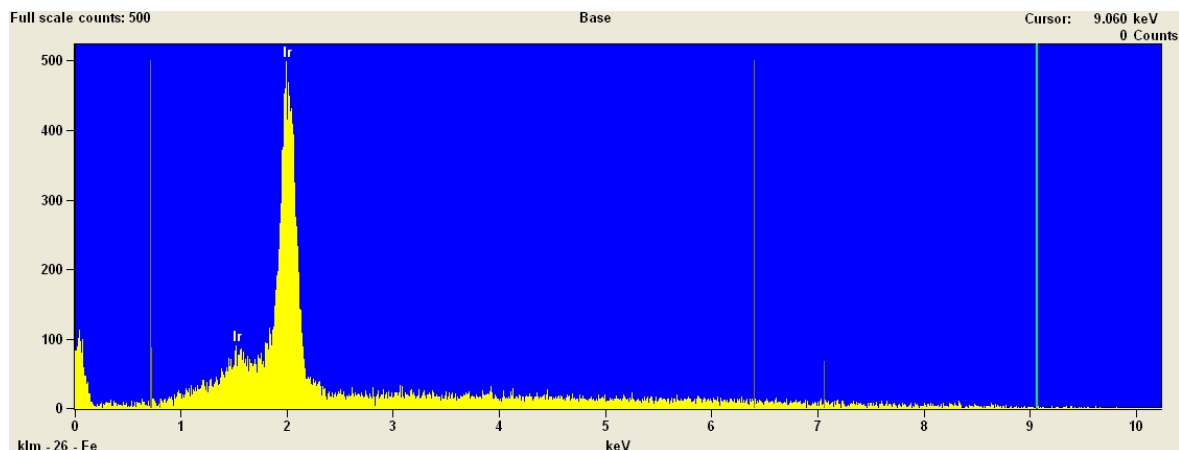


Figure 6.3 EDX analysis of a Na_2IrO_3 thin film grown on a-sapphire at an oxygen partial pressure of 3×10^{-4} mbar and 600 W. The sodium content of this sample was greatly reduced.

To investigate the epitaxial relationship of the film to the substrate, XRD ϕ -scans of the asymmetric $\text{Al}_2\text{O}_3(113)$ and $\text{Na}_2\text{IrO}_3(202)$ reflections were performed on sample S1557 grown at 0.3 mbar and 400 W (Fig. 6.4(a)). The asymmetric (202) reflection of Na_2IrO_3 is six-fold and two of the six peaks very well coincide with the two measured peaks of the asymmetric $\text{Al}_2\text{O}_3(113)$ reflection. The result indicates the six-fold in-plane symmetry of the hexagonal layers containing the Ir atoms in Na_2IrO_3 and making up the honeycomb structure. Furthermore, very weak reflections shifted by 30° can be seen between the six-fold (202) reflections. They could be regarded as an indication of film crystallites twisted in-plane by 30° , i.e. 30° rotation domains.

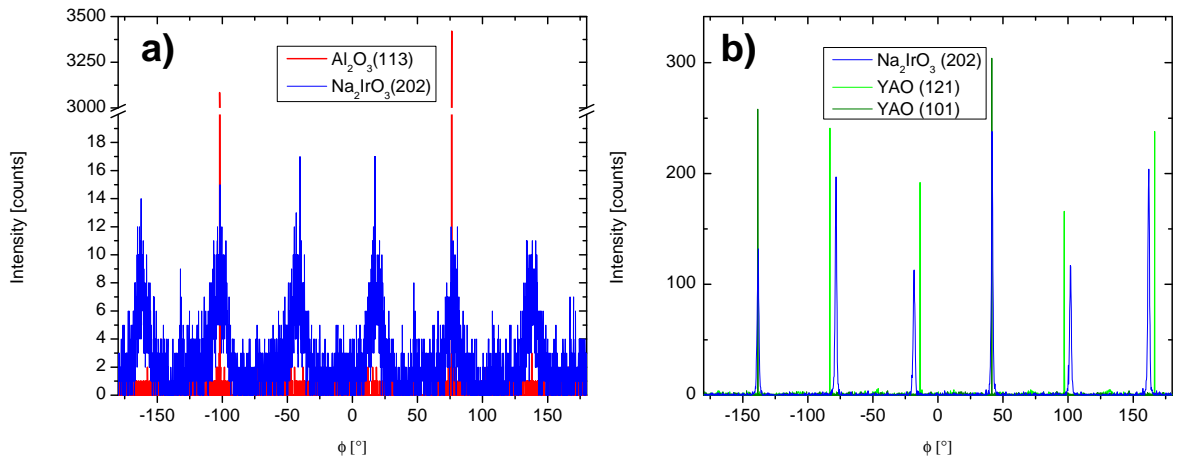


Figure 6.4 XRD ϕ -scans of (001) oriented Na_2IrO_3 thin films grown (a) on a-sapphire at 0.3 mbar and 400 W (S1557) and (b) on YAO(001) at 3×10^{-4} mbar and 500 W (E3354). Both ϕ -scans indicate the six-fold in-plane symmetry according to the hexagonal honeycomb structure of Na_2IrO_3 .

YAO(001) Films were also grown on YAO(001) under the exact same conditions as the films on a-sapphire. Figure 6.5 depicts the wide-angle XRD pattern obtained from a pressure series at 400 W. Also on YAO(001) the (001) orientation of Na_2IrO_3 is realized and with pressure a decrease of the c lattice parameter by 0.378 \AA occurs (see. Tab. 6.1). The number of reflections related to other orientations of Na_2IrO_3 or other crystalline phases is greatly reduced. However, on YAO(001) the (004) film reflex is close to the (001) substrate reflex. Above 0.016 mbar the (004) film reflections converges with the (001) substrate reflex. The same can be observed for the (008) film reflections with respect to the (002) substrate reflex. Just as the film grown on a-sapphire at 0.1 mbar, the (002) reflex is followed by another at 17.200° which again indicates the presence of another closely related crystalline phase, i.e. (111) oriented $\text{Na}_4\text{Ir}_3\text{O}_8$.

The temperature series on YAO(001) also has very similar features as the series on a-sapphire: The dominant orientation of the Na_2IrO_3 phase is (001). Peak heights decrease with temperature while the lattice parameter shows no uniform variation. A noticeable difference to a-sapphire is that at 600 W a phase of $\text{Na}_2\text{IrO}_3(001)$ is still preserved and the film is insulating (cf. Sec. 6.2). Still, one finds other crystalline phases relatable to metallic Ir/IrO-species.

Also for a film on YAO(001), XRD ϕ -scans of the YAO(121), YAO(101) and the (202) reflection of Na_2IrO_3 were performed (sample E3354 grown at 3×10^{-4} mbar and 500 W, Fig. 6.4(b)). The asymmetric (202) reflection of Na_2IrO_3 is again six-fold with a 60° periodicity and two of these six peaks very well coincide with the two measured

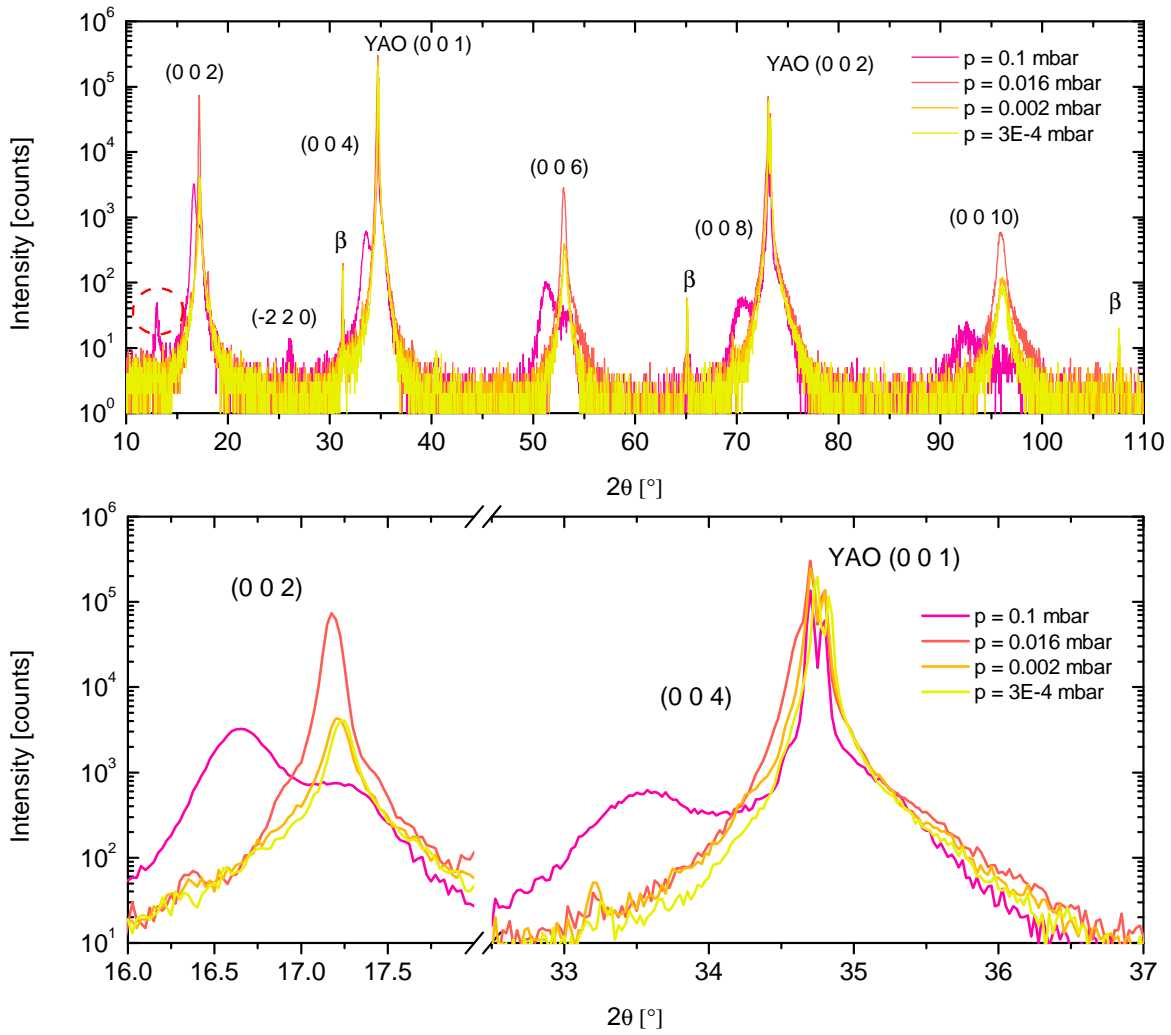


Figure 6.5 XRD 2θ - ω -scans of (001) oriented Na_2IrO_3 thin films on YAO(001) grown at 400 W heater power and oxygen partial pressures as indicated. The red dashed circle denotes another crystalline phase, e.g. $\text{Na}_4\text{Ir}_3\text{O}_8$; β denotes the $K\beta$ spectral lines. Top: Full pattern ($10^\circ < 2\theta < 110^\circ$). Bottom: Zoom-in on (002) and (004) reflections of Na_2IrO_3 indicating tunability of lattice constant with growth temperature.

peaks of the asymmetric $\text{Al}_2\text{O}_3(113)$ reflection at -138° and 42° , respectively. The asymmetric YAO(121) reflection is four-fold with spacings of 70° and 110° indicating the rectangular unit cell dimensions of YAO(001) (see. table 5.1). Four peaks of $\text{Na}_2\text{IrO}_3(202)$ are as close as 5° to the YAO(121) reflexes. In conclusion, the results again clearly indicate the six-fold in-plane symmetry of the hexagonal layers contained in the honeycomb structure of Na_2IrO_3 .

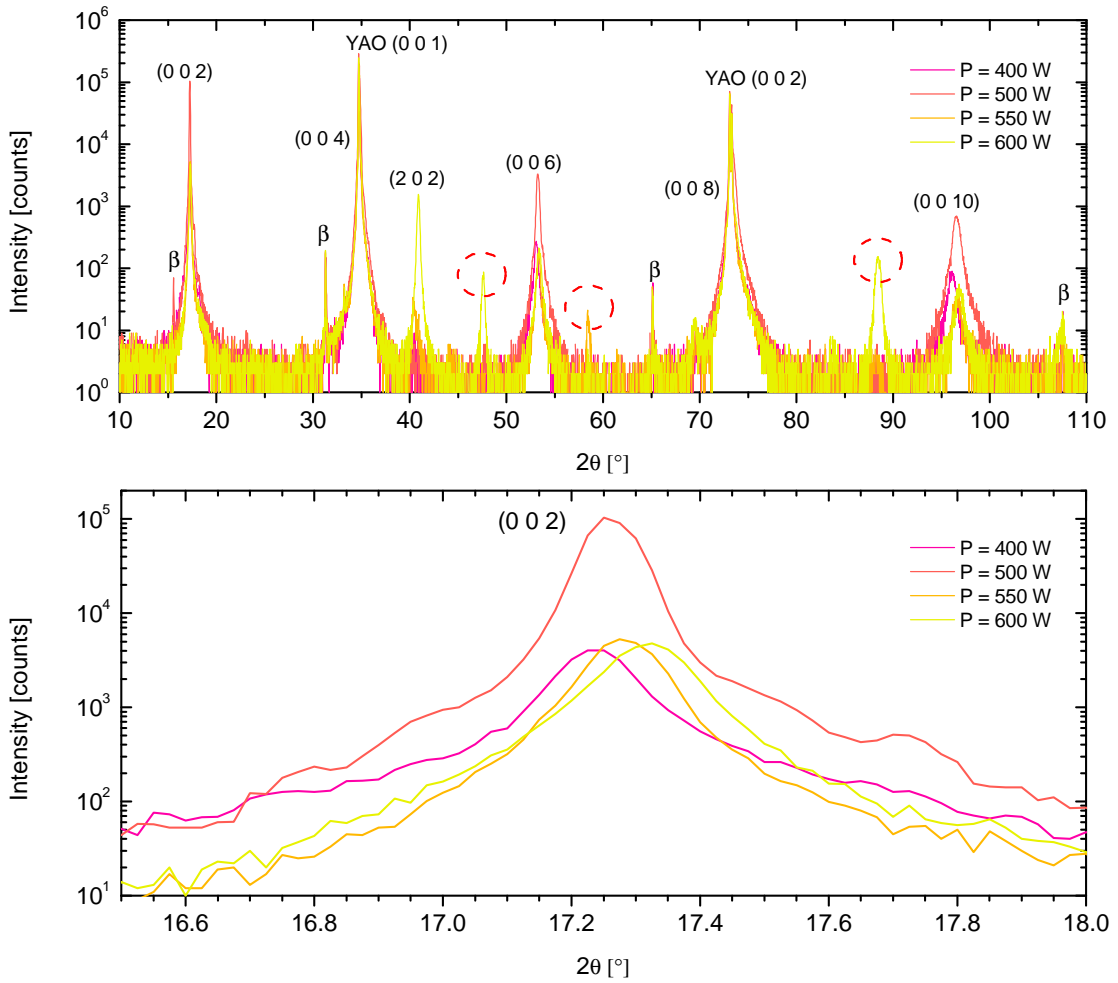


Figure 6.6 XRD 2θ - ω -scans of (001) oriented Na_2IrO_3 thin films on YAO(001) grown at an oxygen partial pressure of 3×10^{-4} mbar and heater powers as indicated. Red circles indicate orientations of a related phase of $\text{Na}_4\text{Ir}_3\text{O}_8$; β denotes the $\text{K}\beta$ spectral lines. Top: Full pattern ($10^\circ < 2\theta < 110^\circ$). Bottom: Zoom-in on (002) reflection of Na_2IrO_3 .

c-sapphire & c-ZnO To further study substrate-induced effects on film growth properties, thin films were also grown on c-sapphire and c-ZnO, both at 400 W and 0.016 mbar. Figure 6.7 displays the results of wide-angle XRD measurements of the respective samples. Again, on both substrates the (001) orientation of Na_2IrO_3 is obtained. There is very little indication for other orientations of Na_2IrO_3 or other crystalline phases. In the bottom part of figure 6.7 a zoom-in of the (002) reflex is shown. The XRD data for films on a-sapphire and YAO(001) are shown, as well. Under the same growth conditions, the film on YAO(001) yields the highest intensity and lowest FWHM. The positions of peak maxima are distributed between 17.02° and 17.25° , i.e. there exists a substrate-induced variation of the c lattice constant (cf. Tab. 6.1)

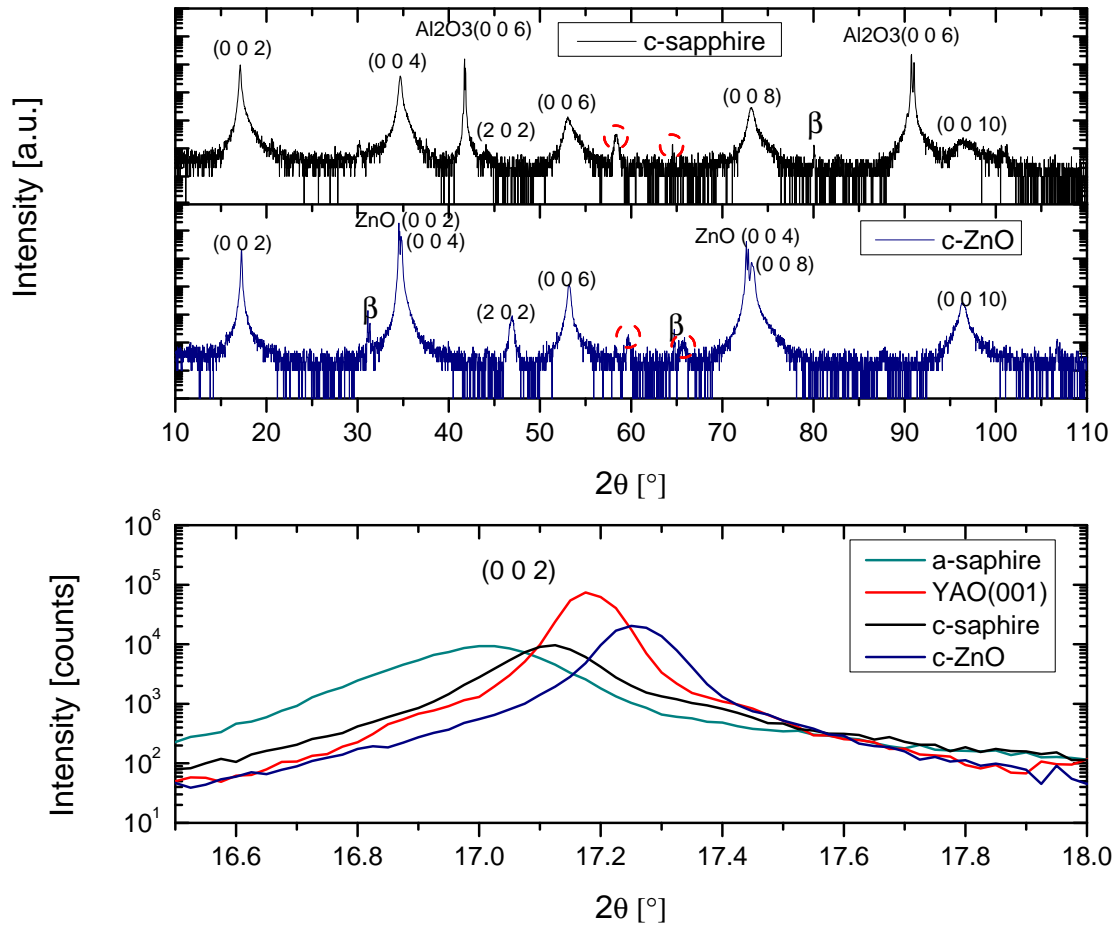


Figure 6.7 Na_2IrO_3 thin films on different substrates. Top: XRD 2θ - ω -scans of (001) oriented Na_2IrO_3 thin films grown on c-sapphire and c-ZnO, both at 400 W and 0.016 mbar. Red dashed circles indicate extrinsic phases. Bottom: Zoom-in on the (002) reflection of $\text{Na}_2\text{IrO}_3(001)$ films grown on substrates as indicated and under growth conditions as in (a).

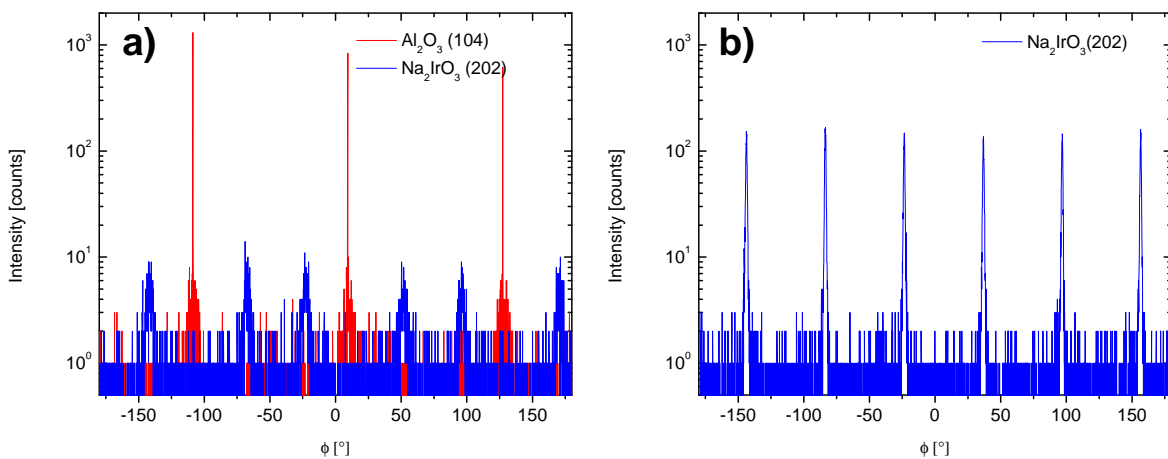


Figure 6.8 XRD ϕ -scans of (001) oriented Na_2IrO_3 thin films grown at 0.016 mbar and 400 W on (a) c-sapphire and (b) c-ZnO. The ϕ -scans indicate the six-fold in-plane symmetry according to the hexagonal honeycomb structure. The spacing of the (202) reflections in (a) is unequal, suggesting a distorted honeycomb structure. In (b), the ϕ -scan of an asymmetrical ZnO reflection is missing.

Table 6.1 Structural properties of Na₂IrO₃ thin films determined by XRD. Listed are the results of pressure and temperature series on a-sapphire and YAO(001), resp. and of a substrate series. Lattice constants w.r.t. the C/2c unit cell c were determined from the (002) peak positions; c_{mean} is the mean of all visible peaks of the (001) phase. Calculation of lattice constants was done similarly also w.r.t. the C2/m unit cell [66].

a-sapphire pressure series (400 W):					C2/c		C2/m	
Sample no.	Pressure [mbar]	Pos. (002) [$^{\circ}2\Theta$]	FWHM [$^{\circ}2\Theta$]	d [\AA]	c_{002} [\AA]	$c_{002,\text{mean}}$ [\AA]	c_{001} [\AA]	$c_{001,\text{mean}}$ [\AA]
E3298	0.1	16.6609	0.246	5.32112	10.793	10.81575	5.629	5.6409
E3300	0.016	17.0227	0.1968	5.20884	10.565	10.565	5.5102	5.51025
E3312	0.002	17.118	0.0984	5.18006	10.507	10.5248	5.4798	5.48912
E3304	3.00E-004	17.2027	0.0984	5.15474	10.455	10.492	5.453	5.4721
a-sapphire temperature series (3×10^{-4} mbar):					C2/c		C2/m	
Sample no.	Heater Power [W]	Pos. (002) [$^{\circ}2\Theta$]	FWHM [$^{\circ}2\Theta$]	d [\AA]	c_{002} [\AA]	$c_{002,\text{mean}}$ [\AA]	c_{001} [\AA]	$c_{001,\text{mean}}$ [\AA]
E3315	400	17.22	0.123	5.14962	10.445	10.46525	5.4476	5.458275
E3316	500	17.2986	0.1722	5.12638	10.398	10.4455	5.423	5.7236
E3318	550	17.222	0.1476	5.14903	10.444	10.4694	5.4469	5.46032
E3323	600	-	-	-	-	-	-	-
YAO(001) pressure series (400 W):					C2/c		C2/m	
Sample no.	Pressure [mbar]	Pos. (002) [$^{\circ}2\Theta$]	FWHM [$^{\circ}2\Theta$]	d [\AA]	c_{002} [\AA]	$c_{002,\text{mean}}$ [\AA]	c_{001} [\AA]	$c_{001,\text{mean}}$ [\AA]
E3337	0.1	16.6294	0.2706	5.33115	10.813	10.82975	5.6396	5.648175
E3342	0.016	17.1818	0.0984	5.16096	10.468	10.5028	5.4596	5.47774
E3345	0.002	17.2136	0.123	5.15151	10.449	10.4902	5.4496	5.47116
E3346	3.00E-004	17.236	0.123	5.14487	10.435	10.4804	5.4425	5.4661
YAO(001) temperature series (3×10^{-4} mbar):					C2/c		C2/m	
Sample no.	Heater Power [W]	Pos. (002) [$^{\circ}2\Theta$]	FWHM [$^{\circ}2\Theta$]	d [\AA]	c_{002} [\AA]	$c_{002,\text{mean}}$ [\AA]	c_{001} [\AA]	$c_{001,\text{mean}}$ [\AA]
E3346	400	17.236	0.123	5.14487	10.435	10.4804	5.4425	5.4661
E3354	500	17.2621	0.0738	5.13714	10.42	10.4702	5.4344	5.46086
E3355	550	17.2824	0.123	5.13117	10.407	10.4568	5.428	5.45384
E3356	600	17.3233	0.123	5.11914	10.383	10.4508	5.4153	5.4506
Substrate series (400 W, 0.016 mbar):					C2/c		C2/m	
Sample no.	Substrate	Pos. (002) [$^{\circ}2\Theta$]	FWHM [$^{\circ}2\Theta$]	d [\AA]	c_{002} [\AA]	$c_{002,\text{mean}}$ [\AA]	c_{001} [\AA]	$c_{001,\text{mean}}$ [\AA]
E3274	c-Sapphire	17.1556	0.123	5.1688	10.484	10.491	5.468	5.471
E3302	a-Sapphire	17.163	0.1476	5.16658	10.479	10.495	5.465	5.474
E3342	YAO (001)	17.1818	0.0984	5.16096	10.468	10.503	5.460	5.478
E3287	c-ZnO	17.2561	0.123	5.1389	10.423	10.466	5.436	5.459

In addition, XRD ϕ -scans were made. In agreement with the hexagonal in-plane symmetry of Na_2IrO_3 , both on c-sapphire and c-ZnO (Figs. 6.8(a) and (b)) the asymmetric $\text{Na}_2\text{IrO}_3(202)$ reflections are six-fold. While for c-ZnO the six reflections have a uniform spacing of 60° , there is an uneven spacing of 75° and 45° for c-sapphire. The unequal spacing suggests a distortion of the Ir-containing hexagonal honeycombs in the film grown on c-sapphire.

In conclusion, the very good in-plane and out of plane orientation of Na_2IrO_3 thin films on all four substrates was shown and therefore thin film growth can be considered as epitaxial. Moreover, the tunability of the c lattice constant by the PLD process parameters growth temperature and oxygen partial pressure was shown. Especially at high temperatures and low oxygen partial pressures, additional minor peaks related to other orientations of Na_2IrO_3 but also to the related crystalline phase of $\text{Na}_4\text{Ir}_3\text{O}_8$ became visible.

6.1.2 Surface Morphology - AFM

For the investigation of the surface morphology of the Na_2IrO_3 thin films an atomic force microscope(cf. Sec. 4.2) was employed. A sample's topography was measured in the non-contact mode first with an area of $10 \times 10 \mu\text{m}^2$. Within this area another measurement with a smaller area of $3 \times 3 \mu\text{m}^2$ was performed to obtain a closer image of crystallites. If possible, the smaller scan areas were chosen to be free of obvious droplets in order to give lower values of RMS roughness that in addition represent the actually achievable surface roughness. However, due to drifts of the cantilever sometimes measurements had to be aborted, such that some topography images are not of the complete area. Therefore, AFM images were cropped to $10 \times 5 \mu\text{m}^2$ and $3 \times 1.5 \mu\text{m}^2$, respectively. From these cropped images the RMS roughness was obtained to have a direct comparison.

Figure 6.9 shows the root mean squared (RMS) roughness in dependence of oxygen partial pressure (a) and temperature (b) of Na_2IrO_3 films grown on both a-sapphire and YAO(001). The surface roughness ranges from 11 to 143 nm. AFM scans within the $3 \times 1.5 \mu\text{m}^2$ generally yield a smaller RMS roughness. All films can be considered as rough. A complete overview over all AFM images can be found in the appendix.

On a-sapphire, a trend towards a smoother surface with decreasing pressure can be seen (Fig. 6.9(a)). At partial pressures of 0.016 and 3×10^{-4} mbar, the difference

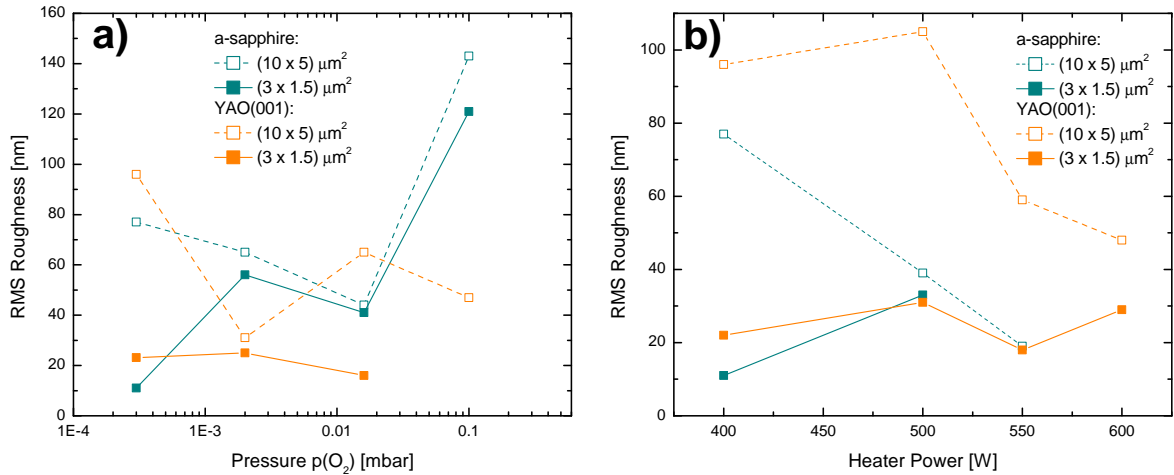


Figure 6.9 Root mean squared (RMS) roughness of Na_2IrO_3 thin films PLD-grown on a-sapphire and YAO(001) in dependence of (a) oxygen partial pressure and (b) heater power.

between surface roughness within $10 \times 5 \mu\text{m}^2$ and $3 \times 1.5 \mu\text{m}^2$ is largest. This is due to droplets adsorbed on the surface; for an example see Figure 6.10. Simultaneously, the size of crystallites decreases (Fig. A.1). In the temperature series ((Fig. 6.9(b)) at 3×10^{-4} mbar, the surface roughness within $10 \times 10 \mu\text{m}^2$ continuously decreases down to 21 nm at 550 W. At 500 W, large plate-like crystallites can be seen (Fig. A.2(c)) in compliance with the larger intensity in the wide-angle XRD scan when compared to 400 W (cf. Fig. 6.2). There is no AFM data at 600 W, because in that case the film showed no dominant Na_2IrO_3 phase and was in fact metallic (cf. Sec. 6.2).

For films grown on YAO(001) there is no clear dependence of surface roughness on pressure. Yet, the smaller scan areas are generally smoother than the larger ones indicating the presence of droplets - especially at 0.016 mbar and 3×10^{-4} mbar (cf. Figs. A.3). At the lowest pressure, the surface roughness on YAO(001) is comparable with that on a-sapphire. With temperature, the surface roughness tends to decrease in the $10 \times 10 \mu\text{m}^2$ scans, although it is maximal at 500 W in compliance with some very large droplets (Fig A.4(c)).

A direct comparison between the four different substrates a-sapphire, YAO(001), c-sapphire and c-ZnO at 400 W and 0.016 mbar is shown in figure 6.11. The respective AFM images for films on c-sapphire and c-ZnO can be seen in figure A.5.

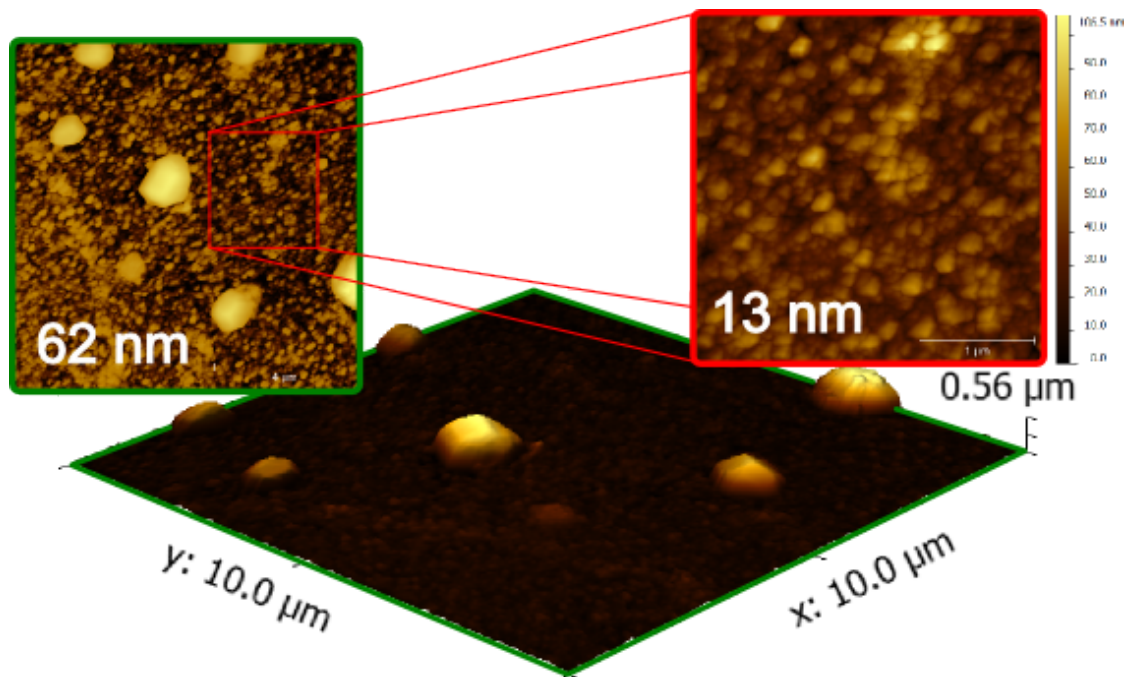


Figure 6.10 A detailed look at AFM scans of E3304 grown at 400 W and 3×10^{-4} mbar on a-sapphire. Droplets of diameters between 0.5 and $1.5 \mu\text{m}$ and heights between 300 and 500 nm are clearly visible. The RMS roughness of 13 nm in the $3 \times 3 \mu\text{m}^2$ scan represents the actually attainable surface roughness at the given growth conditions.

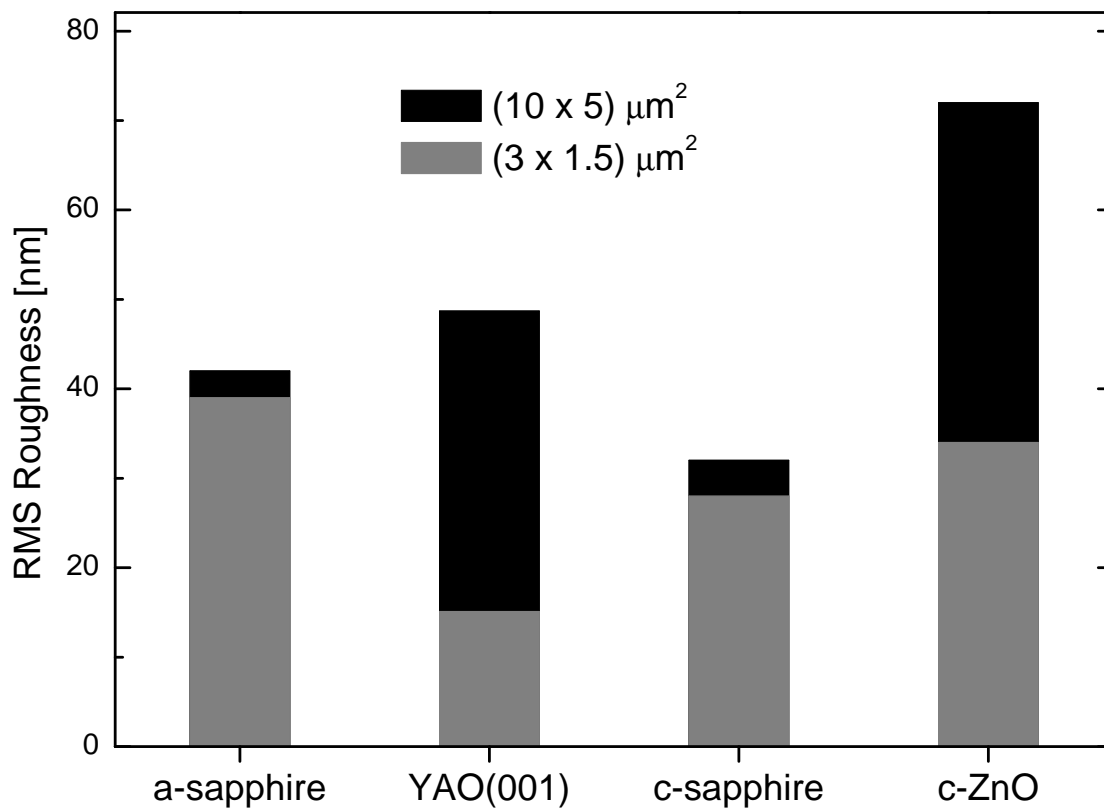


Figure 6.11 Surface roughness (RMS) of Na_2IrO_3 thin films grown on four different substrates at 400 W and 0.016 mbar.

6.1.3 Chemical Film Composition and Surface Corrosion

An early pressure series of Na₂IrO₃ thin films grown on a-sapphire at 400 W was studied by means of energy dispersive X-ray spectroscopy (EDX) to obtain the Na:Ir ratio which should be equal to 2:1 (or 66% and 33%) for the expected stoichiometry. This particular EDX analysis was done by Mr. Jörg Lenzner of HLP. Table 6.2 shows the results.

Table 6.2 Energy dispersive X-ray analysis of a pressure series of Na₂IrO₃ thin films grown on a-sapphire at 400 W. Shown are the Na:Ir ratios in atomic percent obtained from averaging the results of analyses on three different points on each sample.

Pressure [mbar]	0.6	0.3	0.1	0.016	0.002	3×10^{-4}
Na [at %]	0.69	0.66	0.61	0.56	0.61	0.59
Ir [at %]	0.31	0.34	0.39	0.44	0.39	0.41

Except for partial pressures of 0.016 mbar and 3×10^{-4} mbar the Na:Ir ratios are very close to the expected 66% and 33% ratio for Na₂IrO₃. Deviations from the expected ratio at pressures of 0.3 mbar and below are most likely caused by evaporation of Na during growth, where the high temperatures and low pressures are especially beneficial for evaporation. Reduced Na:Ir ratios make the presence of other sodium iridate phases conceivable and explain the observations of a crystalline phase of Na₄Ir₃O₈ in the XRD data (cf. Sec. 6.1.1). Let it be noted here, that a Na:Ir ratio of 57% to 43% would in fact precisely correspond to this closely related phase of Na₄Ir₃O₈. However, Na₄Ir₃O₈ was reported to have a thermally activated insulating behaviour with an activation energy of 43 meV and a room temperature resistivity of 0.1 Ωm [14]. All this is in variance with the findings of variable range hopping conductivity and room temperature resistivities of at least an order of magnitude lower (cf. Sec. 6.2).

During the study of Na₂IrO₃ thin film samples, a degradation in conjunction with a corrosion of the sample surface became apparent. At times, corrosion set in as early as a few hours after deposition. The surface turned dull and sometimes a white precipitate could be seen. Close-up views of the film surface were done with light and scanning electron (SEM) microscopes (Fig. 6.12). The images clearly reveal the rough surface of the studied samples explaining the surface turning dull. One can even see little crystals growing on the surface. Backscattered electron (BE) images (Fig. 6.13) at 600x and 4000x magnification reveal the stoichiometric inhomogeneity of the surface.

In combination with an EDX analysis, the dark areas can be shown to be Na-rich compared to the lighter areas. At 4000x one can make out grains with sizes in the order of micrometers. Their grain boundaries appear to be accumulated with sodium. In general, it is possible that sodium Na reacts with air moisture H_2O to form solid sodium hydroxide NaOH.

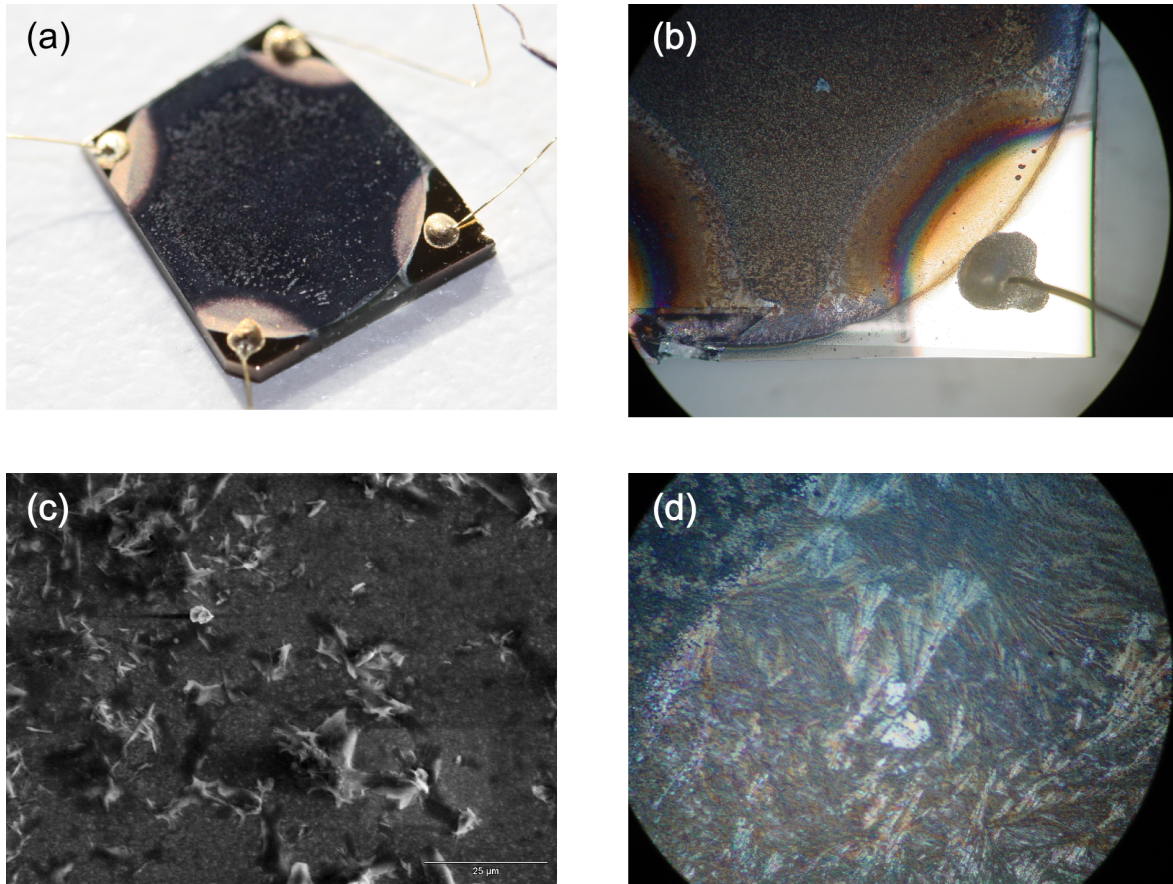


Figure 6.12 Surface corrosion after varying exposure to air (hours and days, not logged). (a) Photograph of a 5 mm \times 5 mm Na_2IrO_3 thin film sample with contacts in van-der-Pauw geometry. (b),(d) Light microscope images. (c) SEM image at 1000x magnification.

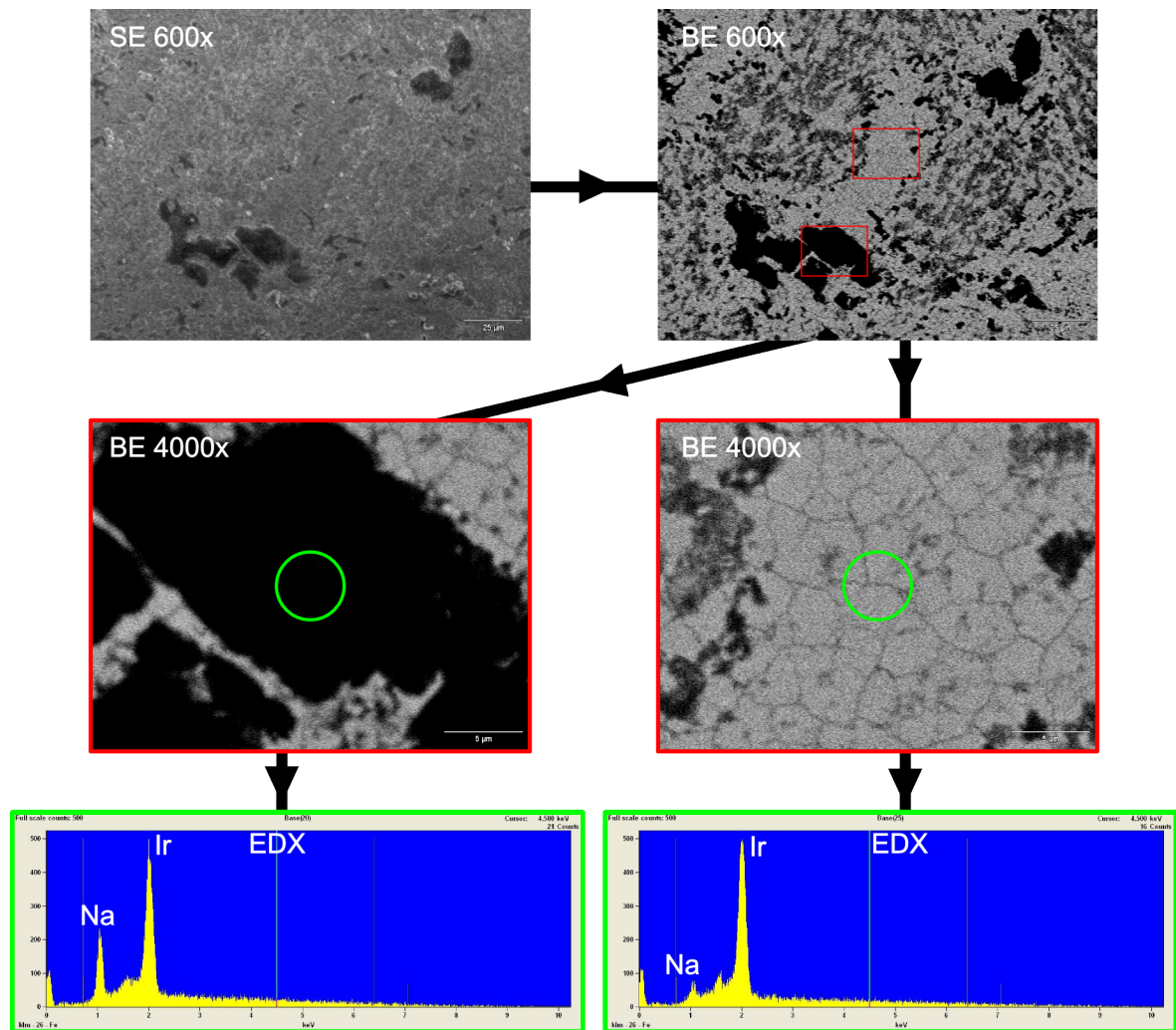


Figure 6.13 SEM, BE and EDX analysis of a Na_2IrO_3 thin film sample illustrating the surface inhomogeneities after several days of exposure to air. EDX reveals, that black areas in BE contain more Na than lighter ones. At 600x magnification an image corresponds to about $138 \mu\text{m} \times 184 \mu\text{m}$, at 4000x magnification to about $21 \mu\text{m} \times 27 \mu\text{m}$.

6.2 Temperature Dependent Electrical Resistivity

Temperature dependent resistivity measurements from 300 K down to 30 K were performed with a Hall setup in van-der-Pauw geometry. The thin film samples had dimensions of $5 \times 5 \text{ mm}^2$ and gold contacts were DC-sputtered at the corners. The evaluation of the temperature dependent Hall data is limited to resistivity only, because individual Hall coefficients were inconsistent repeatedly changing sign - both at one given temperature and within a range of temperatures. Consequently, also charge carrier concentrations and Hall mobility, which often fluctuated by an order of magnitude within the measured temperature interval, were not evaluated.

Figure 6.14 shows the DC electrical resistivity for a series of Na_2IrO_3 thin films grown on a-sapphire at 400 W presented in different scales. A log-lin plot of $\rho(T)$ (Fig. 6.14(a)) clearly reveals an insulating behaviour for all applied pressures. At the highest pressure, resistivity at 300 K is around $2.4 \times 10^{-4} \Omega\text{m}$ and increases by two orders of magnitude to $2.8 \times 10^{-2} \Omega\text{m}$ at 3×10^{-4} mbar. As semilogarithmic ρ versus $1/T$ plot in figure 6.14(b) shows, the resistivity does not follow an Arrhenius law $\rho(T) \propto \exp(-\Delta/T)$ over an extended range of temperature. Figure 6.14(c), however, reveals that resistivity follows a $\rho(T) \propto \exp[(T_0/T)^{1/4}]$ dependence over the widest continuous range of temperatures, that is from 300 K to at least 50 K. Such a dependence agrees well with single crystals of Na_2IrO_3 [4] and is usually associated with three-dimensional variable range hopping (VRH) of carriers localized by disorder as stated in section 2.6.

The dependence of the resistivity on growth temperature is shown in figure 6.15. Here, all samples were grown on a-sapphire at 3×10^{-4} mbar and pressures as indicated. A dominance of variable range hopping between 300 K and at least 50 K can once again be established for heater powers up to 550 W. In fact, the thin film grown at 600 W shows metallic behaviour over the entire range of temperatures. In this case, XRD revealed the absence of a (001) oriented Na_2IrO_3 phase and instead uncovered the dominant existence of Ir/IrO-species, implying a significant evaporation of Na from the sample (see Fig. 6.3). Inherent to an increases of heater power is the decrease of resistivity of the films: $\rho(T = 300\text{K})$ decreases from $2.8 \times 10^{-2} \Omega\text{m}$ to $3.2 \times 10^{-3} \Omega\text{m}$.

The same resistivity measurements as mentioned above were also done on Na_2IrO_3 thin films grown on YAO(001). Figure 6.16 shows the pressure series at 400 W. An insulating behaviour over the entire range and the tunability of resistivity with oxygen partial pressure can also be observed on YAO. With $9.0 \times 10^{-5} \Omega\text{m}$ at 0.1 mbar and

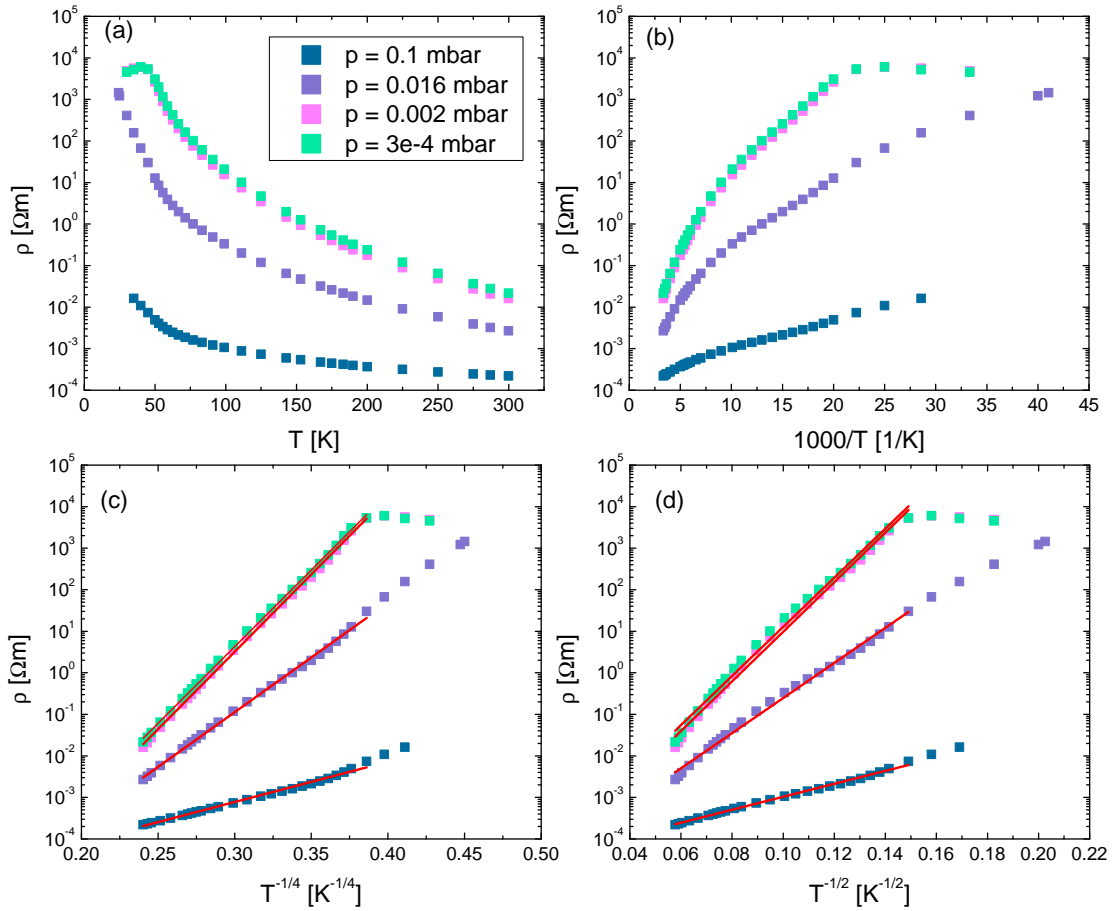


Figure 6.14 Temperature dependent resistivity for a pressure series of Na_2IrO_3 thin films grown on a-sapphire at 400 W. Data is plotted in different scales: (a) log-lin $\rho(T)$, (b) log-lin $\rho(1/T)$, (c) log-lin $\rho(T^{1/4})$ and (d) log-lin $\rho(T^{1/2})$. Straight lines in (c) and (d) indicate a Mott and Efros-Shklovskii (ES) variable range hopping conductivity mechanism. Red lines are fits to the data according to equation (2.46) with $p = 1/4$ (c) and $p = 1/2$ (d) fixed.

$2.9 \times 10^{-2} \Omega\text{m}$ at 3×10^{-4} mbar, the tuning of resistivity is larger than on a-sapphire. Furthermore, variable range hopping again is the dominant conduction mechanism.

Thin films on YAO(001) were also grown at a fixed pressure of 3×10^{-4} mbar but at various heater powers (Fig. 6.18). With heater power, the resistivity is tunable from $2.7 \times 10^{-2} \Omega\text{m}$ to $5.2 \times 10^{-3} \Omega\text{m}$ very similar to films on a-sapphire. Moreover, for all heater powers the semi-log plot of $\rho(T^{1/4})$ is a straight line pointing again to variable range hopping conductivity. Interestingly, also the film grown at 600 W shows insulating variable range hopping behaviour in variance with the film grown on a-sapphire under the same conditions, which was found to be metallic (cf. Fig.

So far, Na_2IrO_3 thin films have been established to be semiconducting and dominated by an insulating hopping conductivity mechanism in agreement with their single-crystalline equivalent. Also, resistivity is tunable by oxygen partial pressure and growth

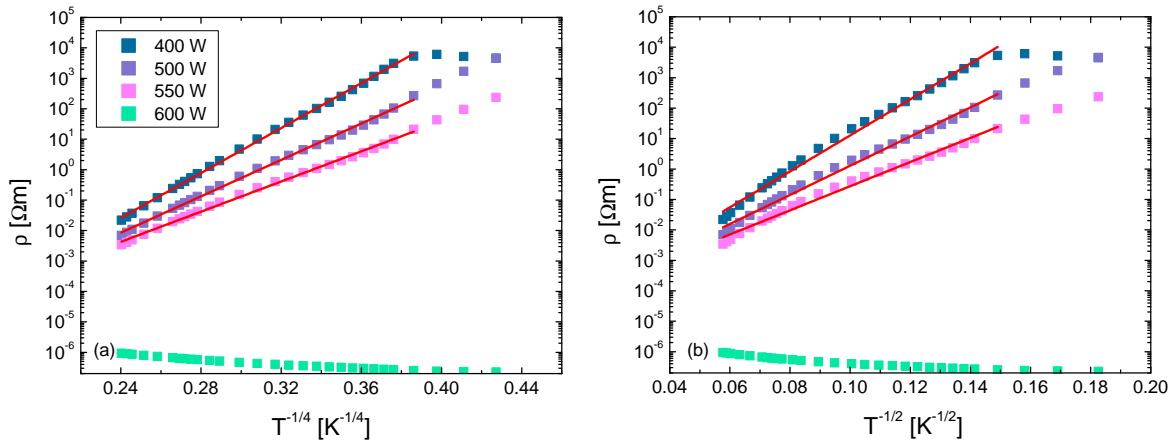


Figure 6.15 Temperature dependent resistivity for a series of Na_2IrO_3 thin films grown on sapphire at 3×10^{-4} mbar and heater power as indicated. Data is plotted in semi-logarithmically as (A) $\rho(T^{1/4})$ and (b) $\rho(T^{1/2})$. Straight lines in (a) indicate Mott-VRH. Red lines are fits to the data according to equation (2.46) with $p = 1/4$ (a) and $p = 1/2$ (b) fixed.

temperature by up to four orders of magnitude. However, the first report on variable range hopping in single-crystalline Na_2IrO_3 did not give a possible explanations for its occurrence. Hence in the following, the applicability of the variable range hopping conductivity models as discussed in section 2.6 will be reviewed.

The models on variable range hopping conduction, e.g. by Mott [76] and Efros & Shklovskii [71], are based on localized states inside a narrow optimum band $\epsilon_0(T)$ (see. Fig. 2.11). The Fermi level lies within this band and conduction is via thermally activated and phonon-assisted hopping. In the model systems carriers are localized by disorder and in fact, variable range hopping has been successfully applied to amorphous and disordered systems, however, usually at low temperatures. If the system had no significant electron correlations, the parameter p in equation (2.46) would be $1/4$ (Mott-VRH). If however, significant electron correlations were present, the narrow band would be gapped and $p = 1/2$ (ES-VRH). 6.15). In Mott-insulating Na_2IrO_3 , localization of states on the one hand is caused by strong on-site Coulomb interactions of the Ir 5d orbitals, but to some degree also induced by frequent stacking faults and interatomic site mixings [16,66,67] causing structural disorder. Also, electron transfer is mainly via the edge-shared IrO_6 octahedra with direct Ir-Ir and indirect Ir-O-Ir hoppings of various range [61,95,96]. Furthermore, the Ir 5d- t_{2g} bands have been found to be narrow, both in this work (Sec. 6.4) and in [89]. There exists a small insulating Coulomb gap in the range between 200 meV (this work, see Sec. 6.4) and 350 meV [89]. Naturally, the Fermi level is inside this gap, thus rendering the system insulating. To sum up, some important requirements in the applicability of variable range hopping to Na_2IrO_3 are met.

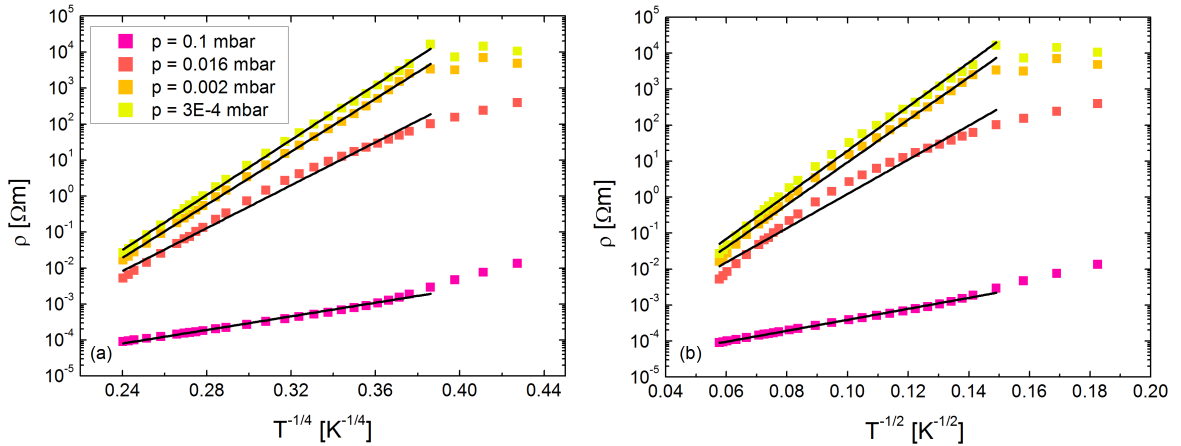


Figure 6.16 Temperature dependent resistivity for a series of Na_2IrO_3 thin films grown on YAO(001) at 400 W and oxygen partial pressures as indicated. (a) Semi-log plot of $\rho(T^{1/4})$. (b) Semi-log plot of $\rho(T^{1/2})$. Black lines are fits to the data according to equation (2.46) with $p = 1/4$ (a) and $p = 1/2$ (b) fixed.

Some quantitative analysis of the resistivity data was also done. Plotting either $\ln\rho$ vs. $(1/T)^{1/4}$ or $\ln\rho$ vs. $(1/T)^{1/2}$ linearly, a linear regression of the form $\ln\rho = \ln\rho_0 + T_0^p \cdot (1/T)^p$ was performed in the range from 300 K to 50 K. To determine which type of variable range hopping best fits the data the goodness of fit described by the adjusted sum of squares *adj. R*² is compared for $p = 1/4$ and $p = 1/2$, respectively (Tab. 6.3). Even though the difference between the respective *adj. R*² is marginal for all samples, $p = 1/4$ describes the data best - with the exception of films grown at 400 W and 0.1 mbar (see Figs. 6.14 to 6.18). If Mott-VRH were applicable even in the presence of a Coulomb gap, then the Coulomb gap should be narrower than the bands it gaps.

Measurements of resistance R down to 2 K were performed by Mr. Barzola of the Division of Superconductivity and Magnetism (SUM) on sample E3254 grown on YAO(001) at 400 W and 0.016 mbar. The sample was contacted at all four corners with DC-sputtered gold contacts. A current of 10 μA was applied to two pairs of contact perpendicular to each other (channel 1 and 2) and the resistance at a given temperature was then determined from the measured voltage. The result are shown in figure 6.17. One can observe a clear peak in the resistance at around 15 K, which interestingly coincides well with the antiferromagnetic ordering temperature T_N determined by several experimental methods to lie in between 13.3 K and 18.1 K [4, 65–67]. The data shows Mott-VRH behaviour from 300 to 50 K supported by the goodness of fit (cf. Tab. 6.3). At lower temperatures there are diversions from a straight line. Channels 1 and 2, corresponding to different pairs of contacts, are quantitatively different, which points at sample inhomogeneities. The resistance at 0°C is 370 Ω for channel 1 and 2 Ω for channel 2. Below 65 K, however, channel 2 shows higher resistance. In the straight

line fits according to Mott variable range hopping (eq. 2.46) as shown in figure 6.17, this also results in a different slope T_0 of 33.28 K and 39.27 K for channel 1 and 2, respectively.

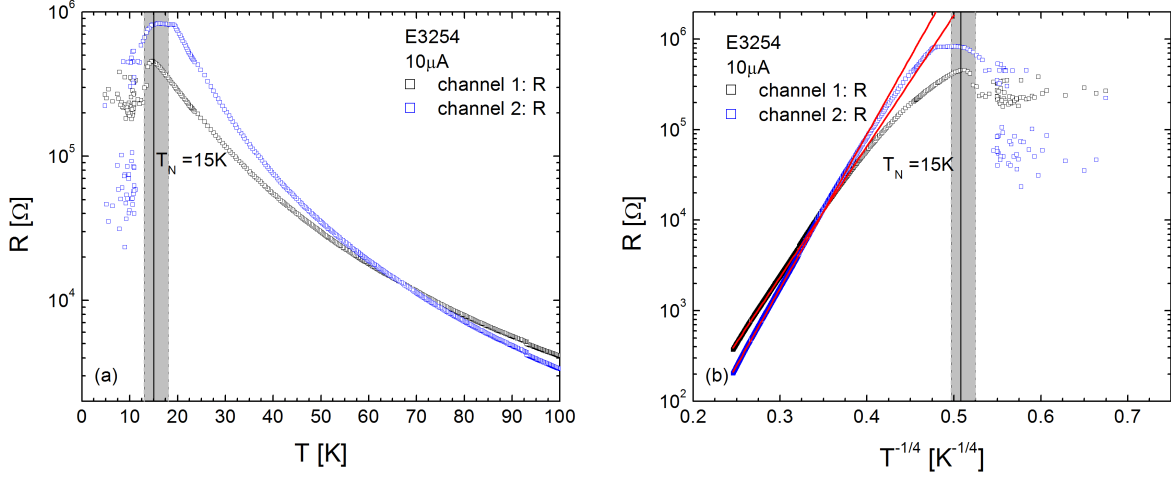


Figure 6.17 Resistance at very low temperature. Resistance vs. temperature from 273 K to 2 K of Na_2IrO_3 thin film E3254 grown on YAO(001) at 400 W and 0.016 mbar. Semi-log plots of (a) $\rho(T)$ and (b) $\rho(T^{1/4})$ show an anomaly around 15 K coinciding with reported antiferromagnetic ordering temperatures T_N of Na_2IrO_3 single crystals. Red lines in (b) are straight line fits indicating Mott-VRH from 300 K to 50 K. Measured by J. Barzola (SUM).

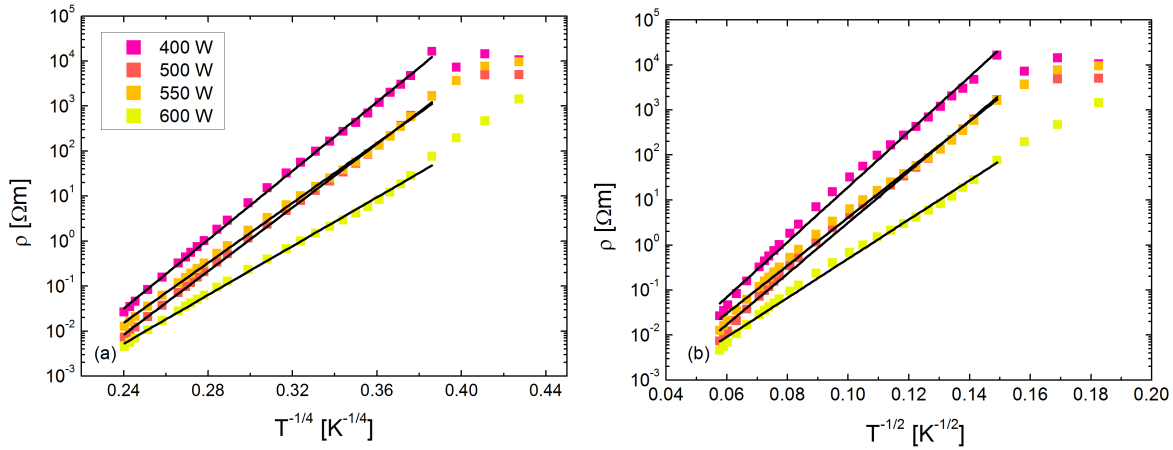


Figure 6.18 Temperature dependent resistivity for a temperature series of Na_2IrO_3 thin films grown on YAO(001) at 3×10^{-4} mbar and oxygen partial pressures as indicated. (a) Semi-log plot of $\rho(T^{1/4})$. (b) Semi-log plot of $\rho(T^{1/2})$. Black lines are fits to the data according to equation (2.46) with $p = 1/4$ (a) and $p = 1/2$ (b) fixed.

At this point, however, it remains an open question why in Na_2IrO_3 variable range hopping extends to temperatures as high as 300 K. In the theoretical treatment of variable range hopping by means of percolation theory (Sec. 2.6) a critical temperature T_C (Eq. 2.42) is given. Above this critical temperature there is a gradual transition

from the variable range hopping type conductivity to nearest-neighbour hopping. For nearest-neighbour hopping, charge carriers hop to nearest neighbours only and the resistivity is of an activated type with $\rho \propto \exp(1/T)$ (cf. eq. 2.43). Making reasonable assumptions [85] for the wavefunction decay radius $a = 10 \text{ \AA}$, the density of charge carriers $N = 10^{18} \text{ cm}^{-3}$ and the width of the narrow band $2\Delta E = 500 \text{ meV}$ (cf. Sec. 6.4), one only obtains a critical temperature of $T_c \approx 84 \text{ K}$. However, the observed variable range hopping conductivity extends well beyond 84 K.

Table 6.3 Electrical properties of Na_2IrO_3 thin films determined by temperature dependent measurements of resistivity in van-der-Pauw geometry. Listed are the results of pressure and temperature series on a-sapphire and YAO(001), respectively. ρ_0 , T_0 and p are fit parameters according to eq. (2.46). The goodness-of-fit is given in terms of the adjusted R^2 in the last two columns.

a-sapphire pressure series (400 W):					adj. R^2	
Sample no.	Pressure [mbar]	$\rho(300 \text{ K}) [\Omega\text{m}]$	$\rho_0 [\Omega\text{m}]$	$T_0 [\text{K}]$	p=1/4	p=1/2
E3298	0.1	2.4×10^{-4}	9.64×10^{-7}	3.68×10^4	0.99162	0.99673
E3302	0.016	3.3×10^{-3}	1.40×10^{-9}	1.73×10^5	0.99821	0.99479
E3312	0.002	1.7×10^{-2}	2.14×10^{-11}	3.64×10^5	0.99918	0.99422
E3315	3×10^{-4}	2.773×10^{-2}	3.62×10^{-11}	3.34×10^5	0.99906	0.99304
a-sapphire temperature series (3×10^{-4} mbar):					adj. R^2	
Sample no.	Heater Power [W]	$\rho(300 \text{ K}) [\Omega\text{m}]$	$\rho_0 [\Omega\text{m}]$	$T_0 [\text{K}]$	p=1/4	p=1/2
E3315	400	2.8×10^{-2}	3.62×10^{-11}	3.34×10^5	0.99906	0.99304
E3316	500	7.5×10^{-3}	5.67×10^{-10}	2.05×10^5	0.99777	0.99225
E3318	550	3.2×10^{-3}	4.84×10^{-9}	1.34×10^5	0.99701	0.98964
E3323	600	9.3×10^{-7}	-	-	-	-
YAO(001) pressure series (400 W):					adj. R^2	
Sample no.	Pressure [mbar]	$\rho(300 \text{ K}) [\Omega\text{m}]$	$\rho_0 [\Omega\text{m}]$	$T_0 [\text{K}]$	p=1/4	p=1/2
E3337	0.1	9.0×10^{-5}	4.28×10^{-7}	4.62×10^4	0.98506	0.99399
E3342	0.016	7.1×10^{-3}	5.87×10^{-10}	2.04×10^5	0.98904	0.97328
E3345	0.002	1.6×10^{-2}	2.78×10^{-11}	3.49×10^5	0.99886	0.99298
E3346	3×10^{-4}	2.9×10^{-2}	2.13×10^{-11}	3.65×10^5	0.99885	0.9935
YAO(001) temperature series (3×10^{-4} mbar):					adj. R^2	
Sample no.	Heater Power [W]	$\rho(300 \text{ K}) [\Omega\text{m}]$	$\rho_0 [\Omega\text{m}]$	$T_0 [\text{K}]$	p=1/4	p=1/2
E3346	400	2.9×10^{-2}	2.13×10^{-11}	3.65×10^5	0.99885	0.9935
E3354	500	7.3×10^{-3}	2.75×10^{-11}	3.50×10^5	0.99882	0.99485
E3355	550	1.3×10^{-2}	1.59×10^{-10}	2.59×10^5	0.99801	0.99322
E3356	600	4.6×10^{-2}	1.64×10^{-9}	1.67×10^5	0.99738	0.99383

6.3 Magnetic Properties

SQUID magnetometry and magnetoresistance measurements were performed on samples of Na_2IrO_3 thin films by J. Barzola-Quiquia of the Division of Superconductivity and Magnetism. For the magnetic moment measurements a superconducting quantum interferometer device (SQUID) from Quantum Design was used.

Magnetic moment m versus applied external field H was measured in the zero field cooled states (ZFC) at 5 K and 50 K, i.e. below and well above the Néel temperature T_N of about 15 K for Na_2IrO_3 single crystals [4, 65–67]. The thin film measured here was grown on a c-sapphire substrate at 400 W and 0.016 mbar and covered by a 110 nm SiN_x protective layer by means of PECVD (sample no. E3313). After subtraction of the diamagnetic contribution of the substrate, at both 5 K and 50 K a hysteresis loop is discernible (Fig. 6.19). For both sets of data, magnetic moment begins to saturate above fields of ± 2500 Oe. At 50 K, the magnetic moment saturates at $3 \mu\text{emu}$ which is at the very low end of the measurement range. It is comparable in order of magnitude to typical contributions of the substrate contaminated with magnetic impurities [97].

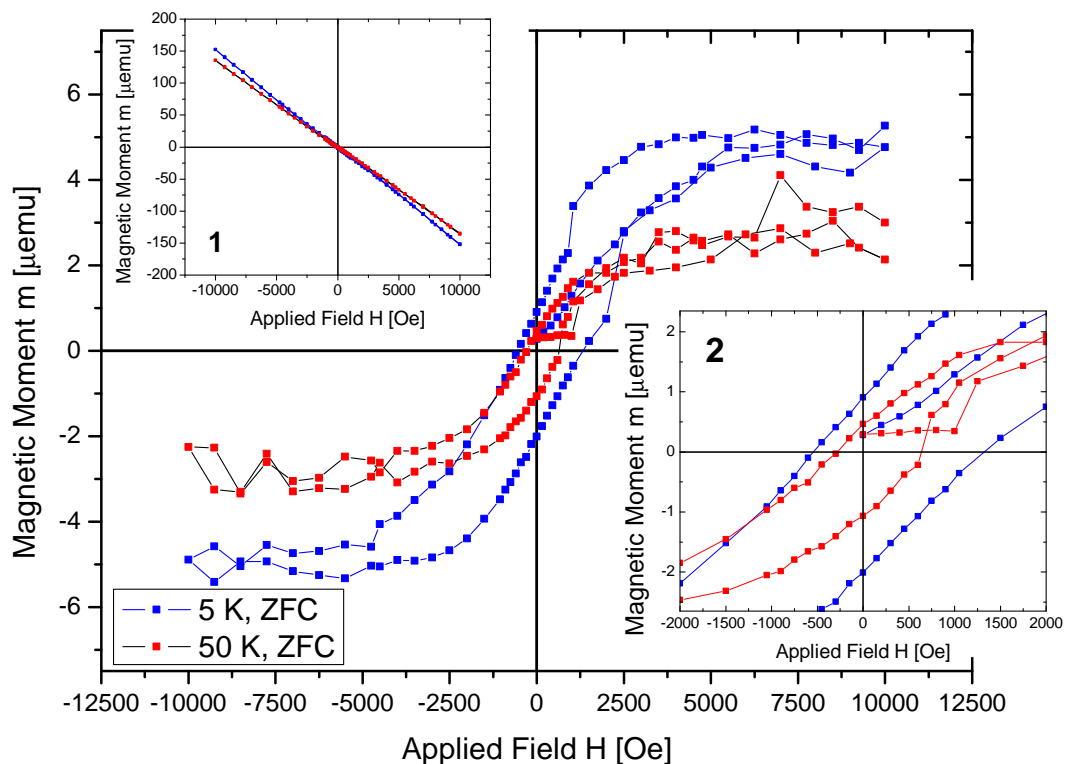


Figure 6.19 Field hysteresis of magnetic moment $m(H)$ at 5 K and 50 K. Shown are ZFC states of a Na_2IrO_3 film grown on c-sapphire. The diamagnetic contribution of the substrate was subtracted. Inset 1 shows $m(H)$ before subtraction of the diamagnetic contribution. Inset 2 shows a zoom-in of the hysteresis loops between applied fields of ± 2000 Oe.

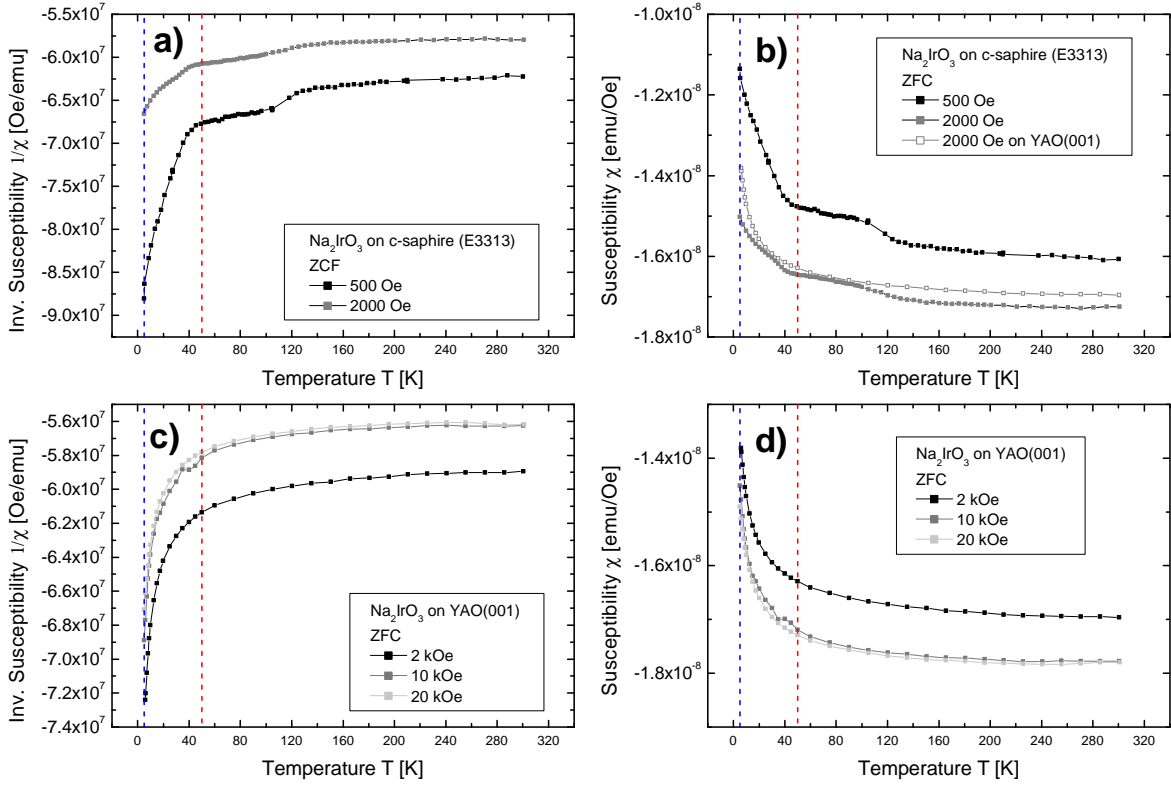


Figure 6.20 (a,c) Inverse magnetic susceptibility $1/\chi = H/m$ versus temperature T of thin films grown on c-sapphire and YAO(001) at various applied fields between 500 Oe and 20 kOe. (b,d) Magnetic susceptibilities χ for the same samples. The blue and red dashed lines mark 5 and 50 K, respectively.

Below the Néel temperature of 5 K, i.e. in the antiferromagnetic ordering regime, the saturation magnetic moment is slightly higher with about $5 \mu\text{emu}$. The field-dependent magnetic moment shows pronounced asymmetries in the field and magnetic moment axes. Compared to the 50 K data, coercivity fields and remnant magnetic moments are higher (cf. inset of Fig. 6.19). Such asymmetries can be related to exchange couplings between ferromagnetic (FM) and antiferromagnetic (AFM) phases as present for instance in FM/AFM bilayer materials [98]. Experimentally, this exchange coupling is observed as horizontal and/or vertical shifts of the hysteresis loop with temperature. In our case such exchange bias effects could result from the finite size of crystallites. Crystallites of sufficiently small size lose their AFM long-range order, s.t. possible local structural and stoichiometric variations could lead to ferromagnetism. Consequently, ferromagnetic crystallites were embedded in the otherwise antiferromagnetic matrix. Then, the exchange coupling between their interfaces would cause the observed asymmetries.

Inverse magnetic susceptibility $1/\chi = H/m$ versus temperature between 5 K and 300 K was obtained from temperature dependent measurements of magnetic moment in

applied fields ranging from 500 Oe to 20,000 Oe. The measurements were performed on samples E3313 (Figs. 6.20a,b), grown on c-sapphire and used in above $m(H)$ measurements, and sample E3253 (Figs. 6.20c,d) which was grown on YAO(001) at 400W and 0.016 mbar. Sample E3253 was not covered by a SiN_x layer.

The inverse magnetic susceptibility monotonously decreases with temperature; the absolute value decreases with applied field. Also, the (inverse) magnetic susceptibility data at 500 and 2000 Oe of the film grown on c-sapphire each have a dent between 40 and 120 K. This is at variance with the otherwise smooth curve progression of the film grown on YAO(001). Moreover, the data at 2000 Oe for the films on either substrates c-sapphire and YAO(001), respectively, does not compare (cf. Fig. 6.20b). Unlike in a recent experiment [4] on Na_2IrO_3 single crystals, neither a Curie-Weiß law can be fitted to the data in any extended range of temperatures, nor can a maximum in $\chi(T)$ be observed that would highlight the onset of antiferromagnetic order. It is presumed that like in measurements of the $m(H)$ hysteresis, magnetic properties of the thin film are masked by a contribution of the substrate to the already small signal.

Magnetoresistance (MR) measurements between 2 and 100 K were performed on E3313 and on another sample E3314 where a shadow mask was used to apply gold contacts in a Hall bar geometry via the sputtering technique (cf. Fig. 5.4). Again, the film was first grown on c-sapphire at 400 W and 0.016 mbar and afterwards covered with a 110 nm SiN_x protective layer.

First, let sample E3314 measured between 2 K and 25 K and at a fixed current of 5 μA be considered. The normalized magnetoresistance $[R(B) - R(B = 0)]/R(B = 0)$ (Fig. 6.21) increases monotonously from zero applied field up to fields of ± 8 Tesla for all temperatures. In fields above ± 4 T it scales well with B^2 as the fits (straight lines) indicate and there is no saturation at higher fields. In lower fields (< 3 T), a simple B^2 dependence cannot be found. The parabolalike dependence at high fields originates from Lorentz deflections of carriers in perpendicular fields [99]. However at 2 K, the deviation below 3 T is that of a broad cusp indicating the presence of a weak anti-localization (WAL) effect associated with topological surface states [21]. The WAL effect originates from strong spin-orbit coupling that reduces backscattering of carriers to a minimum at zero field due to time-reversal symmetry. Applied magnetic fields break said symmetry causing an unusual rise in resistance. At 10 K the cusp has already straightened out and a WAL effect can no longer be observed.

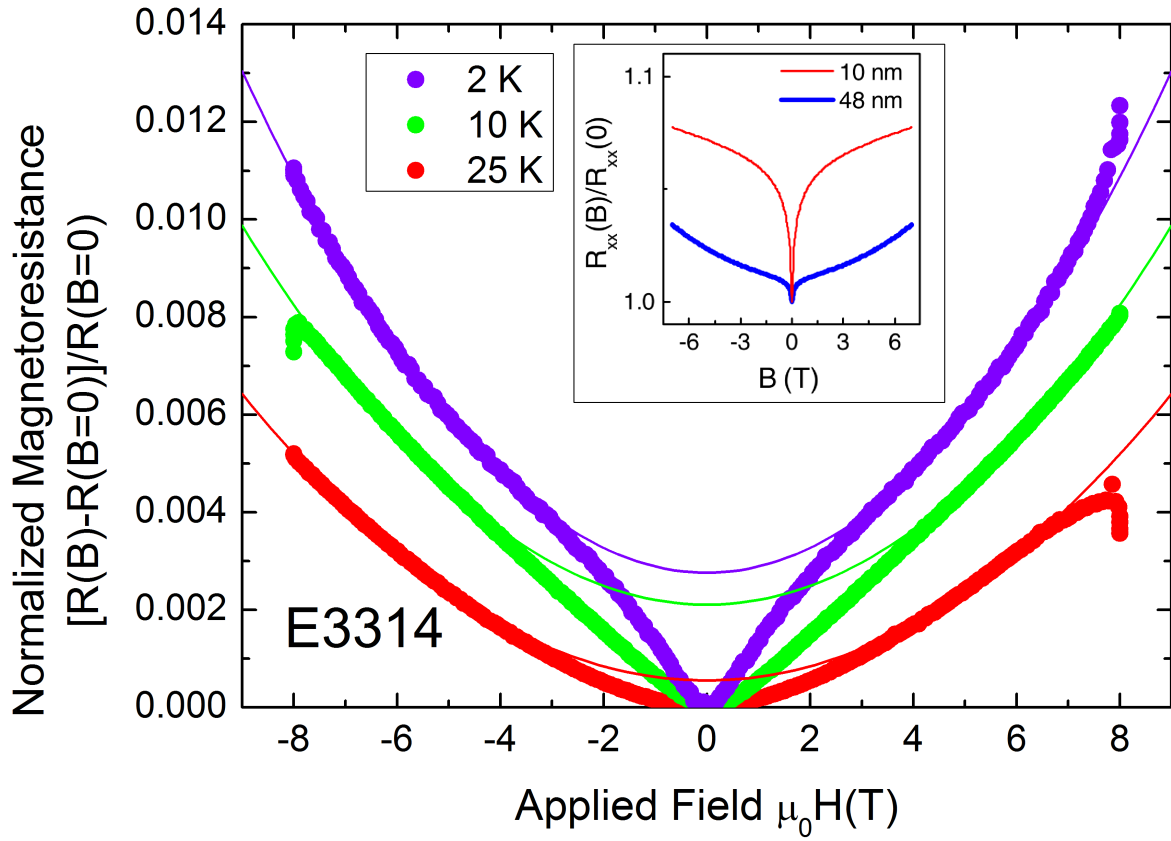


Figure 6.21 Normalized magnetoresistance $[R(B) - R(B = 0)]/R(B = 0)$ (MR) between 2 K and 25 K and at a fixed current of $5 \mu\text{A}$ measured on sample E3314 covered by a SiN_x protective layer. Straight lines are fits according to a simple B^2 dependence. For comparison, the inset shows the MR of two samples of epitaxially grown Bi_2Se_3 thin films at 1.8 K, where the weak antilocalization effect was reported [28].

Weak antilocalization can also be observed in the magnetoresistance data of samples E3313 and E3314 at $1 \mu\text{A}$ (6.23). For both samples the effect persists up to 4 K. However, it is more pronounced at 2 K for sample E3314. From 10 K onwards the observed cusps begin to straighten out. In fact, the data compares surprisingly well with published magnetoresistance data of known topological insulators (cf. Fig. 6.22).

To summarize, the thin film susceptibility data was not compatible with measurements on bulk crystals and no signs of antiferromagnetic order could be uncovered. However, a field-dependent magnetic moment measurement at 5 K showed signatures of antiferromagnetic order, as found in Na_2IrO_3 single crystals, together with an exchange bias effect due to AFM/FM interfaces inside the Na_2IrO_3 thin film. Via the observation of a weak antilocalization effect, magnetoresistance measurements between 2 and 100 K point at the existence of topological surface states below 4 K even after exposure to air.

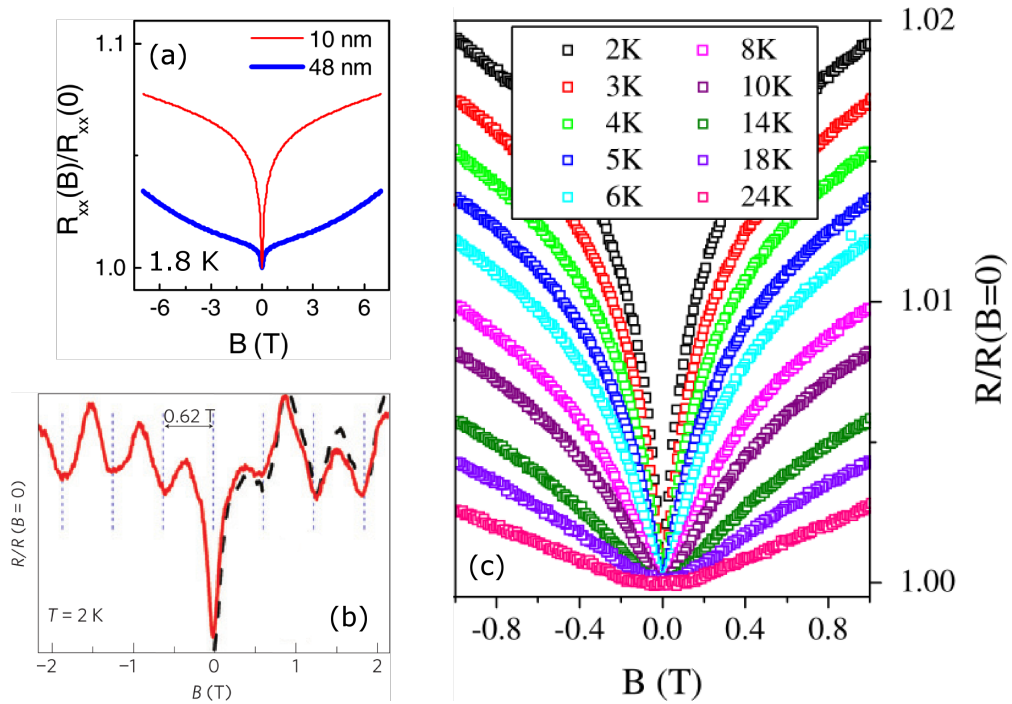


Figure 6.22 Weak antilocalization effect observed in magnetoresistance of strong topological insulators. (a) Two samples of epitaxially grown Bi_2Se_3 thin films at 1.8 K [28]. (b) A Bi_2Se_3 nanoribbon at 2 K shows the WAL effect with a sharp cusp at zero field [100]. (c) WAL effect in a 5 nm Bi_2Te_3 thin film at low temperatures [101].

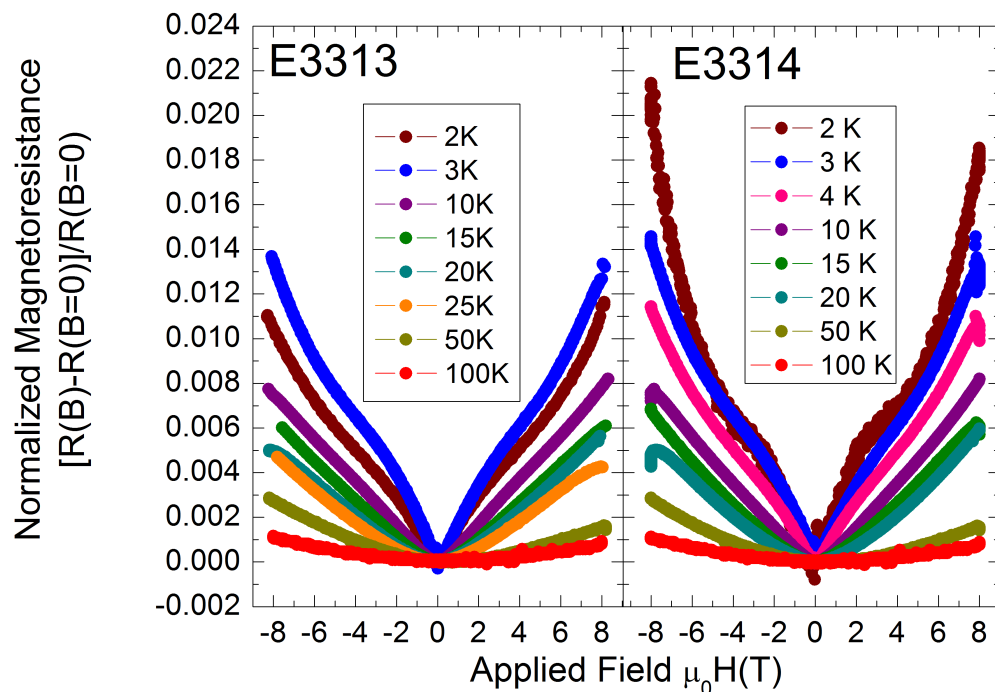


Figure 6.23 Normalized magnetoresistance $[R(B) - R(B = 0)]/R(B = 0)$ (MR) between 2 K and 100 K and at $1 \mu\text{A}$ measured on samples E3313 (van-der-Pauw contacts) and E3314 (Hall bar contacts) both covered by a SiN_x protective layer.

6.4 Optical Properties

To study the low- and high-energy optical properties of Na_2IrO_3 thin films, optical conductivity (OC) measurements, optical transmission (OT) spectroscopy and Fourier transform infrared spectroscopy (FTIR) in the wide range between 0.025 eV and 6.200 eV and at ambient conditions were performed. The measurements were performed on three different samples. They were grown at 0.016 mbar and 400 W on c-sapphire for OC and OT. For FTIR, a sample grown on a-sapphire at 0.016 mbar and 500 W was used. Optical conductivity was determined by the inverse electrical resistance $1/R = I/V$ measured at a given energy of incident light. For this matter the sample was contacted with four DC-sputtered gold contacts.

Figure 6.24(a) displays the results of all three measurements from 0 to 6 eV. FTIR (black) and optical transmission (blue) data are given as absorptance; optical conductivity is shown in red. Apart from a phononic feature [89] at 180 meV (see inset), FTIR absorptance data reveals an absorption edge starting at 200 meV indicating a small optical gap. This is in good agreement with a recent experiment [89] on Na_2IrO_3 single crystals where the insulating gap between the Ir 5d- t_{2g} bands was estimated around 350 meV by combining ARPES observations of chemical potential shift with carrier doping and optical conductivity measurements (cf. Fig. 3.3). In the FTIR data, absorptance monotonously increases and saturates at around 450 meV. At higher energies the FTIR data is increasingly governed by noise.

Optical transmission data (blue) is available from 0.6 eV onwards (see Fig. 6.24(b)). However, the data is rather noisy up to energies of 1.5 eV. Nevertheless, between 600 and 800 meV the signal first decreases, possibly representing the high-energy flank of the feature observed in the FTIR data above 200 meV. For further discussion, let both observations in FTIR and OT be combined into one narrow peak α with a maximum at around 0.6 eV. In the OT data above 800 meV absorptance again increases and one can observe another wide feature between 0.8 and 2.3 eV with a maximum at 1.5 eV (6.24(b)). This feature will be denoted as β . A similar feature can also be seen in the optical conductivity data (red) at a slightly lower energy of 1.4 eV. In both the transmission and OC data, the signal continuously increases above 2.3 eV. While the OT signal goes into saturation above 3 eV, the optical conductivity continues to rise. Let this third feature be denoted as γ (6.24(a)).

Based on recent ARPES data of Na_2IrO_3 single crystals at 130 K [89], the low energy

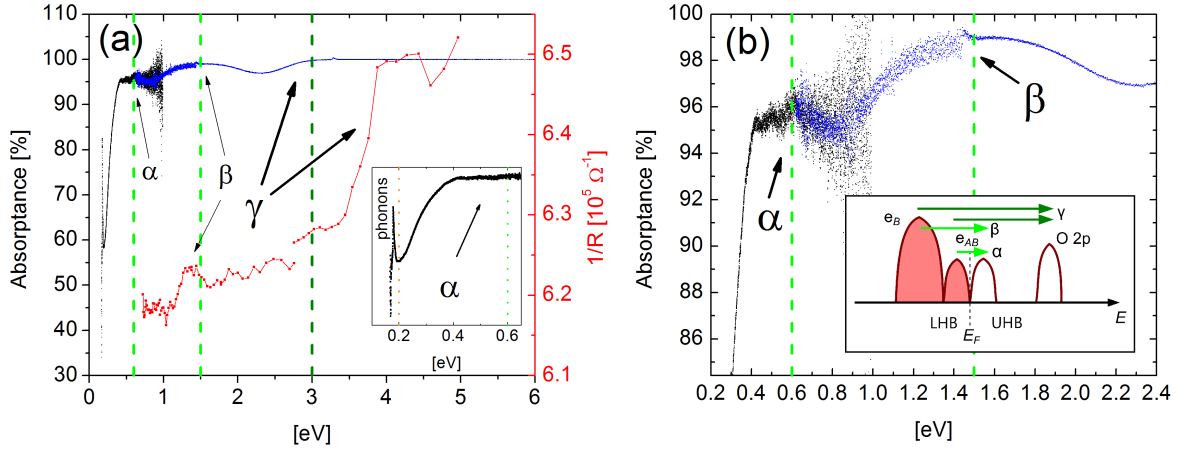


Figure 6.24 Optical properties of Na_2IrO_3 thin films determined by optical conductivity (red) measurements, optical transmission spectroscopy (blue) and Fourier transform infrared spectroscopy (black) at ambient conditions. (a) Full measured spectral range shows three absorption peaks α , β , γ . The inset shows a zoom-in on the FTIR data below 0.6 eV indicating a small optical gap of ≈ 200 meV. (b) Low energy absorption peaks α at 0.6 eV and β at 1.5 eV as measured by FTIR and OT corresponding to intraband transitions within the Ir 5d- t_{2g} manifold [89]. The inset shows a schematic representation of the observed transitions that are similarly found in Ir_2O_4 [102].

absorptions α and β originate from the Ir 5d- t_{2g} manifold, while γ above 3 eV originates from O 2p states (cf. Fig. 3.3). Moreover, the observation of the two absorption peaks α and β implies a further splitting of the Ir 5d- t_{2g} manifold. This splitting is due to a delicate interplay between spin-orbit coupling, electron correlations and possible trigonal distortions [60, 61, 89] as discussed in section 2.3.1. Although experimental reports on the presence of trigonal distortions in the IrO_6 octahedra are conflicting [4, 66, 67], the low energy absorption peaks will be assigned according to a proposed level scheme [60, 61] where trigonal distortions were argued to be a necessary ingredients to obtain a zig-zag type AF magnetic order (see also Sec. 2.3.1).

In this spirit the electronic structure is summarized schematically in the inset of figure 6.24(b). Peak α at 600 meV is assigned to the Mott-Hubbard transition within the narrow half-filled e_{AB} doublet. The onset of absorption at 200 meV is thus equivalent to the order of magnitude of the insulating Mott gap. Next, peak β corresponds to the ≈ 1.5 eV intraband transition from the filled and degenerate e_B to the empty upper Hubbard band e_{AB} . The intraband transitions α and β are in fact similar to low energy transitions observed in Sr_2IrO_4 [8, 103] and Ir_2O_4 [104]. Lastly, the absorption spectrum above 3 eV (γ) can be assigned to the interband transitions from e_B and e_{AB} to empty O 2p states which was also observed in the other iridates Sr_2IrO_4 and Ir_2O_4 (see Fig. 6.25).

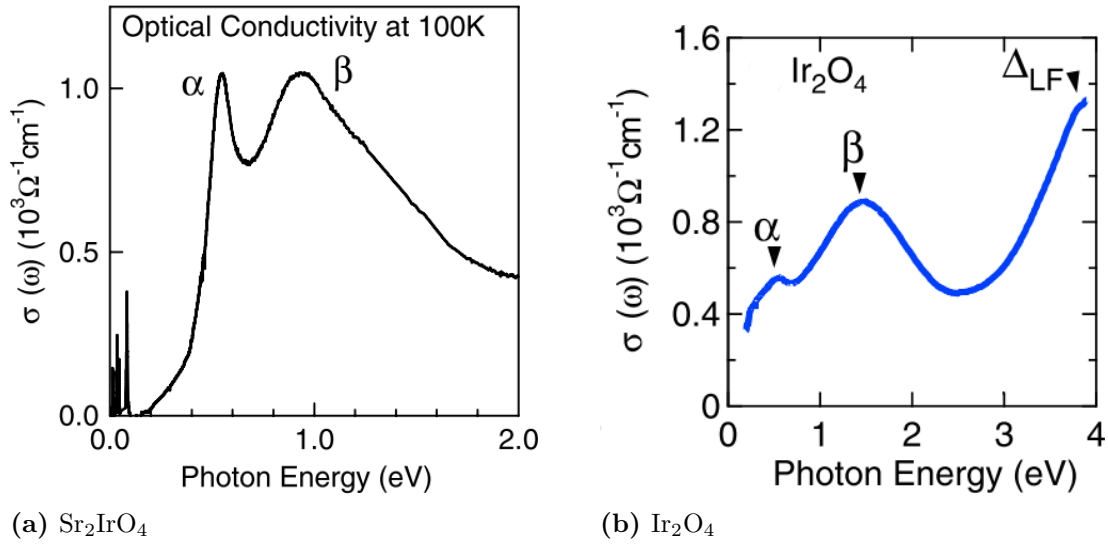


Figure 6.25 Optical conductivity $\sigma(\omega)$ data of single-crystalline Sr_2IrO_4 at 100 K (a) and of a Ir_2O_4 thin film at room temperature (b) show transitions α , β and Δ_{LF} that are similar to the ones observed in Na_2IrO_3 thin films of this work. (adapted from [8] and [102], resp.)

To sum up, in the optical measurements of Na_2IrO_3 thin films below 6 eV, experimental signatures of optical absorption were found, that agree surprisingly well with published data on single crystals of Na_2IrO_3 and also other iridate single crystals and thin films. In detail, the onset of a small insulating Mott gap was observed around 200 meV in reasonable agreement with Na_2IrO_3 single crystals [89]. Two distinct absorption peaks, narrow α at 0.5 eV and β at 1.5 eV, agree well with the proposed level scheme influenced by SOC, electron correlations and trigonal distortions supporting the notion of Na_2IrO_3 being a spin-orbit-assisted Mott insulating antiferromagnet.

7 Summary and Outlook

In this work, heteroepitaxial Na_2IrO_3 thin films were grown on various oxide substrates by means of pulsed laser deposition. The thin films were studied in terms of their structural, electrical, magnetic and optical properties.

Polycrystalline PLD targets were prepared by a solid state synthesis of Na_2CO_3 and IrO_2 powders. X-ray diffraction patterns of the final targets confirmed their Na_2IrO_3 phase. The deposition of Na_2IrO_3 thin films was done on four different substrates, that is a-plane sapphire, YAlO_3 (001), c-plane sapphire and c-plane ZnO employing a KrF excimer laser with a wavelength of 248 nm. During this study, the dependence of thin film properties on both oxygen partial pressure and growth temperature were investigated.

X-ray diffraction measurements on all substrates established that the thin films grow with an excellent (001) out-of-plane and in-plane orientation of Na_2IrO_3 , hence the films can be considered epitaxial. However, especially at the very highest growth temperatures the presence of other orientations of Na_2IrO_3 also other crystalline phases, such as $\text{Na}_4\text{Ir}_3\text{O}_8$, was discovered in the form of minor additional peaks. The XRD study further showed the tunability of the out-of-plane lattice constant with oxygen partial pressure and growth temperature within a range from 10.383 Å to 10.813 Å for the $C/2c$ unit cell and from 5.415 Å to 5.640 Å for the $C2/m$ unit cell. The reference values for single crystals with respect to the $C/2c$ and $C/2m$ unit cells are 10.765 Å and 5.614 Å, respectively.

Furthermore, the surface morphology of Na_2IrO_3 thin films was investigated by atomic force microscopy. There, the root mean squared roughness was determined and ranged from 11 nm to 143 nm. Obviously, the films consisted of crystallites of varying size. No dependence of surface roughness on PLD process parameters could unambiguously be determined and often droplets were found on the surface. Most probably, the mechanically soft PLD targets contribute to the rough film surface.

Temperature dependent resistivity measurements of films grown on a-sapphire and YAO showed an insulating $\rho \propto \exp(T^{-1/4})$ dependence in a large range of temperatures from 300 K down to at least 40 K. Previously, such a dependence was found in Na_2IrO_3 single crystals in a smaller range between 300 K and 100 K [4]. This observation was ascribed here to variable range hopping (VRH) of carriers between localized

states as the dominant conductivity mechanism. In excellent agreement with previous experimental reports on Na_2IrO_3 single crystals [4,66,67,89], the observation of variable range hopping confirmed the inherent presence of structural disorder, the existence of narrow bands in the vicinity of the Fermi level, and the localization of electronic states due to strong Coulomb repulsions consistent with a Mott insulator. The resistivity was generally tunable with oxygen partial pressure and growth temperature by up to four orders of magnitude. Room temperature resistivities ranged from $9.0 \times 10^{-5} \Omega\text{m}$ to $4.6 \times 10^{-2} \Omega\text{m}$. Furthermore, the low temperature resistance showed a clear peak around 15 K which corresponds well to the antiferromagnetic ordering temperatures determined in previous studies on single crystals [4,65–67].

The investigation of magnetic properties comprised of susceptibility, magnetic moment and magnetoresistance measurements. The susceptibility data was not compatible with measurements on bulk crystals [4] and no signs of antiferromagnetic order could be uncovered. However, magnetic hysteresis measurements at 5 K showed signatures of antiferromagnetic order, as found in Na_2IrO_3 single crystals, together with an exchange bias effect [98] due to AFM/FM interfaces inside the Na_2IrO_3 thin film. Most striking, however, was the observation of a weak antilocalization (WAL) effect [21] in magnetoresistance measurements below 4 K, since this effect is strongly associated with signatures for topological surface states and was in the past reported for thin films of the strong topological insulators Bi_2Te_3 and Bi_2Se_3 [28, 101, 105, 106]. Consequently, this finding supports the proposals [12, 17, 19] of a topological phase present in Na_2IrO_3 .

At last, Na_2IrO_3 thin films were investigated by optical measurements. By means of optical transmission and optical conductivity measurements, signatures of optical absorption below 6 eV were discovered. In an optical transmission measurement the onset of a small insulating Mott gap around 200 meV was observed in reasonable agreement with an experiment on single crystals [89]. Furthermore, two distinct absorption peaks, at 0.5 eV and 1.5 eV, manifest a splitting of the Ir $5d-t_{2g}$ manifold in agreement with proposed level schemes [60, 61] influenced by an interplay of spin-orbit coupling, electron correlations and trigonal distortions. The results presented here thus support the notion [89] of Na_2IrO_3 being a spin-orbit-assisted Mott insulating antiferromagnet.

Future work on Na_2IrO_3 thin films, must focus first on the reduction of surface roughness. Second, the effect of substrates and PLD parameters on topological signatures in magnetoresistance measurements, but also on optical conductivity and absorption should be studied. Furthermore, a highly sensitive AC Hall system is currently un-

der construction, which might enable a reliable measurement of Hall coefficient, Hall mobility and charge carrier density. Finally, surface sensitive probes, such as scanning tunneling microscopy (STM) or angle-resolved photoelectron spectroscopy, can be employed in order to enable a more direct observation of topological insulator properties, such as a surface state band structure. In the meantime, a possible STM study could be limited to individual large and in average smoother crystallites, that are present on the surface of Na_2IrO_3 thin films discussed here. Other avenues to explore are the annealing of thin films after deposition and the homoepitaxial growth on Na_2IrO_3 single crystals.

Bibliography

- [1] K. D. NELSON, Z. Q. MAO, Y. MAENO, Y. LIU: *Odd-parity superconductivity in Sr₂RuO₄*, Science (New York, N.Y.) **306**, 1151 (2004)
- [2] D. MANDRUS, J. THOMPSON, R. GAAL, L. FORRO, J. BRYAN, B. CHAKOUMAKOS, L. WOODS, B. SALES, R. FISHMAN, V. KEPPENS: *Continuous metal-insulator transition in the pyrochlore Cd₂Os₂O₇*, Physical Review B **63**, 1 (2001)
- [3] K. TAKADA, H. SAKURAI, E. TAKAYAMA-MUROMACHI, F. IZUMI, R. A. DILLANIAN, T. SASAKI: *Superconductivity in two-dimensional CoO₂ layers*, Nature **422**, 53 (2003)
- [4] Y. SINGH, P. GEGENWART: *Antiferromagnetic Mott insulating state in single crystals of the honeycomb lattice material Na₂IrO₃*, Physical Review B **82**, 1 (2010)
- [5] M. CRAWFORD, M. SUBRAMANIAN, R. HARLOW, J. FERNANDEZ-BACA, Z. WANG, D. JOHNSTON: *Structural and magnetic studies of Sr₂IrO₄*, Physical Review B **49**, 9198 (1994)
- [6] G. CAO, Y. XIN, C. ALEXANDER, J. CROW, P. SCHLOTTMANN, M. CRAWFORD, R. HARLOW, W. MARSHALL: *Anomalous magnetic and transport behavior in the magnetic insulator Sr₃Ir₂O₇*, Physical Review B **66**, 1 (2002)
- [7] A. ERICKSON, S. MISRA, G. MILLER, R. GUPTA, Z. SCHLESINGER, W. HARRISON, J. KIM, I. FISHER: *Ferromagnetism in the Mott Insulator Ba₂NaOsO₆*, Physical Review Letters **99**, 1 (2007)
- [8] B. KIM, H. JIN, S. MOON, J.-Y. KIM, B.-G. PARK, C. LEEM, J. YU, T. NOH, C. KIM, S.-J. OH, J.-H. PARK, V. DURAIRAJ, G. CAO, E. ROTENBERG: *Novel Jeff=1/2 Mott State Induced by Relativistic Spin-Orbit Coupling in Sr₂IrO₄*, Physical Review Letters **101**, 1 (2008)
- [9] G. CHEN, L. BALENTS: *Spin-orbit effects in Na₄Ir₃O₈: A hyper-kagome lattice antiferromagnet*, Physical Review B **78**, 1 (2008)

- [10] M. LAWLER, A. PARAMEKANTI, Y. KIM, L. BALENTS: *Gapless Spin Liquids on the Three-Dimensional Hyperkagome Lattice of $\text{Na}_4\text{Ir}_3\text{O}_8$* , Physical Review Letters **101**, 3 (2008)
- [11] D. PODOLSKY, A. PARAMEKANTI, Y. KIM, T. SENTHIL: *Mott Transition between a Spin-Liquid Insulator and a Metal in Three Dimensions*, Physical Review Letters **102**, 1 (2009)
- [12] A. SHITADE, H. KATSURA, J. KUNEŠ, X.-L. QI, S.-C. ZHANG, N. NAGAOSA: *Quantum Spin Hall Effect in a Transition Metal Oxide Na_2IrO_3* , Physical Review Letters **102**, 256403 (2009)
- [13] G. JACKELI, G. KHALIULLIN: *Mott Insulators in the Strong Spin-Orbit Coupling Limit: From Heisenberg to a Quantum Compass and Kitaev Models*, Physical Review Letters **102**, 2 (2009)
- [14] Y. OKAMOTO, M. NOHARA, H. ARUGA-KATORI, H. TAKAGI: *Spin-Liquid State in the $S=1/2$ Hyperkagome Antiferromagnet $\text{Na}_4\text{Ir}_3\text{O}_8$* , Physical Review Letters **99**, 4 (2007)
- [15] S. NAKATSUJI, Y. MACHIDA, Y. MAENO, T. TAYAMA, T. SAKAKIBARA, J. DUIJN, L. BALICAS, J. MILLICAN, R. MACALUSO, J. CHAN: *Metallic Spin-Liquid Behavior of the Geometrically Frustrated Kondo Lattice $\text{Pr}_2\text{Ir}_2\text{O}_7$* , Physical Review Letters **96**, 3 (2006)
- [16] Y. SINGH, S. MANNI, J. REUTHER, T. BERLIJN, R. THOMALE, W. KU, S. TREBST, P. GEGENWART: *Relevance of the Heisenberg-Kitaev Model for the Honeycomb Lattice Iridates $A_2\text{IrO}_3$* , Physical Review Letters **108**, 6 (2012)
- [17] J. WANG, R. LI, S.-C. ZHANG, X.-L. QI: *Topological Magnetic Insulators with Corundum Structure*, Physical Review Letters **106**, 2 (2011)
- [18] J. CHALOUPKA, G. JACKELI, G. KHALIULLIN: *Kitaev-Heisenberg Model on a Honeycomb Lattice: Possible Exotic Phases in Iridium Oxides $A_2\text{IrO}_3$* , Physical Review Letters **105**, 6 (2010)
- [19] H.-C. JIANG, Z.-C. GU, X.-L. QI, S. TREBST: *Possible proximity of the Mott*

- insulating iridate Na₂IrO₃ to a topological phase: Phase diagram of the Heisenberg-Kitaev model in a magnetic field*, Physical Review B **83**, 1 (2011)
- [20] C. L. KANE, E. J. MELE: *Quantum Spin Hall Effect in Graphene*, Physical Review Letters **95**, 1 (2005)
- [21] L. FU, C. KANE: *Topological insulators with inversion symmetry*, Physical Review B **76**, 1 (2007)
- [22] M. KÖNIG, S. WIEDMANN, C. BRÜNE, A. ROTH, H. BUHMANN, L. W. MOLENKAMP, X.-L. QI, S.-C. ZHANG: *Quantum spin hall insulator state in HgTe quantum wells.*, Science (New York, N.Y.) **318**, 766 (2007)
- [23] Y. XIA, D. QIAN, D. HSIEH, L. WRAY, A. PAL, H. LIN, A. BANSIL, D. GRAUER, Y. S. HOR, R. J. CAVA, M. Z. HASAN: *Observation of a large-gap topological-insulator class with a single Dirac cone on the surface*, Nature Physics **5**, 398 (2009)
- [24] Y. L. CHEN, J. G. ANALYTIS, J.-H. CHU, Z. K. LIU, S.-K. MO, X. L. QI, H. J. ZHANG, D. H. LU, X. DAI, Z. FANG, S. C. ZHANG, I. R. FISHER, Z. HUSSAIN, Z.-X. SHEN: *Experimental realization of a three-dimensional topological insulator, Bi₂Te₃.*, Science (New York, N.Y.) **325**, 178 (2009)
- [25] D. HSIEH, D. QIAN, L. WRAY, Y. XIA, Y. S. HOR, R. J. CAVA, M. Z. HASAN: *A topological Dirac insulator in a quantum spin Hall phase.*, Nature **452**, 970 (2008)
- [26] D. HSIEH, Y. XIA, L. WRAY, D. QIAN, A. PAL, J. H. DIL, J. OSTERWALDER, F. MEIER, G. BIHLMAYER, C. L. KANE, Y. S. HOR, R. J. CAVA, M. Z. HASAN: *Observation of unconventional quantum spin textures in topological insulators.*, Science (New York, N.Y.) **323**, 919 (2009)
- [27] C. KANE, J. MOORE: *Topological insulators*, Physics World S. 32–36 (2011)
- [28] J. CHEN, H. QIN, F. YANG, J. LIU, T. GUAN, F. QU, G. ZHANG, J. SHI, X. XIE, C. YANG, K. WU, Y. LI, L. LU: *Gate-Voltage Control of Chemical Potential and Weak Antilocalization in Bi₂Se₃*, Physical Review Letters **105**, 1 (2010)

- [29] H. LIN, T. DAS, L. A. WRAY, S.-Y. XU, M. Z. HASAN, A. BANSIL: *An isolated Dirac cone on the surface of ternary tetradymite-like topological insulators*, New Journal of Physics **13**, 095005 (2011)
- [30] Y. J. WANG, H. LIN, T. DAS, M. Z. HASAN, A. BANSIL: *Topological insulators in the quaternary chalcogenide compounds and ternary famatinite compounds*, New Journal of Physics **13**, 085017 (2011)
- [31] H. LIN, R. MARKIEWICZ, L. WRAY, L. FU, M. HASAN, A. BANSIL: *Single-Dirac-Cone Topological Surface States in the $TlBiSe_{2}$ Class of Topological Semiconductors*, Physical Review Letters **105**, 2 (2010)
- [32] B. YAN, C.-X. LIU, H.-J. ZHANG, C.-Y. YAM, X.-L. QI, T. FRAUENHEIM, S.-C. ZHANG: *Theoretical prediction of topological insulators in thallium-based III-V-VI 2 ternary chalcogenides*, EPL (Europhysics Letters) **90**, 37002 (2010)
- [33] Y. CHEN, Z. LIU, J. ANALYTIS, J.-H. CHU, H. ZHANG, B. YAN, S.-K. MO, R. MOORE, D. LU, I. FISHER, S. ZHANG, Z. HUSSAIN, Z.-X. SHEN: *Single Dirac Cone Topological Surface State and Unusual Thermoelectric Property of Compounds from a New Topological Insulator Family*, Physical Review Letters **105**, 2 (2010)
- [34] T. SATO, K. SEGAWA, H. GUO, K. SUGAWARA, S. SOUMA, T. TAKAHASHI, Y. ANDO: *Direct Evidence for the Dirac-Cone Topological Surface States in the Ternary Chalcogenide $TlBiSe_{2}$* , Physical Review Letters **105**, 1 (2010)
- [35] S. CHADOV, X. QI, J. KÜBLER, G. H. FECHER, C. FELSER, S. C. ZHANG: *Tunable multifunctional topological insulators in ternary Heusler compounds*, Nat Mater **9**, 541 (2010)
- [36] H. LIN, L. A. WRAY, Y. XIA, S. XU, S. JIA, R. J. CAVA, A. BANSIL, M. Z. HASAN: *Half-Heusler ternary compounds as new multifunctional experimental platforms for topological quantum phenomena*, Nat Mater **9**, 546 (2010)
- [37] D. XIAO, Y. YAO, W. FENG, J. WEN, W. ZHU, X.-Q. CHEN, G. STOCKS, Z. ZHANG: *Half-Heusler Compounds as a New Class of Three-Dimensional Topological Insulators*, Physical Review Letters **105**, 25 (2010)
- [38] M. KARGARIAN, J. WEN, G. FIETE: *Competing exotic topological insulator*

- phases in transition-metal oxides on the pyrochlore lattice with distortion*, Physical Review B **83**, 1 (2011)
- [39] H.-M. GUO, M. FRANZ: *Three-Dimensional Topological Insulators on the Pyrochlore Lattice*, Physical Review Letters **103**, 1 (2009)
- [40] B.-J. YANG, Y. KIM: *Topological insulators and metal-insulator transition in the pyrochlore iridates*, Physical Review B **82**, 1 (2010)
- [41] C. WEEKS, M. FRANZ: *Topological insulators on the Lieb and perovskite lattices*, Physical Review B **82**, 1 (2010)
- [42] H.-M. GUO, M. FRANZ: *Topological insulator on the kagome lattice*, Physical Review B **80**, 20 (2009)
- [43] G. P. COLLINS: *Computing with Quantum Knots*, Scientific American **294**, 56 (2006)
- [44] A. S. GOLDHABER, M. GOLDHABER: *The neutrino's elusive helicity reversal*, Physics Today **64**, 40 (2011)
- [45] L. FU, C. KANE: *Superconducting Proximity Effect and Majorana Fermions at the Surface of a Topological Insulator*, Physical Review Letters **100**, 1 (2008)
- [46] L. FU, C. KANE: *Josephson current and noise at a superconductor/quantum-spin-Hall-insulator/superconductor junction*, Physical Review B **79**, 1 (2009)
- [47] J. E. MOORE: *The birth of topological insulators.*, Nature **464**, 194 (2010)
- [48] J. L. ZHANG, S. J. ZHANG, H. M. WENG, W. ZHANG, L. X. YANG, Q. Q. LIU, S. M. FENG, X. C. WANG, R. C. YU: *Pressure-induced superconductivity in topological parent compound Bi_2Te_3* **108**, 24 (2011)
- [49] R. LUTCHYN, J. SAU, S. DAS SARMA: *Majorana Fermions and a Topological Phase Transition in Semiconductor-Superconductor Heterostructures*, Physical Review Letters **105**, 1 (2010)
- [50] Y. OREG, G. REFAEL, F. VON OPPEN: *Helical Liquids and Majorana Bound States in Quantum Wires*, Physical Review Letters **105**, 1 (2010)

- [51] V. MOURIK, K. ZUO, S. M. FROLOV, S. R. PLISSARD, E. P. A. M. BAKKERS, L. P. KOUWENHOVEN: *Signatures of Majorana fermions in hybrid superconductor-semiconductor nanowire devices.*, Science (New York, N.Y.) **336**, 1003 (2012)
- [52] A. KITAEV: *Anyons in an exactly solved model and beyond*, Annals of Physics **321**, 2 (2006)
- [53] A. KITAEV: *Fault-tolerant quantum computation by anyons*, Annals of Physics **303**, 2 (2003)
- [54] L. BALENTS: *Spin liquids in frustrated magnets.*, Nature **464**, 199 (2010)
- [55] S. MAEKAWA, T. TOHYAMA, S. BARNES, S. ISHIHARA, W. KOSHIBAE, G. KHALIULLIN: *Physics of Transition Metal Oxides* (Springer, Berlin ; Heidelberg ; New York ; Hong Kong ; London ; Milan ; Paris ; Tokyo, 2004)
- [56] F. GEBHARD: *The Mott Metal-Insulator Transition* (Springer, Berlin ; Heidelberg ; Singapore ; Tokyo ; New York ; Barcelona ; Budapest ; Hong Kong ; London ; Milan ; Paris ; Santa Clara, 1997)
- [57] M. IMADA, A. FUJIMORI, Y. TOKURA: *Metal-insulator transitions*, Reviews of Modern Physics **70**, 1039 (1998)
- [58] S. MOON, M. KIM, K. KIM, Y. LEE, J.-Y. KIM, J.-H. PARK, B. KIM, S.-J. OH, S. NAKATSUJI, Y. MAENO, I. NAGAI, S. IKEDA, G. CAO, T. NOH: *Electronic structures of layered perovskite Sr_2MO_4 ($M=Ru, Rh, and Ir$)*, Physical Review B **74**, 5 (2006)
- [59] B. KIM, H. OHSUMI, T. KOMESU, S. SAKAI, T. MORITA: *Phase-Sensitive Observation of a Spin-Orbital Mott State in Sr_2IrO_4* , Science **323**, 1329 (2009)
- [60] S. BHATTACHARJEE, S.-S. LEE, Y. B. KIM: *Spin-orbital locking, emergent pseudo-spin and magnetic order in honeycomb lattice iridates*, New Journal of Physics **14**, 073015 (2012)
- [61] H. JIN, H. KIM, H. JEONG, C. H. KIM, J. YU: *Mott Insulating Ground State and its Proximity to Spin-Orbit Insulators in $Na_{2}IrO_{3}$* , arXiv S. 5 (2009)

-
- [62] J. HUBBARD: *Electron Correlations in Narrow Energy Bands*, Proceedings of the Royal Society A Mathematical Physical and Engineering Sciences **276**, 238 (1963)
- [63] J. HUBBARD: *Electron Correlations in Narrow Energy Bands. II. The Degenerate Band Case*, Proceedings of the Royal Society A Mathematical Physical and Engineering Sciences **277**, 237 (1964)
- [64] J. ZAAANEN, G. SAWATZKY: *Band gaps and electronic structure of transition-metal compounds*, Physical review letters **55** (1985)
- [65] X. LIU, T. BERLIJN, W.-G. YIN, W. KU, A. TSVELIK, Y.-J. KIM, H. GRE-TARSSON, Y. SINGH, P. GEGENWART, J. HILL: *Long-range magnetic ordering in Na_2IrO_3* , Physical Review B **83**, 1 (2011)
- [66] S. K. CHOI, R. COLDEA, A. N. KOLMOGOROV, T. LANCASTER, I. I. MAZIN, S. J. BLUNDELL, P. G. RADAELLI, Y. SINGH, P. GEGENWART, K. R. CHOI, S. W. CHEONG, P. J. BAKER, C. STOCK, J. TAYLOR: *Spin waves and revised crystal structure of honeycomb iridate Na_2IrO_3* S. 12 (2012)
- [67] F. YE, S. CHI, H. CAO, B. CHAKOUMAKOS, J. FERNANDEZ-BACA, R. CUSTELCEAN, T. QI, O. KORNETA, G. CAO: *Direct evidence of a zigzag spin-chain structure in the honeycomb lattice: A neutron and x-ray diffraction investigation of single-crystal Na_2IrO_3* , Physical Review B **85**, 1 (2012)
- [68] I. KIMCHI, Y.-Z. YOU: *Kitaev-Heisenberg- J_2 - J_3 model for the iridates A_2IrO_3* , Physical Review B **84**, 2 (2011)
- [69] J. REUTHER, D. A. ABANIN, R. THOMALE: *Magnetic order and paramagnetic phases in the quantum J_1 - J_2 - J_3 honeycomb model*, Physical Review B **84**, 1 (2011)
- [70] S. BHATTACHARJEE, S.-S. LEE, Y. B. KIM: *Spin-Orbital Locking, Emergent Pseudo-Spin, and Magnetic order in Na_2IrO_3* , Physics **1**, 11 (2011)
- [71] B. SHKLOVSKII, A. EFROS: *Electronic properties of doped semiconductors* (Springer, Berlin ; Heidelberg ; New York ; Tokyo, 1984)

- [72] H. VON WENCKSTERN: *Electrical Properties of ZnO Thin Films and ZnO Single Crystals*, Diplomarbeit, Universität Leipzig (2002)
- [73] N. ASHCROFT, N. D. MERMIN: *Festkörperphysik* (Oldenburg Verlag, München; Wien; Oldenbourg, 2007), 3. Ed.
- [74] BONC-BRUEVIC: *Halbleiterphysik* (VEB Deutscher Verlag der Wissenschaften, Berlin, 1982)
- [75] E. A. DAVIS, N. F. MOTT: *Conduction in non-crystalline systems V. Conductivity, optical absorption and photoconductivity in amorphous semiconductors*, Philosophical Magazine **22**, 0903 (1970)
- [76] N. F. MOTT: *Conduction in non-crystalline materials*, Philosophical Magazine **19**, 835 (1969)
- [77] G. CAO, J. BOLIVAR, S. MCCALL, J. E. CROW: *Weak ferromagnetism, metal-to-nonmetal transition, and negative differential resistivity*, Physical Review B **57**, 39 (1998)
- [78] K. NOMURA, T. KAMIYA, H. OHTA, K. UEDA, M. HIRANO, H. HOSONO: *Carrier transport in transparent oxide semiconductor with intrinsic structural randomness probed using single-crystalline $\text{InGaO}_{3/5}(\text{ZnO})_5$ films*, Applied Physics Letters **85**, 1993 (2004)
- [79] A. SUEMASU, K. NAKAHATA, K. RO, T. KAMIYA, C. M. FORTMANN, I. SHIMIZU: *In situ hydrogen plasma treatment for improved transport of (400) oriented polycrystalline silicon films*, Solar Energy Materials Solar Cells **66**, 313 (2001)
- [80] M. SARACHIK, P. DAI: *Variable-Range Hopping in $\text{Si} : \text{B}$: A Temperature-Independent Prefactor in Three Dimensions*, Physica Status Solidi (B) **230**, 205 (2002)
- [81] D. C. LOOK: *Hopping Conduction in Molecular Beam Epitaxial GaAs Grown at Very Low Temperatures*, Journal of The Electrochemical Society **141**, 747 (1994)
- [82] D. LOOK, D. WALTERS, M. MANASREH: *Anomalous Hall-effect results in low-*

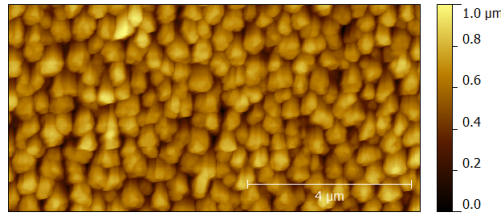
- temperature molecular-beam-epitaxial GaAs: Hopping in a dense EL2-like band*, Physical Review B **42**, 2 (1990)
- [83] H. A. ALBUQUERQUE: *Reduction of variable range hopping conduction in low-temperature molecular-beam epitaxial GaAs*, Journal of Applied Physics **95**, 3553 (2004)
- [84] N. F. MOTT: *Conduction in non-Crystalline systems*, Philosophical Magazine **22**, 7 (1970)
- [85] P. NAGELS: *Electronic transport in amorphous semiconductors*, Amorphous semiconductors (1985)
- [86] A. MILLER, E. ABRAHAMS: *Impurity Conduction at Low Concentrations*, Physical Review **120**, 745 (1960)
- [87] V. AMBEGAOKAR: *Hopping Conductivity in Disordered Systems*, Physical Review B **4**, 2612 (1971)
- [88] C. MCDANIEL: *Phase relations in the systems Na₂O—IrO₂ and Na₂O—PtO₂ in air*, Journal of Solid State Chemistry **146**, 139 (1974)
- [89] R. COMIN, G. LEVY, B. LUDBROOK, Z. H. ZHU, C. N. VEENSTRA, J. A. ROSEN, Y. SINGH, P. GEGENWART, D. STRICKER, J. N. HANCOCK, D. VAN DER MAREL, I. S. ELFIMOV, A. DAMASCELLI: *Na₂IrO₃ as a spin-orbit-assisted antiferromagnetic insulator with a 350 meV gap*, arXiv **1**, 1 (2012)
- [90] L. SPIESS: *Moderne Röntgenbeugung : Röntgendiffraktometrie für Materialwissenschaftler, Physiker und Chemiker* (Teubner, Wiesbaden, 2005)
- [91] C. P. DIETRICH: *Strukturelle und optische Eigenschaften von MgZnO-Dünnschichten*, Diplomarbeit, Universität Leipzig (2009)
- [92] C. SCHMIDT: *Strukturelle, optische und elektrische Untersuchung von Scandium-dotierten Zinkoxid-Dünnschichten*, Diplomarbeit, Universität Leipzig (2012)
- [93] L. J. VAN DER PAUW: *A Method of Measuring the Resistivity and Hall Coefficient on Lamellae and Arbitrary Shape*, Philips Technical Review. **20**, 220 (1958)

- [94] M. LORENZ: *Gepulste Laser-Plasmaabscheidung (PLD) von oxidischen Dünnsfilm- und Nanostrukturen*, Habilitationsschrift, University of Leipzig (2008)
- [95] C. KIM, H. KIM, H. JEONG, H. JIN, J. YU: *Topological Quantum Phase Transition in 5d Transition Metal Oxide $\text{Na}_{-2}\text{IrO}_{-3}$* , Physical Review Letters **108**, 1 (2012)
- [96] I. I. MAZIN, H. O. JESCHKE, D. I. KHOMSKII: *Formation of quasi-molecular orbitals and suppression of spin-orbit coupling in Na_2IrO_3* S. 1–7 (2012)
- [97] M. KHALID, A. SETZER, M. ZIESE, P. ESQUINAZI, A. PÖPPL, E. GOERING: *Ubiquity of ferromagnetic signals in common diamagnetic oxide crystals*, Physical Review B **81**, 214414 (2010)
- [98] J. BARZOLA-QUIQUIA, A. LESSIG, A. BALLESTAR, C. ZANDALAZINI, G. BRIDOUX, F. BERN, P. ESQUINAZI: *Revealing the origin of the vertical hysteresis loop shifts in an exchange biased Co/YMnO_3 bilayer.*, Journal of physics. Condensed matter : an Institute of Physics journal **24**, 366006 (2012)
- [99] J. ZIMAN: *Electrons and Phonons: The Theory of Transport Phenomena in Solids (Repr.)* (Clarendon Press, Oxford, 2007)
- [100] H. PENG, K. LAI, D. KONG, S. MEISTER, Y. CHEN, X.-L. QI, S.-C. ZHANG, Z.-X. SHEN, Y. CUI: *Aharonov-Bohm interference in topological insulator nanoribbons.*, Nature materials **9**, 225 (2010)
- [101] H.-T. HE, G. WANG, T. ZHANG, I.-K. SOU, G. WONG, J.-N. WANG, H.-Z. LU, S.-Q. SHEN, F.-C. ZHANG: *Impurity Effect on Weak Antilocalization in the Topological Insulator Bi_2Te_3* , Physical Review Letters **106**, 1 (2011)
- [102] H. KURIYAMA, J. MATSUNO, S. NIITAKA, M. UCHIDA, D. HASHIZUME, A. NAKAO, K. SUGIMOTO, H. OHSUMI, M. TAKATA, H. TAKAGI: *Epitaxially stabilized iridium spinel oxide without cations in the tetrahedral site*, Applied Physics Letters **96**, 182103 (2010)
- [103] S. J. MOON, H. JIN, K. W. KIM, W. S. CHOI, Y. S. LEE, J. YU, G. CAO, A. SUMI, H. FUNAKUBO, C. BERNHARD, T. W. NOH: *Dimensionality-Controlled Insulator-Metal Transition and Correlated Metallic State in 5d Tran-*

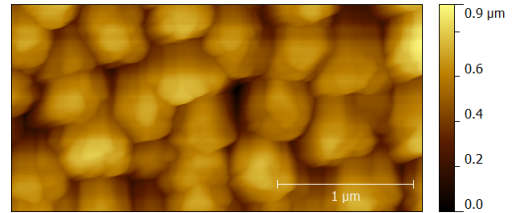
-
- sition Metal Oxides Sr n \tilde{A} $\frac{3}{4}$ 1 Ir n O 3n \tilde{A} $\frac{3}{4}$ 1 (n \hat{A} $\frac{1}{4}$ 1 , 2 , and 1)* **226402**, 2 (2008)
- [104] H. KURIYAMA, J. MATSUNO, S. NIITAKA, M. UCHIDA, D. HASHIZUME, A. NAKAO, K. SUGIMOTO, H. OHSUMI, M. TAKATA, H. TAKAGI: *Epitaxially stabilized iridium spinel oxide without cations in the tetrahedral site*, Applied Physics Letters **96**, 182103 (2010)
- [105] Y. S. KIM, M. BRAHLEK, N. BANSAL, E. EDREY, G. KAPILEVICH, K. IIDA, M. TANIMURA, Y. HORIBE, S.-W. CHEONG, S. OH: *Thickness-dependent bulk properties and weak antilocalization effect in topological insulator Bi $\{2\}$ Se $\{3\}$* , Physical Review B **84**, 1 (2011)
- [106] T. HIRAHARA, Y. SAKAMOTO, Y. TAKEICHI, H. MIYAZAKI, S.-I. KIMURA, I. MATSUDA, A. KAKIZAKI, S. HASEGAWA: *Anomalous transport in an n-type topological insulator ultrathin Bi $\{2\}$ Se $\{3\}$ film*, Physical Review B **82**, 1 (2010)

A Appendix

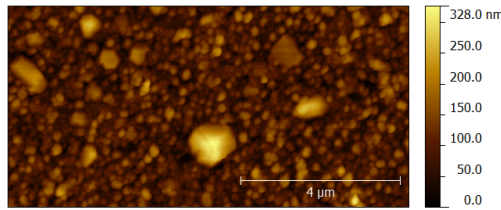
A.1 AFM Images



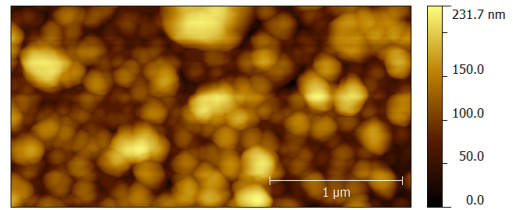
(a) E3298, $p = 0.1$ mbar, $10 \times 5 \mu\text{m}^2$, 143 nm



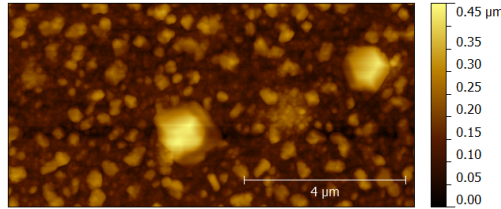
(b) E3298, $p = 0.1$ mbar, $3 \times 1.5 \mu\text{m}^2$, 121 nm



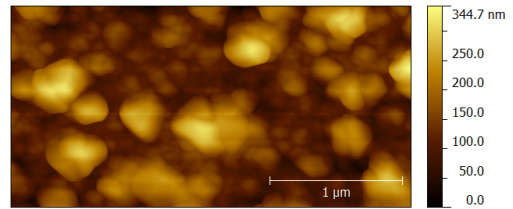
(c) E3300, $p = 0.016$ mbar, $10 \times 5 \mu\text{m}^2$, 44 nm



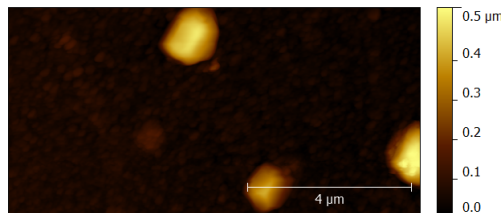
(d) E3300, $p = 0.016$ mbar, $3 \times 1.5 \mu\text{m}^2$, 41 nm



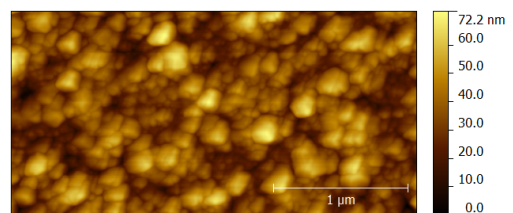
(e) E3303, $p = 0.002$ mbar, $10 \times 5 \mu\text{m}^2$, 65 nm



(f) E3303, $p = 0.002$ mbar, $3 \times 1.5 \mu\text{m}^2$, 56 nm

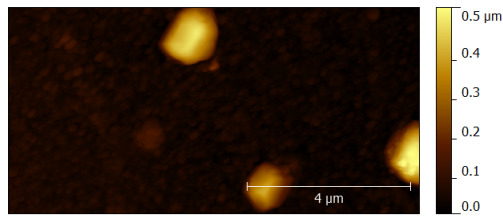


(g) E3304, $p = 3 \times 10^{-4}$ mbar, $10 \times 5 \mu\text{m}^2$, 77 nm

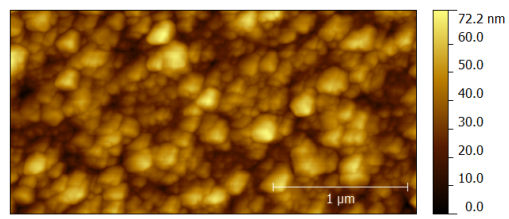


(h) E3304, $p = 3 \times 10^{-4}$ mbar, $3 \times 1.5 \mu\text{m}^2$, 11 nm

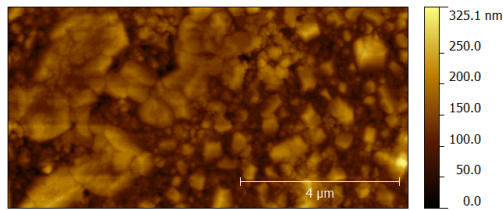
Figure A.1 AFM images for a series of Na_2IrO_3 films on a-sapphire grown at 400 W and oxygen partial pressures as indicated. RMS roughness in nm.



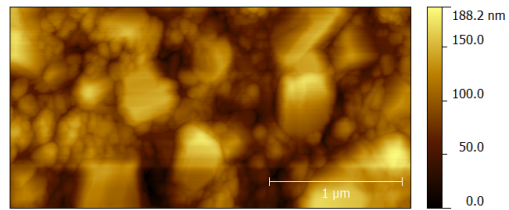
(a) E3304, 400 W, $10 \times 5 \mu\text{m}^2$, 77 nm



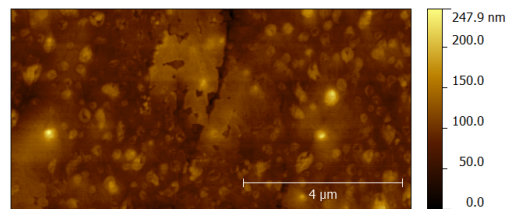
(b) E3304, 400 W, $3 \times 1.5 \mu\text{m}^2$, 11 nm



(c) E3316, 500 W, $10 \times 5 \mu\text{m}^2$, 39 nm

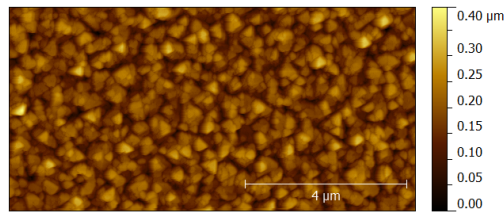
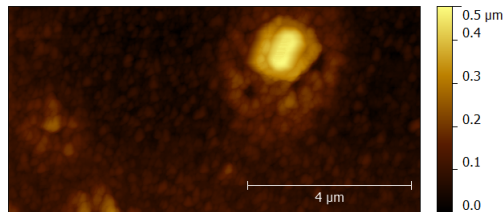
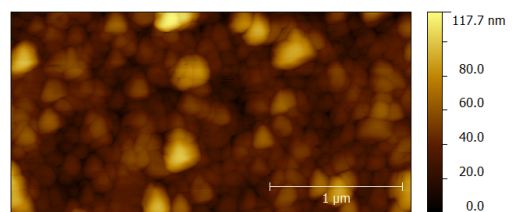
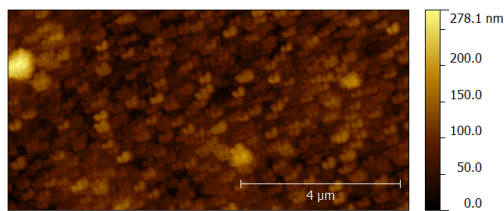
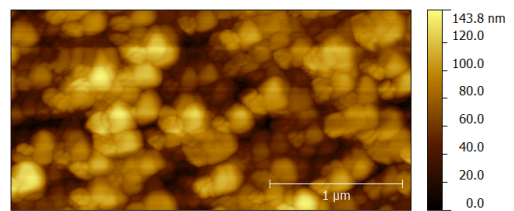
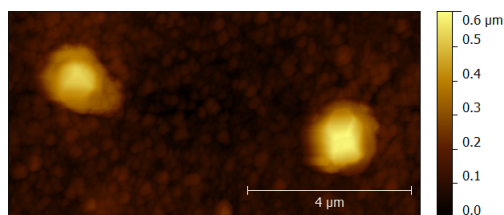
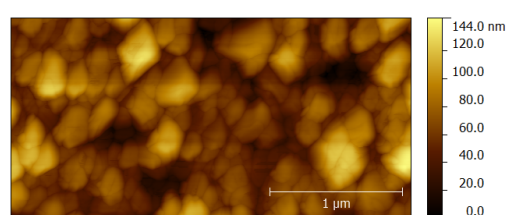


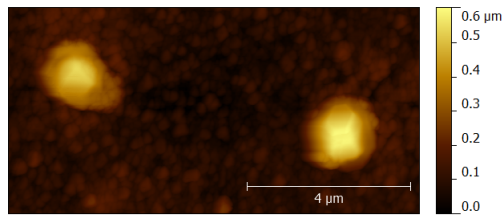
(d) E3316, 500 W, $3 \times 1.5 \mu\text{m}^2$, 33 nm



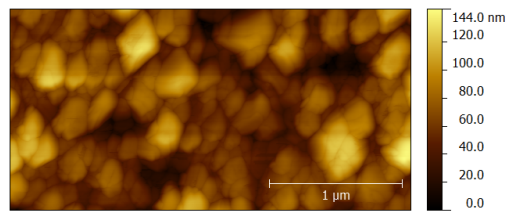
(e) E3318, 550 W, $10 \times 5 \mu\text{m}^2$, 19 nm

Figure A.2 AFM images for a series of Na_2IrO_3 films on a-sapphire grown at 3×10^{-4} mbar and heater powers as indicated. RMS roughness in nm.

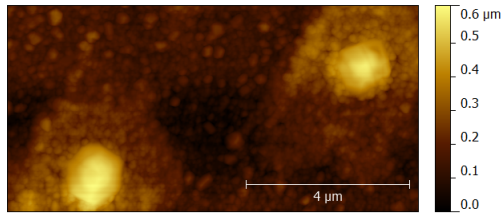
(a) E3337, $p = 0.1$ mbar, $10 \times 5 \mu\text{m}^2$, 47 nm(b) E3342, $p = 0.016$ mbar, $10 \times 5 \mu\text{m}^2$, 65 nm(c) E3342, $p = 0.016$ mbar, $3 \times 1.5 \mu\text{m}^2$, 16 nm(d) E3345, $p = 0.002$ mbar, $10 \times 5 \mu\text{m}^2$, 31 nm(e) E3345, $p = 0.002$ mbar, $3 \times 1.5 \mu\text{m}^2$, 16 nm(f) E3346, $p = 3 \times 10^{-4}$ mbar, $10 \times 5 \mu\text{m}^2$, 96 nm(g) E3346, $p = 3 \times 10^{-4}$ mbar, $3 \times 1.5 \mu\text{m}^2$, 23 nm**Figure A.3** AFM images for a series of Na_2IrO_3 films on YAO(001) grown at 400 W and oxygen partial pressures as indicated. RMS roughness in nm.



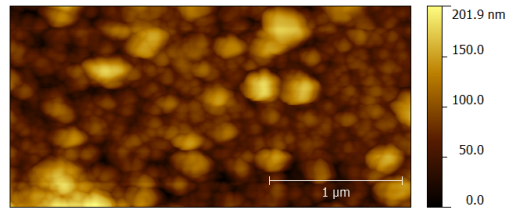
(a) E3346, 400 W, $10 \times 5 \mu\text{m}^2$, 96 nm



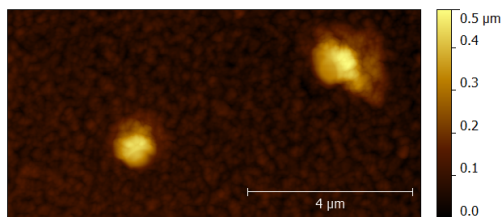
(b) E3346, 400 W, $10 \times 5 \mu\text{m}^2$, 22 nm



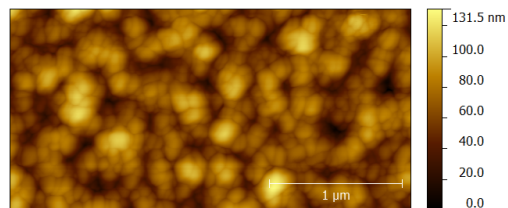
(c) E3354, 500 W, $10 \times 5 \mu\text{m}^2$, 105 nm



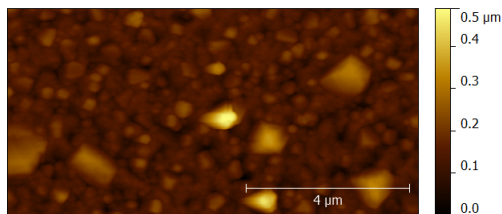
(d) E3354, 500 W, $3 \times 1.5 \mu\text{m}^2$, 31 nm



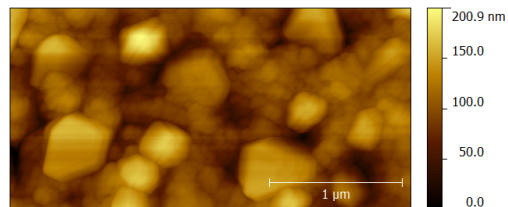
(e) E3355, 550 W, $10 \times 5 \mu\text{m}^2$, 59 nm



(f) E3355, 550 W, $3 \times 1.5 \mu\text{m}^2$, 18 nm



(g) E3362, 600 W, $10 \times 5 \mu\text{m}^2$, 48 nm



(h) E3362, 600 W, $3 \times 1.5 \mu\text{m}^2$, 29 nm

Figure A.4 AFM images for a series of Na_2IrO_3 films on YAO(001) grown at 3×10^{-4} mbar and heater powers as indicated. RMS roughness in nm.

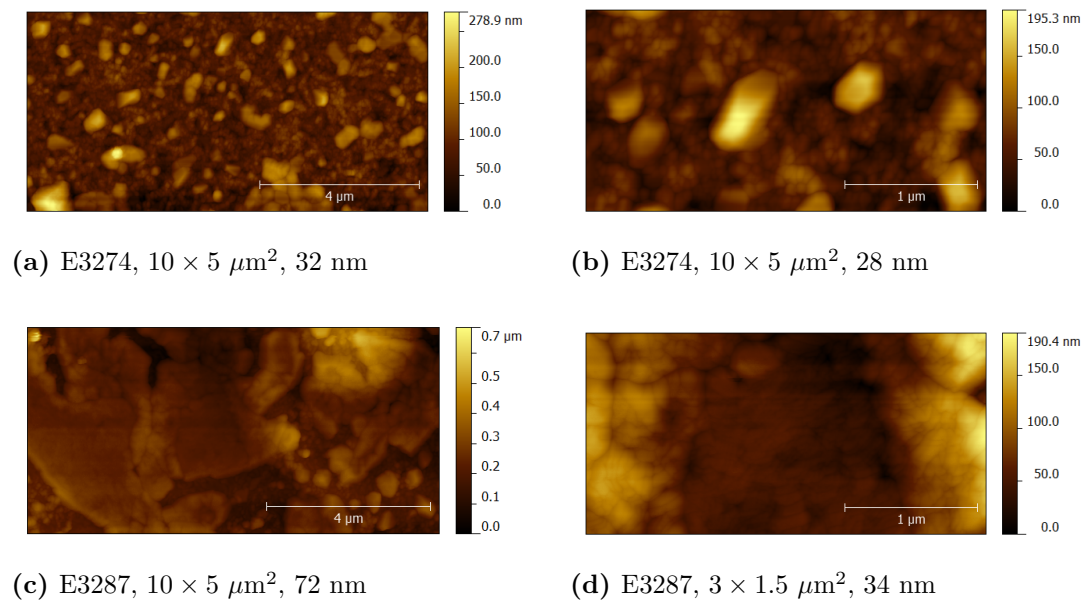


Figure A.5 AFM images of Na₂IrO₃ films on c-sapphire (top row) and c-ZnO (bottom row) grown at 400 W and 3×10^{-4} mbar. RMS roughness in nm.

A.2 JCPDS Diffraction Database Patterns

All patterns are taken from the *PCPDFWIN v. 2.00* software. Patterns for Na_2IrO_3 , $\text{Na}_4\text{Ir}_3\text{O}_8$, Al_2O_3 , YAlO_3 and ZnO are shown.

26-1376		Wavelength= 1.54056						i			
Na2IrO3		2 θ	Int	h	k	l	2 θ	Int	h	k	l
Sodium Iridium Oxide											
		16.682	100	2	0	0	82.094	3	5	3	3
		18.865	15	0	2	0	86.905	3	6	6	2
		19.668	10	1	1	1	94.496	1	9	3	1
		21.928	7	1	1	1	97.695	3	10	2	2
		25.303	4	2	2	0	101.881	4	1	3	5
		29.445	3	3	1	1	104.226	2	3	9	1
Rad.: Cu	λ : 1.54056	Filter: Ni	Beta	d-sp:							
Cut off:	Int.: Diffract.	I/Icor.:									
Ref: McDaniel, C., J. Solid State Chem., 9, 139 (1974)											
		33.510	55	1	3	1	110.940	2	10	0	2
		33.757	35	4	0	0	115.478	3	8	7	1
		34.938	65	1	3	1	116.919	3	1	9	3
		38.370	2	1	2	2	119.876	2	4	0	6
		38.748	3	0	2	2					
		40.208	85	2	0	2					
		43.804	15	3	3	1					
		51.626	6	6	0	0					
Sys.: Monoclinic	S.G.: A2/a (15)										
a: 10.765	b: 9.394	c: 5.418	A: 1.1459	C: 0.5768							
α :	β : 99.58	γ :	Z: [8]	mp:							
Ref: Ibid., J. Solid State Chem.											
		52.454	14	4	0	2					
		57.322	15	5	3	1					
		58.928	19	0	6	0					
		61.706	12	2	6	0					
		68.196	4	6	0	2					
		69.640	11	2	0	4					
		70.417	5	2	6	2					
		73.726	7	2	6	2					
		76.298	3	2	0	4					
Dx: 7.037	Dm:	SS/FOM: F ₃₀ = 5(.0191 , 345)									
Color: Black											
Compound disassociates at 1235 C. PSC: mC48. Mwt: 286.20.											
Volume[CD]: 540.26.											

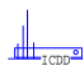
 1998 JCPDS-International Centre for Diffraction Data. All rights reserved
PCPDFWIN v. 2.00

Figure A.6 Na_2IrO_3

26-1377		Wavelength= 1.54056						i			
Na4Ir3O8		2 θ	Int	h	k	l	2 θ	Int	h	k	l
Sodium Iridium Oxide											
		13.935	40	1	1	0	59.981	2	5	3	0
		17.070	100	1	1	1	60.941	15	5	3	1
		22.094	35	2	1	0	61.935	1	6	0	0
		24.231	10	2	1	1	62.868	1	6	1	0
		29.796	3	3	0	0	63.832	1	6	1	1
		31.463	3	3	1	0	66.547	3	5	4	0
		33.064	70	3	1	1	67.471	4	5	4	1
		34.576	70	2	2	2	68.423	5	5	3	3
		36.025	6	3	2	0	69.288	16	6	2	0
		37.425	9	3	2	1	70.176	2	6	3	0
		40.133	65	4	0	0	72.868	6	4	4	4
		41.403	6	4	1	0	74.608	2	5	5	0
		42.674	5	3	3	0	75.442	5	7	1	1
		43.893	20	3	3	1	77.175	2	7	2	0
		46.283	9	4	2	1	78.075	2	7	2	1
		47.410	5	3	3	2	82.350	5	7	3	1
		50.764	2	5	0	0	84.015	1	6	5	0
		52.164	8	5	1	0	84.923	2	6	5	1
		52.911	20	5	1	1	86.615	3	8	0	0
		55.006	5	5	2	0	95.818	3	7	5	1
		57.993	30	4	4	0	96.683	5	6	6	2
		59.011	3	4	4	1	100.072	5	8	4	0
Mwt: 796.61. Volume[CD]: 725.36.											

2 θ	Int	h	k	l
102.744	3	9	1	1
114.280	4	8	4	4

 1998 JCPDS-International Centre for Diffraction Data. All rights reserved
PCPDFWIN v. 2.00

Figure A.7 $\text{Na}_4\text{Ir}_3\text{O}_8$

82-1399		Wavelength= 1.54060					C				
Al ₂ O ₃		2 θ	Int	h	k	l	2 θ	Int	h	k	l
Aluminum Oxide		25.591	689	0	1	2	86.550	28	1	2	8
		35.163	999*	1	0	4	89.029	66	0	2	10
		37.806	465	1	1	0					
		41.681	5	0	0	6					
		43.381	978	1	1	3					
		46.212	15	2	0	2					
		52.583	474	0	2	4					
		57.524	934	1	1	6					
		59.790	24	2	1	1					
		61.179	36	1	2	2					
		61.315	80	0	1	8					
		66.566	352	2	1	4					
		68.268	542	3	0	0					
		70.463	11	1	2	5					
		74.331	13	2	0	8					
		76.888	153	1	0	10					
		77.261	88	1	1	9					
		80.465	8	2	1	7					
		80.773	58	2	2	0					
		83.274	6	0	3	6					
		84.430	47	2	2	3					
		85.219	3	1	3	1					
		86.431	37	3	1	2					
Peak height intensity. R-factor: 0.070. PSC: hR10. Mwt: 101.96. Volume[CD]: 254.42.											



© 1998 JCPDS-International Centre for Diffraction Data. All rights reserved
PCPDFWIN v. 2.00

Figure A.8 Al₂O₃

79-2205		Wavelength= 1.54060					C				
ZnO		2 θ	Int	h	k	l	2 θ	Int	h	k	l
Zinc Oxide		31.766	564	1	0	0					
		34.419	415	0	0	2					
		36.251	999*	1	0	1					
		47.536	211	1	0	2					
		56.591	305	1	1	0					
		62.852	268	1	0	3					
		66.371	40	2	0	0					
		67.942	217	1	1	2					
		69.081	106	2	0	1					
		72.560	17	0	0	4					
		76.953	33	2	0	2					
		81.378	17	1	0	4					
		89.604	67	2	0	3					
Peak height intensity. R-factor: 0.012. PSC: hP4. Mwt: 81.38. Volume[CD]: 47.63.											



© 1998 JCPDS-International Centre for Diffraction Data. All rights reserved
PCPDFWIN v. 2.00

Figure A.9 ZnO

A Appendix

70-1677		Wavelength= 1.54060					C				
YAIO3		2 θ	Int	h	k	l	2 θ	Int	h	k	l
Yttrium Aluminum Oxide											
		20.940	8	0	1	1	54.200	11	1	3	2
		23.936	294	1	0	1	54.563	1	0	1	3
		24.115	192	0	2	0	54.563	1	3	0	1
		26.851	180	1	1	1	55.339	24	2	2	2
		33.601	213	2	0	0	55.605	51	1	4	1
		34.236	999*	1	2	1	55.932	37	1	0	3
		34.605	253	0	0	2	56.083	161	3	1	1
		35.797	99	2	1	0	57.428	23	1	1	3
		37.938	4	2	0	1	60.492	87	3	2	1
		38.619	10	1	0	2	61.065	85	2	4	0
		39.927	8	2	1	1	61.777	234	0	4	2
		40.580	64	1	1	2	61.777	234	1	2	3
		40.580	64	0	3	1	62.637	29	2	3	2
		41.786	195	2	2	0	63.440	2	3	0	2
		42.624	226	0	2	2	63.923	1	2	4	1
		44.141	70	1	3	1	64.223	4	2	0	3
		45.460	16	2	2	1	64.392	2	1	4	2
		46.049	11	1	2	2	64.829	2	3	1	2
		49.004	272	2	0	2	65.604	1	2	1	3
		49.390	186	0	4	0	65.776	3	0	5	1
		50.466	64	2	3	0	66.072	2	0	3	3
		50.641	114	2	1	2	67.453	66	3	3	1
		53.679	6	2	3	1	68.375	6	1	5	1
Rad.: CuK α 1 λ : 1.54060 Filter: d-sp: Calculated											
Cut off: 17.7 Int.: Calculated I/ICor.: 3.88											
Ref: Calculated from ICSD using POWD-12++, (1997)											
Ref: Diehl, R., Brandt, G., Mater. Res. Bull., 10, 85 (1975)											
Sys.: Orthorhombic S.G.: Pnma (62)											
a: 5.33(2)	b: 7.375(2)	c: 5.18(2)	A: 0.7227	C: 0.7024							
α :	β :	γ :	Z: 4	mp:							
Ref: Ibid.											
Dx: 5.346	Dm:	ICSD #: 004115									
Peak height intensity R-factor: 0.075. PSC: oP20. Mwt: 163.89. Volume[CD]: 203.62.											

2 θ	Int	h	k	l
68.665	3	1	3	3
68.909	1	3	2	2
69.660	1	2	2	3
70.632	12	4	0	0
71.952	39	4	1	0
72.127	123	2	4	2
73.001	28	0	0	4
73.295	14	2	5	0
73.295	14	4	0	1
74.598	1	4	1	1
75.477	7	3	3	2
75.477	7	1	0	4
75.923	3	4	2	0
75.923	3	2	5	1
76.202	2	2	3	3
76.358	5	1	5	2
76.775	7	1	1	4
76.938	6	3	0	3
77.612	11	0	6	0
77.814	25	1	4	3
78.218	36	0	2	4
78.218	36	3	1	3
78.455	19	4	2	1
80.601	1	1	2	4
81.100	6	4	0	2
82.026	26	3	2	3
82.363	42	4	1	2
82.615	80	1	6	1
82.804	40	2	0	4
83.653	22	2	5	2
84.062	16	2	1	4
84.373	8	3	4	2
84.777	1	4	3	1
85.080	2	2	4	3
86.132	1	4	2	2
86.892	6	1	3	4
87.280	8	2	6	0
87.844	19	2	2	4
87.844	19	0	6	2
88.031	37	3	5	1
88.302	49	3	3	3
89.157	9	1	5	3
89.816	1	2	6	1

 © 1998 JCPDS-International Centre for Diffraction Data. All rights reserved
PCPDFWIN v. 2.00

Figure A.10 YAIO₃

Acknowledgments

Bei der Erstellung der hier vorliegenden Arbeit habe ich im Laufe der vergangenen 12 Monate tatkräftige Unterstützung aus den Reihen der HLP-Gruppe erhalten. Zuallererst bin ich Herrn Prof Dr. Michael Lorenz für die sehr gute und intensive Betreuung zu großem Dank verpflichtet. Des Weiteren danke ich Herrn Prof. Dr. Marius Grundmann für die Aufnahme in die HLP-Gruppe. Ich bedanke mich außerdem bei Herrn Holger Hochmuth für seine Unterstützung bei der Probenzüchtung. Dabei dürfen gleichzeitig Frau Gabriele Ramm und Frau Monika Hahn nicht ausgelassen werden: Bei ihnen bedanke ich mich für die Erstellung der Targets bzw. für die Kontaktierung der Proben. Herrn Dr. José Barzola-Quiquia danke ich für weitere (magnetische) Messungen, Diskussionen und Ratschläge. Mein Dank geht auch an Frau Ulrike Teschner, Herrn Zhipeng Zhang und Herrn Dr. Heiko Frenzel für die Durchführung der optischen Messungen. Ich bedanke mich zudem bei Frau Kerstin Brachwitz und Herrn Michael Bonholzer für Hilfen am XRD und AFM sowie für den jederzeit freundlichen und fachlichen Austausch. Mein Dank gilt weiter Herrn Jörg Lenzner für die Einführung am SEM/EDX und für Messungen daran. Bedanken möchte ich mich natürlich auch bei der gesamten restlichen HLP-Gruppe für die angenehme und freundliche Atmosphäre und auch dafür, dass man mir bei Fragen oder Problemen immer mit Rat und Tat zur Seite stand. Meinen Eltern möchte ich an dieser Stelle auch besonders danken: für die tatkräftige Unterstützung während des Studiums, aber vor allem auch, dass sie mich bis an diesen Punkt begleitet haben.

Statement of Authorship (Selbständigkeitserklärung)

I hereby certify that this master thesis has been composed by myself, and describes my own work, unless otherwise acknowledged in the text. All references and verbatim extracts have been quoted, and all sources of information have been specifically acknowledged. It has not been accepted in any previous application for a degree.

Hiermit erkläre ich, dass ich die Masterarbeit selbständig verfasst habe und keine anderen als die angegebenen Quellen und Hilfsmittel benutzt habe. Alle Stellen der Arbeit, die wörtlich oder sinngemäß aus Veröffentlichungen oder aus anderweitigen fremden Äußerungen entnommen wurden, sind als solche kenntlich gemacht. Ferner erkläre ich, dass die Arbeit noch nicht in einem anderen Studiengang als Prüfungsleistung verwendet wurde.

Leipzig, November 19, 2012

Marcus Jenderka

Permission for Thesis Deposit (Erklärung für die Bibliothek)

After positive appraisal of this thesis, I agree that one copy of my presented thesis may remain at the disposal of the library of the University of Leipzig.

Ich bin einverstanden, dass die Arbeit nach positiver Begutachtung in der Universitätsbibliothek zur Verfügung steht.

Leipzig, November 19, 2012

Marcus Jenderka